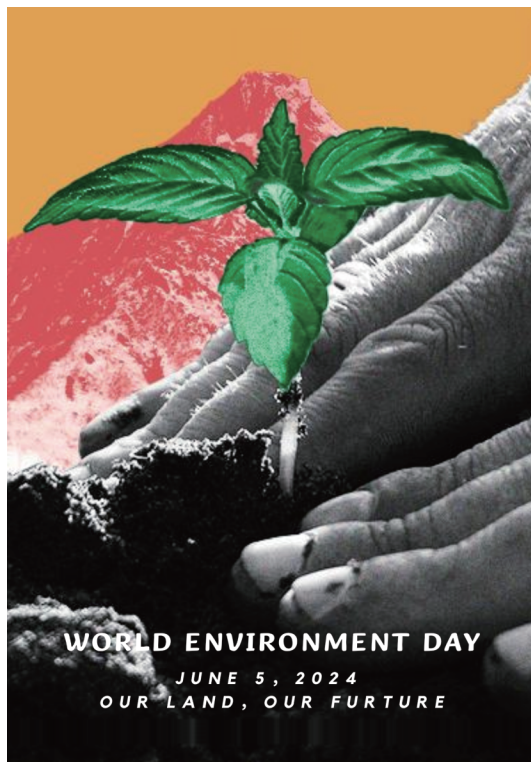


# CHINA CDC WEEKLY



## 中国疾病预防控制中心周报



### WORLD ENVIRONMENT DAY ISSUE

#### Preplanned Studies

- A Prospective Cohort Study of Antimony Exposure and Cognitive Impairment in Older Adults — China, 2017–2021 537
- Potential Adverse Outcome Pathways of Chlorinated Organophosphate Flame Retardants 542

#### Vital Surveillances

- Relationships Between Meteorological Factors and Mongolian Gerbils and Its Flea Burdens — Xilingol League, Inner Mongolia Autonomous Region, China, 2012–2021 547

#### Methods and Applications

- Establishment and Application of a Radiation Dose Rate Model for Nuclear Medicine Examinees 553

#### Outbreak Reports

- First Case Report of Cystic Echinococcosis Caused by G7 Genotype *Echinococcus intermedicus* Confirmed by Genetic Sequencing — Southern China, December 2023 558



ISSN 2096-7071



## Editorial Board

**Editor-in-Chief** Hongbing Shen

**Founding Editor** George F. Gao

**Deputy Editor-in-Chief** Liming Li    Gabriel M Leung    Zijian Feng

**Executive Editor** Chihong Zhao

### Members of the Editorial Board

Rui Chen	Wen Chen	Xi Chen (USA)	Zhuo Chen (USA)
Gangqiang Ding	Xiaoping Dong	Pei Gao	Mengjie Han
Yuantaao Hao	Na He	Yuping He	Guoqing Hu
Zhibin Hu	Yueqin Huang	Na Jia	Weihua Jia
Zhongwei Jia	Guangfu Jin	Xi Jin	Biao Kan
Haidong Kan	Ni Li	Qun Li	Ying Li
Zhenjun Li	Min Liu	Qiyong Liu	Xiangfeng Lu
Jun Lyu	Huilai Ma	Jiaqi Ma	Chen Mao
Xiaoping Miao	Ron Moolenaar (USA)	Daxin Ni	An Pan
Lance Rodewald (USA)	William W. Schluter (USA)	Yiming Shao	Xiaoming Shi
Yuelong Shu	RJ Simonds (USA)	Xuemei Su	Chengye Sun
Quanfu Sun	Xin Sun	Feng Tan	Jinling Tang
Huaqing Wang	Hui Wang	Linhong Wang	Tong Wang
Guizhen Wu	Jing Wu	Xifeng Wu (USA)	Yongning Wu
Min Xia	Ningshao Xia	Yankai Xia	Lin Xiao
Wenbo Xu	Hongyan Yao	Zundong Yin	Dianke Yu
Hongjie Yu	Shicheng Yu	Ben Zhang	Jun Zhang
Liubo Zhang	Wenhua Zhao	Yanlin Zhao	Xiaoying Zheng
Maigeng Zhou	Xiaonong Zhou	Guihua Zhuang	

## Advisory Board

**Director of the Advisory Board** Jiang Lu

**Vice-Director of the Advisory Board** Yu Wang    Jianjun Liu    Jun Yan

### Members of the Advisory Board

Chen Fu	Gauden Galea (Malta)	Dongfeng Gu	Qing Gu
Yan Guo	Ailan Li	Jiafa Liu	Peilong Liu
Yuanli Liu	Kai Lu	Roberta Ness (USA)	Guang Ning
Minghui Ren	Chen Wang	Hua Wang	Kean Wang
Xiaoqi Wang	Zijun Wang	Fan Wu	Xianping Wu
Jingjing Xi	Jianguo Xu	Gonghuan Yang	Tilahun Yilma (USA)
Guang Zeng	Xiaopeng Zeng	Yonghui Zhang	Bin Zou

## Editorial Office

**Directing Editor** Chihong Zhao

**Managing Editors** Yu Chen

**Senior Scientific Editors** Daxin Ni    Ning Wang    Wenwu Yin    Shicheng Yu    Jianzhong Zhang    Qian Zhu

### Scientific Editors

Weihong Chen	Tao Jiang	Xudong Li	Nankun Liu	Liwei Shi	Liuying Tang
Meng Wang	Zhihui Wang	Qi Yang	Qing Yue	Lijie Zhang	Ying Zhang

## Preplanned Studies

## A Prospective Cohort Study of Antimony Exposure and Cognitive Impairment in Older Adults — China, 2017–2021

Yidan Qiu<sup>1,2</sup>; Saisai Ji<sup>2</sup>; Chen Chen<sup>2</sup>; Jinhui Zhou<sup>2</sup>; Jun Wang<sup>2</sup>; Bing Wu<sup>2,3</sup>; Yuan Wei<sup>2,4</sup>; Fangyu Li<sup>2,5</sup>; Xulin Zheng<sup>2,3</sup>; Lanjing Xu<sup>1,2</sup>; Zheng Zhang<sup>2,3</sup>; Feng Zhao<sup>2</sup>; Guangdi Chen<sup>6</sup>; John S. Ji<sup>7,8</sup>; Yuebin Lyu<sup>2</sup>; Shilu Tong<sup>2,3,9,10</sup>; Xiaoming Shi<sup>2,3,#</sup>

### Summary

#### What is already known about this topic?

Antimony (Sb) has been identified as a new neurotoxicant that impacts neurological functions in animal studies. However, its effects on the human population remain unknown.

#### What is added by this report?

The study reveals that there is an association between exposure to Sb and a higher incidence of cognitive impairment in older adults. The dose-response curve demonstrates that the risk of cognitive impairment consistently increased with higher levels of Sb exposure without a discernible threshold.

#### What are the implications for public health practice?

Reducing exposure to Sb may have a beneficial effect in delaying or preventing the onset of cognitive impairment. This intervention has the potential to significantly decrease the disease burden associated with cognitive impairment, ultimately contributing to social development.

Antimony (Sb) has been identified as a novel neurotoxin that affects neurocognition in previous animal studies. However, there is limited research on the association between Sb exposure and cognitive impairment in humans. Given the increasing aging population, it is crucial to investigate the relationship between Sb and cognitive impairment in older adults. In this study, we utilized data from the Healthy Aging and Biomarkers Cohort Study (HABCS), a prospective cohort study. A total of 1,333 participants aged 65 years and older were recruited in 2017–2018 and followed up in 2020–2021. Blood Sb (B-Sb) and urine Sb (U-Sb) concentrations were measured using inductively coupled plasma mass spectrometry. Cognitive function was assessed using the validated Mini-Mental State Examination. During the follow-up period of 4,972.1 person-years, 241 cases of cognitive

impairments were recorded. Cox regression models, adjusted for potential covariates, showed that the risk of cognitive impairment increased by 56.5% for each e-fold increase in U-Sb. Similar results were observed for B-Sb, with a 52.3% increase in the risk of cognitive impairment for each e-fold increase. Our findings suggest that reducing Sb exposure may help mitigate the burden of cognitive impairment, particularly in regions with high Sb pollution.

The participants were selected from the HABCS study (1), which was conducted in nine regions known for longevity between 2017 and 2018. Follow-up of participants took place between 2020 and 2021. Detailed information about the nine longevity regions can be found in the Supplementary Material (available at <https://weekly.chinacdc.cn/>). A total of 3,016 participants were initially recruited, but after excluding those under 65 years old, individuals without blood or urine Sb information, those with missing data on cognitive function, and those who were lost to follow-up or died, a final sample size of 1,333 participants was included (Supplementary Figure S1 and Supplementary Material, available at <https://weekly.chinacdc.cn/>). Cognitive function was assessed using the Chinese version of the Mini-Mental State Examination (MMSE). Participants completed a face-to-face interview involving 24 items on the MMSE questionnaire, with a maximum score of 30. Cognitive impairment was defined as follows: uneducated individuals with an MMSE score of less than 18, individuals with 1–6 years of education and an MMSE score of less than 20, and individuals with 6 or more years of education and an MMSE score of less than 24 (2). Furthermore, standardized questionnaires were used to collect sociodemographic characteristics, frequency of food consumption, and health-related information. Information on exposure to Sb and other metals was obtained through biological sample collection. Please refer to the supplementary material for details on Sb detection and covariate definitions

(Supplementary Table S1 and Supplementary Material, available at <https://weekly.chinacdc.cn/>). Ethical approval for the study was obtained from the Ethics Review Committee of the National Institute of Environmental Health, Chinese Center for Disease Control and Prevention (No. 2017018).

The study participants were divided into two groups based on their cognitive function. Continuous variables with a normal distribution were presented as mean±standard deviation (SD), while those with a skewed distribution were described as median ( $P_{25}$ – $P_{75}$ ). The t-test or rank sum test was used to analyze continuous variables, while categorical variables were described as frequencies (percentages) and analyzed using the  $\chi^2$ -test. A correlation map was used to represent the relationship between the independent variable and the covariable. A strong correlation was defined as  $|r|>0.7$ , indicating the possibility of multicollinearity. However, no statistically significant correlations were observed between variables in the correlation map (Supplementary Figure S2, available at <https://weekly.chinacdc.cn/>). The associations between Sb exposure and the incidence of cognitive impairment were assessed using Cox proportional hazard models. The survival time for participants was calculated from the baseline survey to either the date of cognitive impairment or the end of the survey. Sb exposure levels were modeled as continuous variables using ln-transformed values or categorical variables stratified by high, medium, and low concentrations. Please refer to the Supplementary Material for specific methods used to divide concentration categories. To ensure the accuracy of the study, covariates were included in the Cox proportional hazard models. More details about the models can be found in the eMethods section in the Supplementary Material. The association between Sb exposure and cognitive function was flexibly modeled using restricted cubic splines (RCS). Subgroup analysis was conducted to explore the effects of the association in different populations, and sensitivity analysis was performed to assess the robustness of the observations. Additional information can be found in the supplementary materials. All statistical tests were two-tailed, and  $P$  values  $<0.05$  were considered statistically significant. Statistical analyses were performed using SAS software (version 9.4, SAS Institute Inc., Cary, USA).

A total of 1,333 participants were enrolled in the study from 2020 to 2021, with an average follow-up duration of  $3.73\pm 0.21$  years. Among these participants,

1,092 (81.9%) had normal cognitive function, while 241 (18.1%) had cognitive impairment. The median ( $P_{25}$ – $P_{75}$ ) levels of B-Sb and U-Sb exposure were 2.98 (2.45–3.72)  $\mu\text{g/L}$  and 0.05 (0.05–0.19)  $\mu\text{g/L}$ , respectively (Supplementary Table S2, available at <https://weekly.chinacdc.cn/>).

After controlling for all covariates, we observed that the risk of cognitive impairment increased by 56.5% with each e-fold increase in U-Sb [hazard ratio ( $HR$ )=1.565, 95% confidence interval ( $CI$ ): 1.230, 1.991]. Compared to the low U-Sb group, the  $HR$  (95%  $CI$ ) for cognitive impairment in the high U-Sb group was 2.456 (1.536, 3.927) (Table 1, Model 4). The non-linear relationship between U-Sb and the risk of cognitive impairment in older adults was confirmed by restricted cubic spline analysis ( $P_{\text{nonlinear}}<0.05$ ) (Figure 1A). Furthermore, the risk of cognitive impairment in older adults increased linearly with B-Sb exposure, with a 52.3% increased risk for each e-fold increase in B-Sb ( $HR$ =1.523, 95%  $CI$ : 1.100, 2.109) (Figure 1B, Table 1).

In the subgroup analysis, we observed a stronger impact of Sb exposure on cognitive impairment in individuals aged 65–79 years, men, and individuals who consume alcohol. Among smokers, the effect of U-Sb on cognitive impairment was higher compared to non-smokers. We found a significant interaction effect between B-Sb and sex, but no significant interactions were observed between age, cigarette smoking, alcohol drinking, and Sb exposure (Table 2). The results of four sensitivity analyses further supported the robustness of our findings (Supplementary Tables S3–S6, available at <https://weekly.chinacdc.cn/>).

## DISCUSSION

To the best of our knowledge, this study represents the first attempt to examine the impact of Sb exposure on cognitive impairment in older adults in China. Using data from the HABCS, a 3-year prospective cohort study, we identified a significant association between Sb exposure and an elevated risk of cognitive impairment.

Previous epidemiological studies have not extensively examined the association between Sb exposure and cognition in older adults. One cross-sectional study ( $n=631$ ) conducted using National Health and Nutrition Examination Survey (NHANES) data found a non-linear relationship between U-Sb and cognitive function in older adults. Lower doses of U-Sb were associated with better cognitive function, while higher

TABLE 1. Association of antimony with cognitive impairment among Chinese older adults from 2017 to 2021.

Antimony	HR (95% CI)				
	Crude model	Model 1	Model 2	Model 3	Model 4
Ln-transformed B-Sb <sup>§</sup>	1.189 (0.906, 1.559)	1.179 (0.866, 1.605)	1.121 (0.830, 1.515)	1.235 (0.865, 1.765)	1.523 (1.100, 2.109)*
Categorical by concentration					
Low group	1.000 reference				
Medium group	1.086 (0.789, 1.496)	1.045 (0.752, 1.451)	1.031 (0.735, 1.447)	1.128 (0.788, 1.613)	1.183 (0.822, 1.704)
High group	1.229 (0.891, 1.694)	1.239 (0.890, 1.726)	1.140 (0.810, 1.604)	1.213 (0.844, 1.745)	1.300 (0.890, 1.899)
<i>P</i> for trend	0.209	0.204	0.452	0.296	0.174
Ln-transformed U-Sb <sup>¶</sup>	1.323 (1.127, 1.553) <sup>†</sup>	1.312 (1.100, 1.565) <sup>†</sup>	1.309 (1.084, 1.580) <sup>†</sup>	1.353 (1.105, 1.658) <sup>†</sup>	1.565 (1.230, 1.991) <sup>†</sup>
Categorical by concentration					
Low group	1.000 reference				
Medium group	1.476 (1.060, 2.056)*	1.392 (0.970, 1.996)	1.363 (0.932, 1.993)	1.495 (0.989, 2.259)	1.403 (0.913, 2.156)
High group	1.683 (1.216, 2.330) <sup>†</sup>	1.774 (1.238, 2.542) <sup>†</sup>	1.708 (1.173, 2.488) <sup>†</sup>	1.874 (1.243, 2.825) <sup>†</sup>	2.456 (1.536, 3.927) <sup>†</sup>
<i>P</i> for trend	<0.001	0.002	0.005	0.002	<0.001

Abbreviation: B-Sb=blood antimony; U-Sb=urine antimony; HR=hazard ratio; CI=confidence interval.

\* Denotes statistical significance at  $P<0.05$ .

<sup>†</sup> Denotes statistical significance at  $P<0.01$ .

<sup>§</sup> low group ( $0.04\leq\text{B-Sb}\leq 2.45\ \mu\text{g/L}$ ), medium group ( $2.45<\text{B-Sb}\leq 2.98\ \mu\text{g/L}$ ), high group ( $2.98<\text{B-Sb}\leq 3.72\ \mu\text{g/L}$ ); Model 1 was adjusted for age, sex, ethnicity, marriage status, and residence; Model 2 was further adjusted for cigarette smoking, alcohol drinking, the consumption of fruit, fish, milk, and nuts; Model 3 was further adjusted for BMI, CVD, hypertension, diabetes and CKD; Model 4 was further adjusted for blood As, blood Cd, blood Se, blood Hg, blood Pb and blood Mn.

<sup>¶</sup> low group ( $\text{U-Sb}\leq 0.05\ \mu\text{g/L}$ ), medium group ( $0.05<\text{U-Sb}\leq 0.19\ \mu\text{g/L}$ ), high group ( $0.19<\text{U-Sb}\leq 2.17\ \mu\text{g/L}$ ); Model 1 was adjusted for urine creatinine, age, sex, ethnicity, marriage status, and residence; Model 2 was further adjusted for cigarette smoking, alcohol drinking, and the consumption of fruit, fish, milk, and nuts; Model 3 was further adjusted for BMI, CVD, hypertension, diabetes and CKD; Model 4 was further adjusted for urine As, urine Cd, urine Se, urine Hg, urine Pb and urine Mn.

doses may be linked to cognitive impairment (3). In contrast, our study is a larger cohort study that considers other cognition-related metals as covariates, in line with previous literature. A 5-year cohort study in Portuguese older adults found no association between Sb levels in fingernails and cognitive decline (4). However, the inconsistent findings may be due to the small sample size and different exposure assessment methods. Another case-control study reported higher B-Sb levels in the healthy group compared to the dementia group, suggesting a potential protective effect of Sb on cognitive function (5). Differences in study design and adjustments for covariates may explain the inconsistencies between studies. Animal studies support our findings. Tanu et al. demonstrated the toxic effect of Sb on memory changes in mice (6). Xu et al. assessed the risk of Sb-associated dementia (AD) and found that Sb contributed to amyloid-beta accumulation and hyperphosphorylation of tau protein in the mouse brain, indicating an association between Sb exposure and AD risk (7). Although the exact cellular and molecular mechanisms of Sb-related neurotoxicity remain unclear, there is evidence suggesting that Sb can damage cognitive function. For instance, Sb inhibits protein kinase B (Akt), which

leads to abnormal activation of the Wnt/ $\beta$ -catenin pathway, causing neuronal apoptosis and neurotoxicity (8). Additionally, Sb induces autophagic cell death by suppressing the Akt/mammalian target of the rapamycin (mTOR) pathway through reactive oxygen species, resulting in cognitive impairment (9).

Subgroup analysis revealed a stronger association between Sb exposure and cognitive impairment in men compared to women. This difference in association may be attributed to variations in lifestyle factors, such as higher rates of smoking and alcohol consumption among men, which increase their likelihood of Sb exposure.

There are several limitations in this study. First, the findings of our study may not be generalized to the general population as our research participants consisted exclusively of older adults. Second, the follow-up period of this study was limited to three years, which necessitates further investigation through long-term observational studies to establish a causal relationship between Sb and cognitive impairment. Third, there may be incomplete or inaccurate data regarding the collected covariates. For instance, information on smoking, drinking, diabetes, and cardiovascular disease relied on self-reporting, which

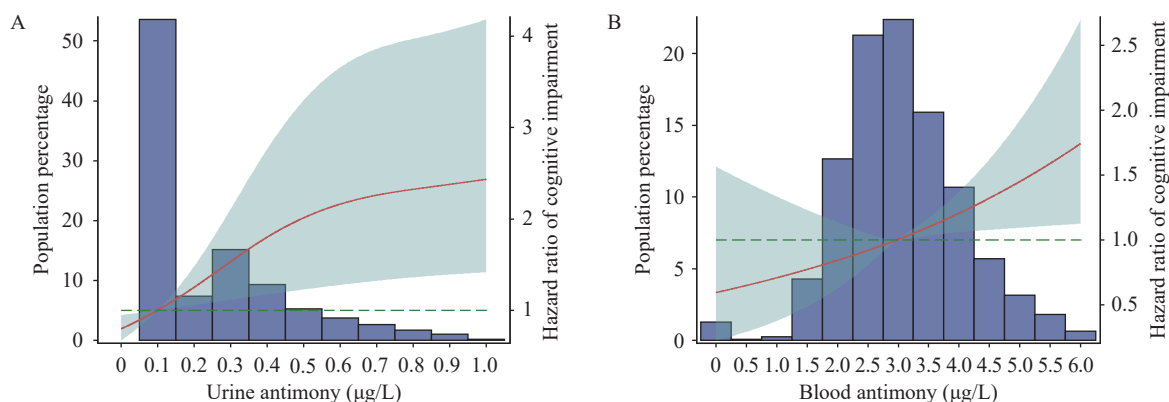


FIGURE 1. Association of antimony with cognitive impairment among Chinese older adults from 2017 to 2021 in Cox models with restricted cubic spline. (A) the dose-response relationship between urine antimony levels and cognitive impairment; (B) the dose-response relationship between blood antimony levels and cognitive impairment.

Note: In Figure 1A, the plot contains three knots located at the 50th, 75th, and 95th centiles; the red line represents the estimated effect of urine antimony on the risk of cognitive impairment, while the green areas indicate the corresponding 95% confidence interval; the effect estimates were adjusted for several covariates, including urine creatinine, age, sex, ethnicity, marital status, residence, cigarette smoking, alcohol drinking, dietary intake of fruit, fish, milk, and nuts, BMI, CVD, hypertension, diabetes, CKD, urine As, urine Cd, urine Se, urine Hg, urine Pb, and urine Mn. In Figure 1B, three knots were observed at the 25th, 50th, and 75th centiles; the estimated effect of blood antimony on the risk of cognitive impairment in older adults is represented by the red line, while the green areas indicate the 95% confidence interval; Adjusted covariates include age, sex, ethnicity, marital status, place of residence, cigarette smoking, alcohol drinking, fruit, fish, milk, and nuts, BMI, CVD, hypertension, diabetes, CKD, blood As, blood Cd, blood Se, blood Hg, blood Pb, and blood Mn.

TABLE 2. Association of antimony with cognitive impairment among Chinese older adults in selected population subgroups from 2017 to 2021.

Subgroup	Ln-transformed B-Sb (HR, 95% CI) <sup>§</sup>	<i>P</i> <sub>interaction</sub>	Ln-transformed U-Sb (HR, 95% CI)	<i>P</i> <sub>interaction</sub>
Age, years		0.433		0.072
65–79 (n=759)	2.577 (1.235, 5.377)*		1.859 (1.106, 3.125)*	
≥80 (n=574)	1.242 (0.829, 1.861)		1.557 (1.174, 2.064) <sup>†</sup>	
Sex		0.048		0.666
Men (n=703)	2.458 (1.416, 4.267) <sup>†</sup>		1.733 (1.243, 2.416) <sup>†</sup>	
Women (n=630)	1.041 (0.681, 1.592)		1.293 (0.899, 1.860)	
Cigarette smoking		0.375		0.175
Smoker (n=423)	2.015 (0.974, 4.169)		2.099 (1.345, 3.278) <sup>†</sup>	
Non-smoker (n=904)	1.445 (0.972, 2.147)		1.536 (1.116, 2.116) <sup>†</sup>	
Alcohol drinking		0.123		0.653
Drinker (n=390)	2.705 (1.075, 6.807)*		1.891 (1.145, 3.123)*	
Non-drinker (n=934)	1.346 (0.964, 1.881)		1.431 (1.046, 1.957)*	

Abbreviation: B-Sb=blood antimony; U-Sb=urine antimony; HR=hazard ratio; CI=confidence interval.

\* Denotes statistical significance at  $P < 0.05$ .

<sup>†</sup> Denotes statistical significance at  $P < 0.01$ .

<sup>§</sup> Model was adjusted for age, sex, ethnicity, marriage status, residence, cigarette smoking, alcohol drinking, the consumption of fruit, fish, milk, and nuts, BMI, CVD, hypertension, diabetes, CKD, blood As, blood Cd, blood Se, blood Hg, blood Pb, and blood Mn.

<sup>¶</sup> Model was adjusted for urine creatinine, age, sex, ethnicity, marriage status, residence, cigarette smoking, alcohol drinking, the consumption of fruit, fish, milk, and nuts, BMI, CVD, hypertension, diabetes, CKD, urine As, urine Cd, urine Se, urine Hg, urine Pb, and urine Mn.

may be subject to recall bias. Additionally, although oxidative stress and psychological stress could potentially act as confounding factors, our study did not measure these indicators. Lastly, the loss of follow-

up bias is an unavoidable limitation in this study.

In conclusion, our study findings from a prospective cohort of older adults in China reveal a significant association between Sb exposure and an increased risk

of cognitive impairment, particularly in men. This suggests that Sb may act as a novel neurotoxicant, adversely affecting the neurocognitive function of older individuals. Food, particularly seafood and dairy products, is considered the primary source of Sb intake among the population (10). Therefore, reducing Sb exposure could potentially delay or prevent the onset of cognitive impairment in older adults. Future research should include longer follow-up studies to provide a more comprehensive understanding of the relationship between Sb exposure and cognition, allowing for a better exploration of causality.

**Conflicts of interest:** Xiaoming Shi is a editorial board member of the journal China CDC Weekly. He was not involved in the peer-review or handling of the manuscript. The authors have no other competing interests to disclose.

**Funding:** Supported by the National Natural Sciences Foundation of China (grant numbers 81872707, 82025030, 82003550, and 82230111).

doi: 10.46234/ccdcw2024.104

# Corresponding author: Xiaoming Shi, shixm@chinacdc.cn.

<sup>1</sup> Department of Big Data in Health Science, School of Public Health, Zhejiang University, Hangzhou City, Zhejiang Province, China; <sup>2</sup> China CDC Key Laboratory of Environment and Population Health, National Institute of Environmental Health, Chinese Center for Disease Control and Prevention, Beijing, China; <sup>3</sup> Center for Global Health, School of Public Health, Nanjing Medical University, Nanjing City, Jiangsu Province, China; <sup>4</sup> Department of Epidemiology and Biostatistics, School of Public Health, Jilin University, Changchun City, Jilin Province, China; <sup>5</sup> School of Public Health, China Medical University, Shenyang City, Liaoning Province, China; <sup>6</sup> Institute of Environmental Health, School of Public Health, and Bioelectromagnetics Laboratory, School of Medicine, Zhejiang University, Hangzhou City, Zhejiang Province, China; <sup>7</sup> Environmental Research Center, Duke Kunshan University, Kunshan City, Jiangsu Province, China; <sup>8</sup> Nicholas School of the Environment, Duke University, Durham, NC, USA; <sup>9</sup> School of Public Health, Institute of Environment and Population Health, Anhui Medical University, Hefei City, Anhui Province, China; <sup>10</sup> School of Public Health and Social Work, Queensland University of Technology, Brisbane, Australia.

Submitted: November 28, 2023; Accepted: February 18, 2024

## REFERENCES

1. Lv YB, Mao C, Yin ZX, Li FR, Wu XB, Shi XM. Healthy ageing and biomarkers cohort study (HABCS): a cohort profile. *BMJ Open* 2019;9(10):e026513. <https://doi.org/10.1136/bmjopen-2018-026513>.
2. Cui GH, Yao YH, Xu RF, Tang HD, Jiang GX, Wang Y, et al. Cognitive impairment using education-based cutoff points for CMMSE scores in elderly Chinese people of agricultural and rural Shanghai China. *Acta Neurol Scand* 2011;124(6):361 – 7. <https://doi.org/10.1111/j.1600-0404.2010.01484.x>.
3. Wang XD, Wang R, Zhang ZY, Luo C, Zhao ZX, Ruan JP, et al. Level-specific associations of urinary antimony with cognitive function in US older adults from the National Health and Nutrition Examination Survey 2011–2014. *BMC Geriatr* 2022;22(1):663. <https://doi.org/10.1186/s12877-022-03351-6>.
4. Gerardo B, Cabral Pinto M, Nogueira J, Pinto P, Almeida A, Pinto E, et al. Associations between trace elements and cognitive decline: an exploratory 5-year follow-up study of an elderly cohort. *Int J Environ Res Public Health* 2020;17(17):6051. <https://doi.org/10.3390/ijerph17176051>.
5. Paglia G, Miedico O, Cristofano A, Vitale M, Angiolillo A, Chiaravalle AE, et al. Distinctive pattern of serum elements during the progression of Alzheimer's disease. *Sci Rep* 2016;6:22769. <https://doi.org/10.1038/srep22769>.
6. Tanu T, Anjum A, Jahan M, Nikkon F, Hoque M, Roy AK, et al. Antimony-induced neurobehavioral and biochemical perturbations in mice. *Biol Trace Elem Res* 2018;186(1):199 – 207. <https://doi.org/10.1007/s12011-018-1290-5>.
7. Xu SY, Yang ZY, Zhi Y, Yu SL, Zhang T, Jiang JK, et al. The effects of antimony on Alzheimer's disease-like pathological changes in mice brain. *Sci Total Environ* 2021;760:143235. <https://doi.org/10.1016/j.scitotenv.2020.143235>.
8. Shi WW, Tang YF, Zhi Y, Li ZJ, Jiang JK, Zhu JF, et al. Akt inhibition-dependent downregulation of the Wnt/β-Catenin Signaling pathway contributes to antimony-induced neurotoxicity. *Sci Total Environ* 2020;737:140252. <https://doi.org/10.1016/j.scitotenv.2020.140252>.
9. Wang XK, Zhu PY, Xu SY, Liu YT, Jin Y, Yu SL, et al. Antimony, a novel nerve poison, triggers neuronal autophagic death via reactive oxygen species-mediated inhibition of the protein kinase B/mammalian target of rapamycin pathway. *Int J Biochem Cell Biol* 2019;114:105561. <https://doi.org/10.1016/j.biocel.2019.105561>.
10. Agency for Toxic Substances and Disease Registry. Toxicological profile for antimony. Atlanta (USA): U.S. Department of Health and Human Services; 2019. <https://wwwn.cdc.gov/TSP/ToxProfiles/ToxProfiles.aspx?id=332&tid=58>.

## SUPPLEMENTARY MATERIAL

### eMethods

#### Information on the Nine Longevity Regions of HABCS in 2017–2018

The nine regions mentioned are as follows: Laizhou City in Shandong Province, Zhongxiang City in Hubei Province, Mayang County in Hunan Province, Rudong County in Jiangsu Province, Sanshui District in Guangdong Province, Yongfu County in Guangxi Autonomous Region, Chengmai County in Hainan Province, Dujiangyan City in Sichuan Province, and Xiayi County in Henan Province.

#### Sample Size

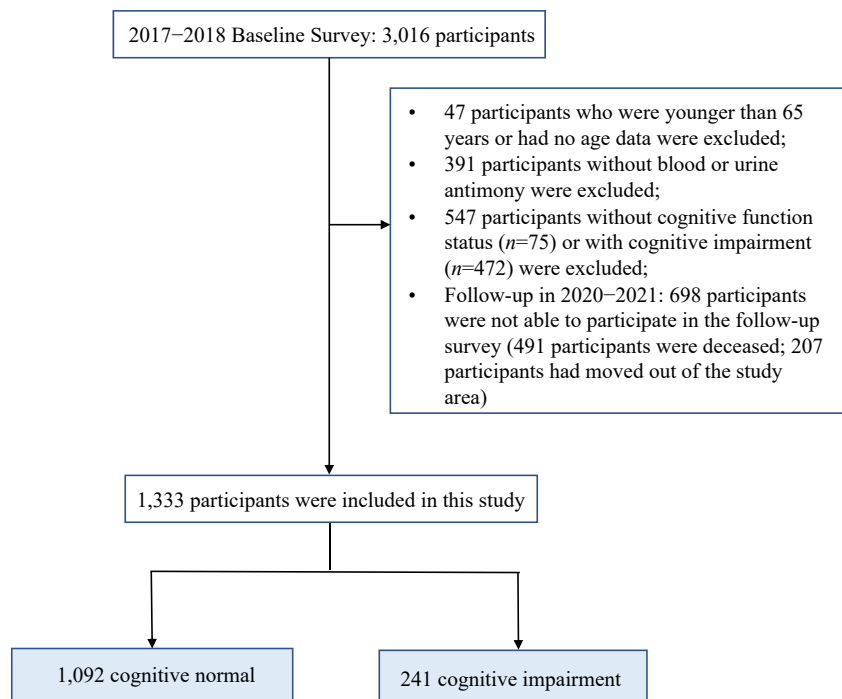
According to the previous cohort study conducted on older adults, the incidence of cognitive impairment over a span of 3 years was approximately 13.5%. The required sample size for the upcoming prospective cohort study was determined as follows:

$$n = \frac{(Z_{\alpha/2}\sqrt{2\bar{p}\bar{q}} + Z_{\beta}\sqrt{p_0q_0 + p_1q_1})^2}{(p_1 - p_0)^2} \quad (1)$$

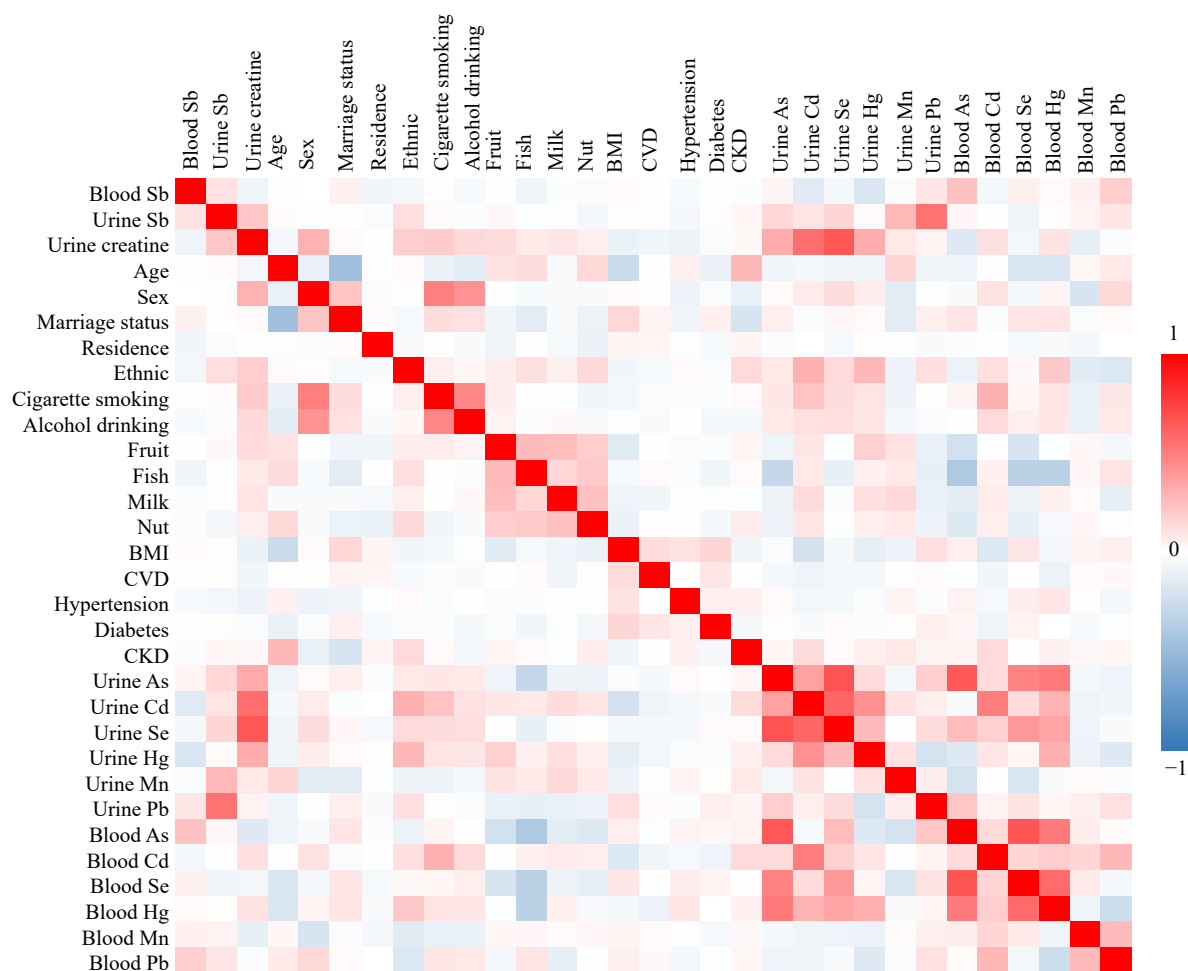
$p_0=0.135$ ,  $q_0=0.865$ ,  $\alpha=0.05$  (bilateral),  $\beta=0.10$ ,  $Z_{\alpha/2}=1.960$ ,  $Z_{\beta}=1.282$ . According to existing studies, the *OR* value between Sb exposure and cognitive impairment is estimated to be 0.402 (1),  $p_1=OR \times p_0 \approx 0.054$ ,  $q_1=1-p_1 \approx 0.946$ .  $\bar{p}=(p_1+p_0)/2 \approx 0.095$ ,  $\bar{q}=1-\bar{p}=0.905$ , substituting into the above formula, the maximum required sample  $n \approx 273$ . Considering a 20% loss of follow-up and death, the total sample size required for prospective cohort studies was  $273/(1-20\%) \times 2 \approx 683$ . This study plans to include 1,333 participants who are adults aged 65 years and older with normal baseline cognitive function. This sample size meets the estimated requirements.

#### Measurement of Antimony and Other Metals

Antimony and other metals were obtained from blood and urine samples collected from participants at baseline to assess their prior exposure. A trained phlebotomist collected 1 mL of blood with heparin and 4.5 mL of urine in the early morning after a fasting period of at least 12 hours. Blood and urine metal concentrations were measured using



SUPPLEMENTARY FIGURE S1. Flow chart depicting the inclusion of 1,333 participants from HABCS (2017–2021).



SUPPLEMENTARY FIGURE S2. Correlation map of independent variables and covariates among 1,333 Chinese older adults. Note: The values represent the coefficients obtained from Spearman's rank correlation analysis conducted among the covariates.

0.5 mL of blood and 1 mL of urine. For the analysis, 0.5 mL of blood was diluted with a 0.1% nitric acid and 0.01% Triton X-100 solution, while 1 mL of urine was diluted with a 1% nitric acid solution. The metal levels in the resulting supernatants were analyzed using centrifugal inductively coupled plasma mass spectrometry (ICP-MS). The LOD for blood antimony (B-Sb) was 0.07  $\mu\text{g/L}$ , and for urine antimony (U-Sb), it was 0.10  $\mu\text{g/L}$ . The LODs for other metals are provided in Supplementary Table S1. In this study, 1.23% of participants had B-Sb concentrations lower than the LOD, and 51.61% had U-Sb concentrations lower than the LOD. For Sb concentrations below the LODs, the concentrations were considered as half of the LOD.

### High, Medium and Low Definition of Sb Exposure Concentration

We categorized the participants into three groups based on their B-Sb levels: tertile 1 (low group) with B-Sb levels ranging from 0.04 to 2.45  $\mu\text{g/L}$  (reference), tertile 2 (medium group) with B-Sb levels ranging from 2.45 to 2.98  $\mu\text{g/L}$ , and tertile 3 (high group) with B-Sb levels ranging from 2.98 to 3.72  $\mu\text{g/L}$ . Since 51.38% of the U-Sb participants had values below the limit of detection (LOD), we considered these participants as the low group with U-Sb levels of 0.05  $\mu\text{g/L}$  or below (reference). The remaining participants were divided into the medium group with U-Sb levels ranging from 0.05 to 0.19  $\mu\text{g/L}$  and the high group with U-Sb levels ranging from 0.19 to 2.17  $\mu\text{g/L}$ , using the  $P_{75}$  dividing line.

### Covariate Collection and Definitions

The interviewers received formal training and used standardized questionnaires to collect data on

SUPPLEMENTARY TABLE S1. The limit of detections for other metals.

Metals	Limit of detections ( $\mu\text{g/L}$ )
Blood arsenic	0.40
Blood cadmium	0.07
Blood selenium	1.20
Blood mercury	0.20
Blood manganese	0.40
Blood lead	0.20
Urine arsenic	0.20
Urine cadmium	0.06
Urine selenium	1.10
Urine mercury	0.04
Urine manganese	0.20
Urine lead	0.10

sociodemographic characteristics, food consumption frequency, health characteristics, and metal exposure. Sociodemographic characteristics encompassed age, sex (men or women), ethnicity (Han or ethnic minorities), marital status (married or unmarried), and residence (urban or rural). Food consumption frequencies were documented for various items such as fruit, fish, milk, and nuts, with options ranging from almost every day to rarely or never. Health characteristics included urine creatine levels, cigarette smoking (yes or no), alcohol drinking (yes or no), body mass index (BMI), self-reported cardiovascular disease (yes or no), hypertension, self-reported diabetes (yes or no), and chronic kidney disease (CKD). BMI was categorized into four groups: underweight ( $<18.5 \text{ kg/m}^2$ ), normal weight ( $18.5\text{--}24.0 \text{ kg/m}^2$ ), overweight ( $24.0\text{--}28.0 \text{ kg/m}^2$ ), and obese ( $\geq 28.0 \text{ kg/m}^2$ ). BMI was calculated by dividing weight (kg) by the square of height ( $\text{m}^2$ ). Hypertension was defined as diastolic blood pressure measurements exceeding 90 mmHg and/or systolic blood pressure measurements exceeding 140 mmHg, or a diagnosis of hypertension given by a physician or healthcare provider. CKD was defined by an estimated glomerular filtration rate (eGFR) less than  $60 \text{ mL/min/1.73 m}^2$  or the presence of proteinuria.

### Cox Proportional Hazard Models for Blood Antimony and Urine Antimony

**Blood Antimony:** the crude model did not adjust for any covariates. Model 1 was adjusted for age, sex, ethnicity, marital status, and residence. Model 2 further adjusted for cigarette smoking, alcohol consumption, and dietary factors including fruit, fish, milk, and nut intake. Model 3 additionally adjusted for BMI and the presence of comorbidities such as CVD, hypertension, diabetes, and CKD. Finally, model 4 accounted for potential confounding factors by adding adjustments for blood As, blood Cd, blood Se, blood Hg, blood Pb, and blood Mn.

**Urine Antimony:** the crude model did not adjust for any covariates. Model 1 included adjustments for urine creatinine, age, sex, ethnicity, marital status, and residence. Model 2 further adjusted for factors such as cigarette smoking, alcohol consumption, and the intake of fruit, fish, milk, and nuts. Model 3 additionally adjusted for BMI, CVD, hypertension, diabetes, and CKD. Lastly, model 4 further adjusted for urine As, urine Cd, urine Se, urine Hg, urine Pb, and urine Mn.

### Subgroup Analysis

A subgroup analysis was performed to examine the potential impact of age (65–79 years old *vs.*  $\geq 80$  years old), sex (men *vs.* women), cigarette smoking (smoker *vs.* non-smoker), and alcohol drinking (drinker *vs.* non-drinker) on the outcomes. Multiplicative interaction effects were calculated.

### Sensitivity Analysis

Four additional sensitivity analyses were conducted to evaluate the robustness of our study findings. First, participants with two or more chronic diseases were excluded from the analysis due to their higher likelihood of experiencing cognitive impairment. Second, given that our study participants consisted of older adults, with over

SUPPLEMENTARY TABLE S2. Characteristics of 1,333 study participants described by cognitive functioning status at baseline.

Characteristics	Normal cognitive function (N=1,092)	Cognitive impairment (N=241)	Total (N=1,333)	P value
Age, mean±SD, years	77.2±8.1	86.4±9.4	78.9±9.1	<0.001
Sex, <i>n</i> (%)				0.004
Women	496 (45.4)	134 (55.6)	630 (47.3)	
Men	596 (54.6)	107 (44.4)	703 (52.7)	
Rural, <i>n</i> (%)	1,057 (97.6)	237 (98.8)	1,294 (97.8)	0.271
Married, <i>n</i> (%)	728 (67.2)	98 (41.4)	826 (62.6)	<0.001
Han, <i>n</i> (%)	945 (92.0)	198 (83.9)	1,143 (90.5)	<0.001
Cigarette smoking, <i>n</i> (%)	357 (32.8)	66 (27.5)	423 (31.9)	0.108
Alcohol drinking, <i>n</i> (%)	339 (31.2)	51 (21.3)	390 (29.5)	0.002
Frequency of fruit consumption, <i>n</i> (%)				0.049
Almost everyday	210 (19.3)	33 (13.8)	243 (18.3)	
Quite often	327 (30.1)	66 (27.6)	393 (29.6)	
Occasionally	366 (33.7)	85 (35.6)	451 (34.0)	
Rarely or never	184 (16.9)	55 (23.0)	239 (18.0)	
Frequency of fish consumption, <i>n</i> (%)				0.019
Almost everyday	87 (8.0)	7 (2.9)	94 (7.1)	
Not every day, but at least weekly	473 (43.5)	96 (39.8)	569 (42.8)	
Not every week, but at least monthly	253 (23.3)	60 (24.9)	313 (23.6)	
Not every month, but occasionally	150 (13.8)	42 (17.4)	192 (14.4)	
Rarely or never	125 (11.5)	36 (14.9)	161 (12.1)	
Frequency of milk consumption, <i>n</i> (%)				0.609
Almost everyday	167 (15.3)	33 (13.7)	200 (15.0)	
Not every day, but at least weekly	146 (13.4)	40 (16.6)	186 (14.0)	
Not every week, but at least monthly	112 (10.3)	21 (8.7)	133 (10.0)	
Not every month, but occasionally	147 (13.5)	29 (12.0)	176 (13.2)	
Rarely or never	516 (47.4)	118 (49.0)	634 (47.7)	
Frequency of nut consumption, <i>n</i> (%)				<0.001
Almost everyday	64 (5.9)	5 (2.1)	69 (5.2)	
Not every day, but at least weekly	138 (12.7)	26 (10.8)	164 (12.3)	
Not every week, but at least monthly	144 (13.2)	18 (7.5)	162 (12.2)	
Not every month, but occasionally	182 (16.7)	33 (13.8)	215 (16.2)	
Rarely or never	560 (51.5)	158 (65.8)	718 (54.1)	
BMI, <i>n</i> (%)				<0.001
Underweight	90 (8.3)	35 (14.9)	125 (9.5)	
Normal weight	527 (48.8)	136 (57.9)	663 (50.4)	
Overweight	353 (32.7)	46 (19.6)	399 (30.3)	
Obesity	110 (10.2)	18 (7.7)	128 (9.7)	
CVD, <i>n</i> (%)	192 (17.7)	35 (14.6)	227 (17.1)	0.247
Hypertension, <i>n</i> (%)	770 (71.0)	171 (72.8)	941 (71.3)	0.594
Diabetes, <i>n</i> (%)	64 (5.9)	8 (3.4)	72 (5.5)	0.121
CKD, <i>n</i> (%)	214 (20.2)	73 (31.6)	287 (22.2)	<0.001
Blood Sb, median (P <sub>25</sub> –P <sub>75</sub> ), µg/L	2.97 (2.46–3.73)	3.01 (2.43–3.68)	2.98 (2.45–3.72)	0.479

Continued

Characteristics	Normal cognitive function (N=1,092)	Cognitive impairment (N=241)	Total (N=1,333)	P value
Blood As, median (P <sub>25</sub> -P <sub>75</sub> ), µg/L	1.70 (0.87-4.90)	1.07 (0.63-2.36)	1.51 (0.80-4.45)	0.001
Blood Cd, median (P <sub>25</sub> -P <sub>75</sub> ), µg/L	1.31 (0.69-2.89)	1.19 (0.62-2.33)	1.28 (0.68-2.86)	0.014
Blood Se, median (P <sub>25</sub> -P <sub>75</sub> ), µg/L	112.79 (91.37-139.50)	96.53 (79.74-121.55)	109.38 (88.32-135.37)	<0.001
Blood Hg, median (P <sub>25</sub> -P <sub>75</sub> ), µg/L	1.72 (0.77-2.93)	1.21 (0.31-2.37)	1.61 (0.72-2.87)	<0.001
Blood Pb, median (P <sub>25</sub> -P <sub>75</sub> ), µg/L	33.88 (23.19-55.94)	34.27 (22.07-59.53)	33.97 (23.00-56.12)	0.886
Blood Mn, median (P <sub>25</sub> -P <sub>75</sub> ), µg/L	10.56 (8.45-13.22)	10.42 (8.73-12.94)	10.53 (8.49-13.19)	0.635
Urine Sb, median (P <sub>25</sub> -P <sub>75</sub> ), µg/L	0.05 (0.05-0.18)	0.11 (0.05-0.20)	0.05 (0.05-0.19)	0.248
Urine As, median (P <sub>25</sub> -P <sub>75</sub> ), µg/L	35.29 (17.67-78.04)	26.94 (14.26-53.63)	33.44 (16.83-72.26)	0.017
Urine Cd, median (P <sub>25</sub> -P <sub>75</sub> ), µg/L	0.95 (0.49-1.92)	0.75 (0.42-1.99)	0.91 (0.48-1.94)	0.604
Urine Se, median (P <sub>25</sub> -P <sub>75</sub> ), µg/L	18.37 (10.77-29.51)	15.37 (9.50-23.61)	18.02 (10.45-27.88)	0.012
Urine Hg, median (P <sub>25</sub> -P <sub>75</sub> ), µg/L	0.32 (0.06-0.82)	0.36 (0.02-0.81)	0.33 (0.05-0.81)	0.663
Urine Pb, median (P <sub>25</sub> -P <sub>75</sub> ), µg/L	6.89 (3.10-14.68)	6.42 (3.00-11.56)	6.69 (3.05-14.31)	0.113
Urine Mn, median (P <sub>25</sub> -P <sub>75</sub> ), µg/L	0.51 (0.10-1.16)	0.83 (0.36-1.94)	0.55 (0.10-1.24)	0.057
Urine creatine, median (P <sub>25</sub> -P <sub>75</sub> ), mg/dL	0.88 (0.55-1.27)	0.85 (0.57-1.33)	0.87 (0.55-1.28)	0.644

Note: Data were presented as the frequency (percentage) for categorical variables, and mean±SD for age, the metal concentrations, and urine creatine are expressed in terms of median (P<sub>25</sub>-P<sub>75</sub>).

Abbreviation: BMI=body mass index; Sb=antimony; As=arsenic; Cd=cadmium; Se=selenium; Hg=mercury; Pb=lead; Mn=manganese; SD=standard deviation; IQR=interquartile range.

SUPPLEMENTARY TABLE S3. Sensitivity analysis: Association of antimony with cognitive impairment among Chinese older adults from 2017 to 2021 (Excluding individuals with comorbidities, n=940).

Antimony	HR (95% CI)				
	Crude model	Model 1	Model 2	Model 3	Model 4
Ln-transformed B-Sb <sup>§</sup>	1.373 (0.929, 2.028)	1.686 (1.047, 2.717)*	1.562 (0.987, 2.472)	1.525 (0.963, 2.413)	1.797 (1.193, 2.709)*
Categorical by concentration					
Low group	1.000 Reference				
Medium group	0.829 (0.556, 1.234)	0.915 (0.611, 1.370)	0.953 (0.629, 1.442)	0.998 (0.658, 1.515)	1.085 (0.707, 1.664)
High group	1.178 (0.803, 1.729)	1.483 (1.000, 2.199)*	1.335 (0.893, 1.998)	1.291 (0.857, 1.944)	1.371 (0.897, 2.096)
P for trend	0.421	0.060	0.176	0.236	0.152
Ln-transformed U-Sb <sup>¶</sup>	1.418 (1.168, 1.721) <sup>†</sup>	1.385 (1.114, 1.722) <sup>†</sup>	1.403 (1.109, 1.776) <sup>†</sup>	1.437 (1.129, 1.829) <sup>†</sup>	1.504 (1.138, 1.990) <sup>†</sup>
Categorical by concentration					
Low group	1.000 Reference				
Medium group	1.961 (1.320, 2.915) <sup>†</sup>	1.740 (1.135, 2.666)*	1.590 (1.010, 2.502)*	1.695 (1.064, 2.699)*	1.498 (0.922, 2.434)
High group	1.956 (1.300, 2.942) <sup>†</sup>	1.972 (1.257, 3.094) <sup>†</sup>	1.980 (1.229, 3.189) <sup>†</sup>	2.047 (1.256, 3.337) <sup>†</sup>	2.245 (1.316, 3.830) <sup>†</sup>
P for trend	<0.001	0.002	0.004	0.003	0.003

Abbreviation: B-Sb=blood antimony; U-Sb=urine antimony; HR=hazard ratio; CI=confidence interval.

\* Denotes statistical significance at P<0.05;

<sup>†</sup> Denotes statistical significance at P<0.01.

<sup>§</sup> low group (0.04≤B-Sb≤2.45 µg/L), medium group (2.45<B-Sb≤2.98 µg/L), high group (2.98<B-Sb≤3.72 µg/L); Model 1 was adjusted for age, sex, ethnicity, marriage status, and residence; Model 2 was further adjusted for cigarette smoking, alcohol drinking, the consumption of fruit, fish, milk, and nuts; Model 3 was further adjusted for BMI, CVD, hypertension, diabetes, and CKD; Model 4 was further adjusted for blood As, blood Cd, blood Se, blood Hg, blood Pb, and blood Mn.

<sup>¶</sup> low group (U-Sb≤0.05 µg/L), medium group (0.05<U-Sb≤0.19 µg/L), high group (0.19<U-Sb≤2.17 µg/L); Model 1 was adjusted for urine creatinine, age, sex, ethnicity, marriage status, and residence; Model 2 was further adjusted for cigarette smoking, alcohol drinking, the consumption of fruit, fish, milk, and nuts; Model 3 was further adjusted for BMI, CVD, hypertension, diabetes, and CKD; Model 4 was further adjusted for urine As, urine Cd, urine Se, urine Hg, urine Pb, and urine Mn.

SUPPLEMENTARY TABLE S4. Sensitivity analysis: Association of antimony with cognitive impairment (MMSE<18) among Chinese older adults from 2017 to 2021 ( $n=1,491$ ).

Antimony	HR (95% CI)				
	Crude model	Model 1	Model 2	Model 3	Model 4
Ln-transformed B-Sb <sup>§</sup>	1.393 (0.996, 1.949)	1.325 (0.916, 1.916)	1.314 (0.907, 1.904)	1.334 (0.892, 1.995)	1.535 (1.055, 2.232)*
Categorical by concentration					
Low group	1.000 Reference				
Medium group	0.930 (0.657, 1.316)	0.919 (0.644, 1.312)	0.953 (0.658, 1.380)	1.041 (0.702, 1.544)	1.082 (0.726, 1.613)
High group	1.317 (0.946, 1.835)	1.244 (0.882, 1.756)	1.274 (0.893, 1.816)	1.375 (0.946, 1.998)	1.479 (0.997, 2.195)
<i>P</i> for trend	0.098	0.196	0.172	0.092	0.052
Ln-transformed U-Sb <sup>¶</sup>	1.398 (1.180, 1.657) <sup>†</sup>	1.358 (1.123, 1.641) <sup>†</sup>	1.306 (1.068, 1.597) <sup>†</sup>	1.325 (1.071, 1.640) <sup>†</sup>	1.482 (1.138, 1.929) <sup>†</sup>
Categorical by concentration					
Low group	1.000 Reference				
Medium group	1.374 (0.953, 1.983)	1.206 (0.816, 1.783)	1.127 (0.739, 1.718)	1.356 (0.861, 2.137)	1.306 (0.820, 2.079)
High group	1.885 (1.343, 2.645) <sup>†</sup>	1.866 (1.282, 2.715) <sup>†</sup>	1.708 (1.150, 2.536) <sup>†</sup>	1.796 (1.169, 2.757) <sup>†</sup>	2.162 (1.297, 3.603) <sup>†</sup>
<i>P</i> for trend	<0.001	0.002	0.010	0.007	0.004

Abbreviation: B-Sb=blood antimony; U-Sb=urine antimony; HR=hazard ratio; CI=confidence interval.

\* denotes statistical significance at  $P<0.05$ .

<sup>†</sup> denotes statistical significance at  $P<0.01$ .

<sup>§</sup> low group ( $0.04\leq\text{B-Sb}\leq 2.45\ \mu\text{g/L}$ ), medium group ( $2.45<\text{B-Sb}\leq 2.98\ \mu\text{g/L}$ ), high group ( $2.98<\text{B-Sb}\leq 3.72\ \mu\text{g/L}$ ); Model 1 was adjusted for age, sex, ethnicity, marriage status, residence, and education; Model 2 was further adjusted for cigarette smoking, alcohol drinking, the consumption of fruit, fish, milk, and nuts; Model 3 was further adjusted for BMI, CVD, hypertension, diabetes, and CKD; Model 4 was further adjusted for blood As, blood Cd, blood Se, blood Hg, blood Pb, and blood Mn.

<sup>¶</sup> low group ( $\text{U-Sb}\leq 0.05\ \mu\text{g/L}$ ), medium group ( $0.05<\text{U-Sb}\leq 0.19\ \mu\text{g/L}$ ), high group ( $0.19<\text{U-Sb}\leq 2.17\ \mu\text{g/L}$ ); Model 1 was adjusted for urine creatinine, age, sex, ethnicity, marital status, residence, and education. Model 2 was further adjusted for cigarette smoking, alcohol drinking, the consumption of fruit, fish, milk, and nuts. Model 3 was further adjusted for BMI, CVD, hypertension, diabetes, and CKD. Model 4 was further adjusted for urine As, urine Cd, urine Se, urine Hg, urine Pb, and urine Mn.

SUPPLEMENTARY TABLE S5. Sensitivity analysis: Association of urine antimony with cognitive impairment among Chinese older adults from 2017 to 2021 (excluding individuals below the limit of detection).

Antimony	HR (95% CI)				
	Crude model	Model 1	Model 2	Model 3	Model 4
Ln-transformed U-Sb	1.157 (0.820, 1.633)	1.149 (0.810, 1.629)	1.179 (0.818, 1.700)	1.110 (0.740, 1.666)	1.515 (0.955, 2.402)
Categorical by concentration					
Tertile 1	1.000 Reference	1.000 Reference	1.000 Reference	1.000 Reference	1.000 Reference
Tertile 2	1.573 (0.974, 2.541)	1.535 (0.932, 2.527)	1.783 (1.058, 3.005)*	1.639 (0.941, 2.852)	1.623 (0.919, 2.866)
Tertile 3	1.433 (0.873, 2.353)	1.608 (0.954, 2.711)	1.765 (1.014, 3.073)*	1.680 (0.917, 3.078)	2.790 (1.410, 5.519) <sup>†</sup>
<i>P</i> for trend	0.177	0.078	0.044	0.088	0.003

Note: Model 1 was adjusted for urine creatinine, age, sex, ethnicity, marriage status and residence; Model 2 was further adjusted for cigarette smoking, alcohol drinking, the consumption of fruit, fish, milk, and nuts; Model 3 was further adjusted for BMI, CVD, hypertension, diabetes and CKD; Model 4 was further adjusted for urine As, urine Cd, urine Se, urine Hg, urine Pb, and urine Mn.

Abbreviation: U-Sb=urine antimony; HR=hazard ratio; CI=confidence interval.

\* denotes statistical significance at  $P<0.05$ .

<sup>†</sup> denotes statistical significance at  $P<0.01$ .

half of them being illiterate, we redefined cognitive impairment by using a different criterion. Specifically, a rrMMSE score  $\geq 18$  was considered indicative of normal cognitive function, while an MMSE score  $< 18$  denoted cognitive impairment. Third, to address the issue of a substantial proportion of the population having U-Sb levels below the LOD, these individuals were excluded from the analysis, and the analysis focused only on those with U-Sb levels above the LOD. Finally, recognizing that death can act as a competing event for cognitive impairment, a competitive risk model was employed to investigate the relationship between Sb exposure and cognitive impairment.

SUPPLEMENTARY TABLE S6. Sensitivity analysis: Association of antimony with cognitive impairment among Chinese older adults from 2017 to 2021 (using a competitive risk model,  $n=1,824$ ).

Antimony	HR (95% CI)				
	Crude model	Model 1	Model 2	Model 3	Model 4
Ln-transformed B-Sb <sup>†</sup>	1.058 (0.793, 1.411)	1.028 (0.762, 1.385)	1.001 (0.767, 1.305)	1.075 (0.774, 1.492)	1.157 (0.873, 1.532)
Categorical by concentration					
Low group	1.000 Reference	1.000 Reference	1.000 Reference	1.000 Reference	1.000 Reference
Medium group	0.974 (0.714, 1.329)	0.903 (0.657, 1.241)	0.835 (0.603, 1.156)	0.857 (0.607, 1.21)	0.886 (0.623, 1.26)
High group	1.088 (0.799, 1.482)	1.073 (0.777, 1.481)	1.016 (0.734, 1.408)	1.105 (0.782, 1.561)	1.085 (0.753, 1.562)
<i>P</i> for trend	0.599	0.671	0.919	0.578	0.671
Ln-transformed U-Sb <sup>§</sup>	1.164 (1.006, 1.347)*	1.119 (0.955, 1.311)	1.143 (0.958, 1.364)	1.171 (0.966, 1.419)	1.317 (1.053, 1.648)*
Categorical by concentration					
Low group	1.000 Reference	1.000 Reference	1.000 Reference	1.000 Reference	1.000 Reference
Medium group	1.363 (0.991, 1.873)	1.313 (0.935, 1.844)	1.252 (0.881, 1.78)	1.317 (0.902, 1.925)	1.372 (0.932, 2.018)
High group	1.348 (0.98, 1.856)	1.233 (0.877, 1.733)	1.271 (0.883, 1.829)	1.337 (0.892, 2.005)	1.595 (0.983, 2.588)
<i>P</i> for trend	0.036	0.164	0.164	0.129	0.046

Abbreviation: B-Sb=blood antimony; U-Sb=urine antimony; HR=hazard ratio; CI=confidence interval.

\* Denotes statistical significance at  $P<0.05$ .

<sup>†</sup> low group ( $0.04\leq\text{B-Sb}\leq 2.64\ \mu\text{g/L}$ ), medium group ( $2.64<\text{B-Sb}\leq 3.46\ \mu\text{g/L}$ ), high group ( $3.46<\text{B-Sb}\leq 13.77\ \mu\text{g/L}$ ); Model 1 was adjusted for age, sex, ethnicity, marriage status, residence, and education; Model 2 was further adjusted for cigarette smoking, alcohol drinking, the consumption of fruit, fish, milk, and nuts; Model 3 was further adjusted for BMI, CVD, hypertension, diabetes, and CKD; Model 4 was further adjusted for blood As, blood Cd, blood Se, blood Hg, blood Pb, and blood Mn.

<sup>§</sup> low group ( $\text{U-Sb}\leq 0.05\ \mu\text{g/L}$ ), medium group ( $0.05<\text{U-Sb}\leq 0.20\ \mu\text{g/L}$ ), high group ( $0.20<\text{U-Sb}\leq 2.17\ \mu\text{g/L}$ ); Model 1 was adjusted for urine creatinine, age, sex, ethnicity, marriage status, residence, and education; Model 2 was further adjusted for cigarette smoking, alcohol drinking, the consumption of fruit, fish, milk, and nuts; Model 3 was further adjusted for BMI, CVD, hypertension, diabetes, and CKD; Model 4 was further adjusted for urine As, urine Cd, urine Se, urine Hg, urine Pb, and urine Mn.

## REFERENCES

1. Wang XD, Wang R, Zhang ZY, Luo C, Zhao ZX, Ruan JP, et al. Level-specific associations of urinary antimony with cognitive function in US older adults from the National Health and Nutrition Examination Survey 2011-2014. *BMC Geriatr* 2022;22(1):663. <https://doi.org/10.1186/s12877-022-03351-6>.
2. Chen CM, Lu FC, Department of Disease Control Ministry of Health, PR China. The guidelines for prevention and control of overweight and obesity in Chinese adults. *Biomed Environ Sci* 2004;17 Suppl:1-36. <https://pubmed.ncbi.nlm.nih.gov/15807475/>.
3. Zhang LX, Wang F, Wang L, Wang WK, Liu BC, Liu J, et al. Prevalence of chronic kidney disease in China: a cross-sectional survey. *Lancet* 2012;379 (9818):815 – 22. [https://doi.org/10.1016/S0140-6736\(12\)60033-6](https://doi.org/10.1016/S0140-6736(12)60033-6).
4. Kao SL, Wang JH, Chen SC, Li YY, Yang YL, Lo RY. Impact of comorbidity burden on cognitive decline: a prospective cohort study of older adults with dementia. *Dement Geriatr Cogn Disord* 2021;50(1):43 – 50. <https://doi.org/10.1159/000514651>.
5. Zhang MY, Katzman R, Salmon D, Jin H, Cai GJ, Wang ZY, et al. The prevalence of dementia and Alzheimer's disease in Shanghai, China: impact of age, gender, and education. *Ann Neurol* 1990;27(4):428 – 37. <https://doi.org/10.1002/ana.410270412>.
6. Cui GH, Yao YH, Xu RF, Tang HD, Jiang GX, Wang Y, et al. Cognitive impairment using education-based cutoff points for CMMSE scores in elderly Chinese people of agricultural and rural Shanghai China. *Acta Neurol Scand* 2011;124(6):361 – 7. <https://doi.org/10.1111/j.1600-0404.2010.01484.x>.
7. Tombaugh TN, McIntyre NJ. The mini-mental state examination: a comprehensive review. *J Am Geriatr Soc* 1992;40(9):922 – 35. <https://doi.org/10.1111/j.1532-5415.1992.tb01992.x>.

## Preplanned Studies

## Potential Adverse Outcome Pathways of Chlorinated Organophosphate Flame Retardants

Meiyu Zhou<sup>1,8</sup>; Huilin Zhang<sup>2,8</sup>; Qi Xiao<sup>1</sup>; Kexin Li<sup>2</sup>; Xiaoting Li<sup>3,#</sup>; Haiyan Chu<sup>1,2,#</sup>

### Summary

#### What is already known about this topic?

Chlorinated organophosphate flame retardants (Cl-OPFRs) are frequently detected chemicals in the environment and biological samples, yet there is a lack of systematic evaluation regarding the adverse effects and toxicological mechanisms of Cl-OPFRs.

#### What is added by this report?

This study utilizes the adverse outcome pathway (AOP) framework to assess the health implications and mechanisms of Cl-OPFRs, identifying multi-system toxicity, with a particular emphasis on reproductive issues and the possible toxic mechanisms.

#### What are the implications for public health practice?

These results enhance knowledge of the health hazards linked to Cl-OPFRs, supporting the creation of focused risk evaluations and suitable regulatory actions.

Chlorinated organophosphate flame retardants (Cl-OPFRs) have frequently been detected at high levels in environment and in human biological specimens. As a result, the toxic effects associated with Cl-OPFR exposure warrant increased attention. It is crucial to move beyond merely evaluating carcinogenic or non-carcinogenic risks (1) and engage in a comprehensive discussion on potential adverse health effects and toxic mechanisms of Cl-OPFRs. The adverse outcome pathway (AOP) concept comprises molecular initiating events (MIEs), key events (KEs), and adverse outcomes (AOs), offering a mechanistic understanding of crucial events and biological pathways leading to AOs, thereby enhancing the efficacy of toxicity risk evaluations. Recent studies have confirmed the practicality of this framework (2). This study utilizes the AOP framework to assess the health implications and mechanisms of Cl-OPFRs by integrating existing toxicity data. The findings suggest that Cl-OPFR exposure can result in multi-system toxicity, with a particular emphasis on reproductive issues. Through molecular investigations using tools such as Cl-OPFRs-gene-phenotype-AO

framework and AOP-helpFinder, key molecular events (*IGF1*, *BAX*, *AR*, *MTOR*, and *PPARG*) linked to hormonal processes and reproductive system development were identified, indicating potential reproductive toxicity induction. This research enhances the understanding of the toxic effects, reproductive toxicity, and mechanisms associated with Cl-OPFRs.

Candidate genes, Gene Ontology (GO) terms, and pathways associated with Cl-OPFRs such as tris-(2-chloroethyl)-phosphate (TCEP), tris-(1-chloro-2-propyl)-phosphate (TCIPP), and tris-(1,3-dichloropropyl)-phosphate (TDCIPP), were identified from the Comparative Toxicogenomics Database (CTD, <http://ctdbase.org>) in February 2023 using the keywords “TCEP”, “TCIPP”, and “TDCIPP”. Target genes were those with more than three interactions. Target phenotypes were determined by overlapping phenotypes obtained from GO enrichment analysis with a significance threshold of  $P < 1 \times 10^{-3}$  and relevant phenotypes in the CTD database. The target phenotypes were categorized into three levels — subcellular, cellular, and systemic — based on the hierarchical structure of GO terms (2). The study first identified AOs affecting individuals or populations as a result of exposure to Cl-OPFRs, prioritizing both biological importance and phenotype classification. Phenotypes that showed strong correlations with AOs were then selected as potential intermediate KEs. Additionally, genes associated with these KEs were identified as MIEs to construct an AOP framework. To prioritize MIEs and KEs, we developed chemical-gene-phenotype-disease frameworks utilizing Cytoscape software (version 3.9.1, Boston, MA, USA). We utilized AOP-helpFinder (<http://aop-helpfinder-v2.u-paris-sciences.fr/>) to identify relevant knowledge linking stressors automatically and events within an AOP and to assess potential candidate genes simultaneously. The assessment was conducted according to Organization for Economic Co-operation and Development (OECD) guidelines utilizing Weight of Evidence (WoE) methodology based on Bradford Hill’s causal considerations, composite score, and

confidence score. The aim was to bolster credibility by consolidating evidence from PubMed, Web of Science, and the AOP Wiki (<https://aopwiki.org/>). WoE criteria primarily focus on biological plausibility and empirical support, incorporating mode of action analysis in chemical regulatory practices. Biological plausibility underscores mechanistic relationships, while empirical support leans on experimental data, particularly dose-response concordance.

Given the widespread presence and long-lasting nature of Cl-OPFRs in the environment, the AOP framework extensively outlined the harmful effects of Cl-OPFRs. A flow diagram depicting this is presented in Figure 1A. Seventy-four interactive genes with Cl-OPFRs effects and 531 shared phenotypes (comprising 483 GO terms and 48 pathways) were identified. These phenotypes were categorized into three levels based on the GO ancestor chart. Notably, at the system level, reproductive toxicity-related phenotypes constituted 43.59% of the total GO terms, followed by organ growth and development at 28.21%, Motor system at 7.69%, and others, indicating potential multi-system toxicity from Cl-OPFRs exposure (Figure 1B). Moreover, an in-depth analysis highlighted that genes such as *IL1B*, *BAX*, and *BCL2* showed higher frequencies within toxic pathways

related to reproduction, while the *IGF1* gene emerged as a crucial factor across all levels (Supplementary Table S1, available at <https://weekly.chinacdc.cn/>).

Reproductive toxicity phenotypes were notably prevalent and thus selected as the AO for the establishment of an AOP framework. Reproductive toxicology terms were classified into 14 categories across three levels of biological organization based on thematic similarities (Supplementary Table S2, available at <https://weekly.chinacdc.cn/>). At the cellular and subcellular levels, the principal categories included hormone-related phenotypes encompassing biological processes and hormonal stimulation, phenotypes associated with cell damage pertaining to the regulation of cell proliferation and cell cycle, and oxidative stress. At the systemic level, out of 17 reproductive system-related phenotypes, 6 were specifically linked to female reproductive health, whereas only 2 pertained to male reproduction. This discrepancy indicates a potentially higher reproductive toxicity risk from Cl-OPFRs for females. The interconnected phenotypes across the three organizational levels constituted the KEs, and 74 genes identified as interacting with these phenotypes were designated as MIEs, thus forming the foundational structure of the AOP (Figure 2).

To assign priority to MIEs and KEs, we utilized a

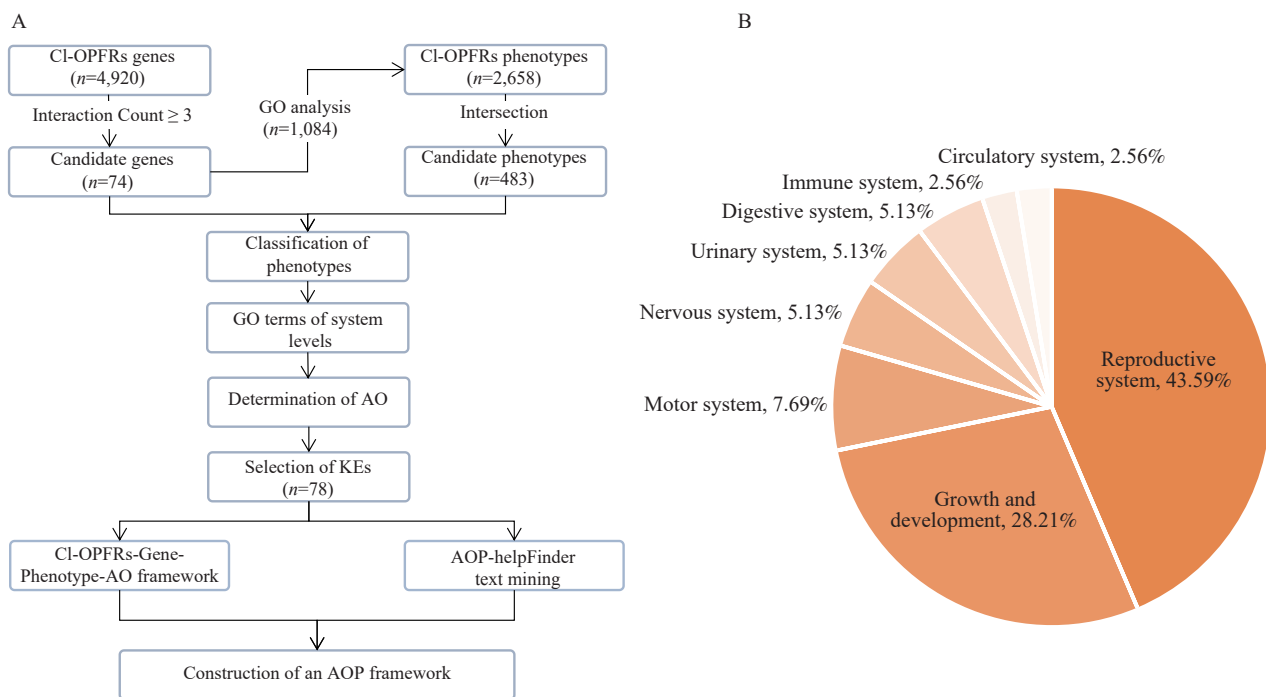


FIGURE 1. The strategy for the construction of the AOP framework. (A) The flow diagram for the construction of the AOP framework. (B) Percentage of GO terms at the system level. Abbreviation: Cl-OPFRs=chlorinated organophosphate flame retardants; AOP=adverse outcome pathway; GO=gen ontology; AO=adverse outcome.

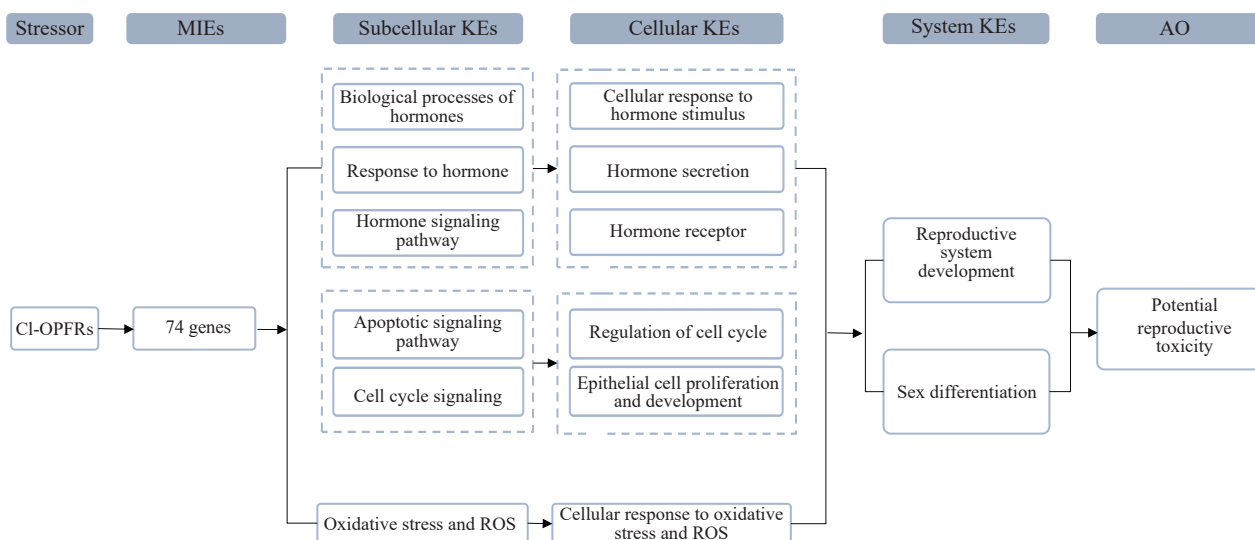


FIGURE 2. AOP framework of CI-OPFRs-induced potential reproductive toxicity.

Abbreviation: AOP=adverse outcome pathway; CI-OPFRs=chlorinated organophosphate flame retardants; MIEs=molecular initiating events; KEs=key events; AO=adverse outcome; ROS=reactive oxygen species.

dataset comprising 74 genes and 8 phenotypic metrics to develop a CI-OPFRs-gene-phenotype-AO network, consisting of 84 nodes and 434 connections (Figure 3A). The relevance of each gene and phenotype within the network was determined by tallying the number of their connections. The AOP-helpFinder tool leveraged PubChem to compile alternate names for the three CI-OPFRs identified as stressors, as well as the 11 genes that featured prominently in the gene-phenotype network analysis due to high connectivity. Notably, the genes *IGF1*, *BAX*, *AR*, *MTOR*, and *PPARG* showcased significant associations with CI-OPFRs exposure (Supplementary Table S3, available at <https://weekly.chinacdc.cn/>). Subsequently, we crafted an AOP model delineating the putative role of CI-OPFRs in reproductive toxicity, structured around the hierarchical and biological interplay between these components (Figure 3B). The proposed AOP model posits that the expression of the five aforementioned MIEs is disrupted upon exposure to CI-OPFRs, which in turn perturbs biological processes and hormone-mediated pathways, potentially compromising reproductive development and culminating in reproductive toxicity. To evaluate the robustness of this AOP model, we conducted a WoE assessment in accordance with the OECD Handbook, which entailed scrutinizing the AOP Wiki and relevant literature. As indicated in Supplementary Tables S4 and S5 (available at <https://weekly.chinacdc.cn/>), the significance of the KEs and the validity of the inter-KE relationships were judged to fall within the “moderate”

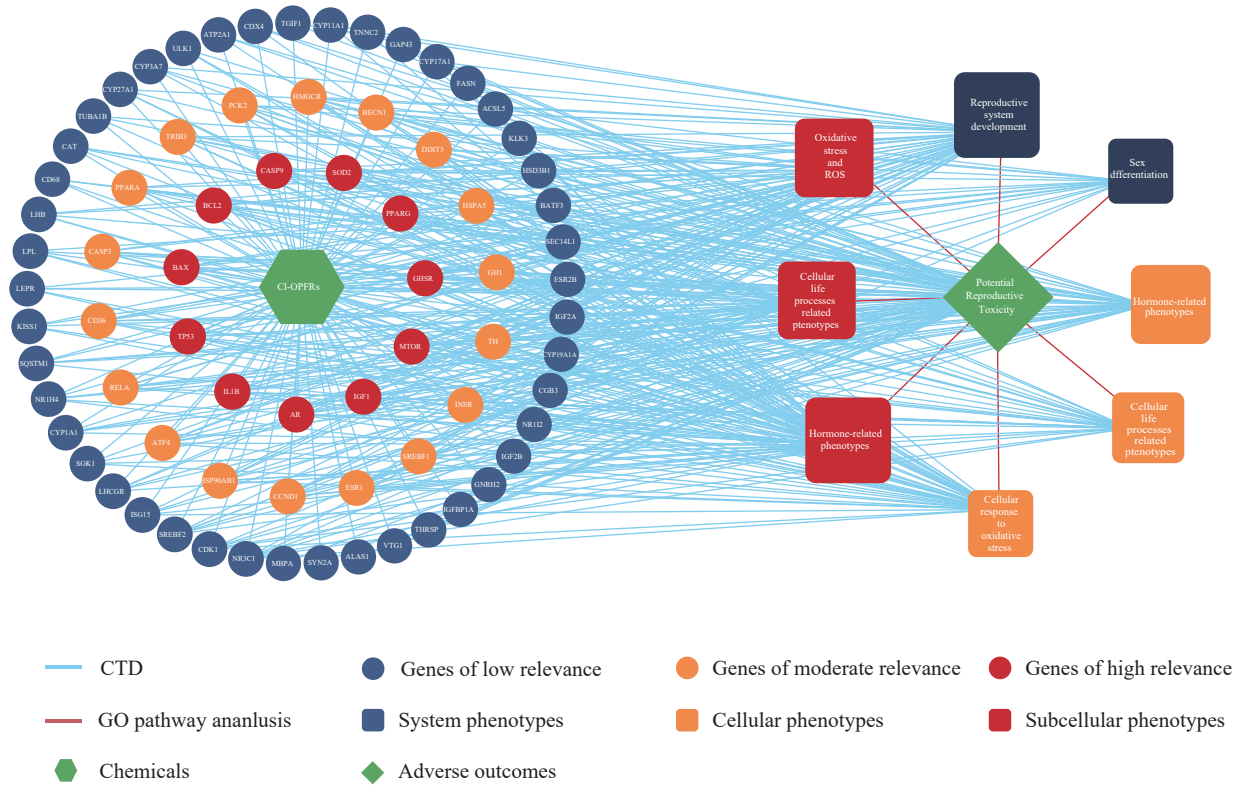
to “high” range, based on criteria such as biological plausibility and supportive experimental and epidemiological studies. In summary, the presented AOP model is characterized by a relatively high degree of credibility.

## DISCUSSION

The study results indicated that CI-OPFRs may lead to toxicity affecting multiple systems, with a focus on reproductive toxicity. The AOP framework suggested that CI-OPFRs could impact the expression of crucial genes such as *IGF1*, *BAX*, *AR*, *MTOR*, and *PPARG*, leading to hormone-related effects that impact reproductive system development and indicating potential reproductive toxicity concerns.

Due to their high production volumes, extensive use, and environmental persistence, the toxic effects of CI-OPFRs across different species have been under scrutiny (3). Despite this interest, a comprehensive assessment of CI-OPFR toxicity and its underlying biological mechanisms remains elusive. The OECD has launched a project to create AOPs that consolidate existing toxicity data to enhance predictions of chemical toxicity, clarify the mechanisms of action, and inform regulatory decisions for hazardous substances (4). Utilizing the AOP framework, which includes data from the CTD, network-based strategies, and an extensive literature review, we investigated the connection between CI-OPFR exposure and adverse health outcomes. Our AOP model revealed that CI-

A



B

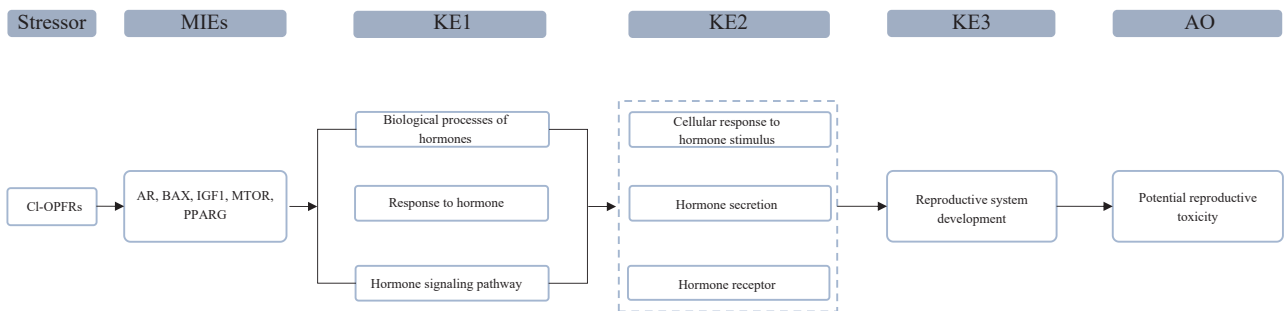


FIGURE 3. CI-OPFRs-gene-phenotype-AO framework. The green hexagon node represents CI-OPFRs; the green diamond node represents potential reproductive toxicity; the round nodes represent target genes, with their proximity to the center of the circle indicating their relative contribution to the framework; the blue rectangle nodes represent system phenotypes, while orange rectangle nodes represent cellular phenotypes, and red rectangle nodes represent subcellular phenotypes. The size of the rectangle reflects the magnitude of their impact on the framework. In total, 434 links extracted from the CTD, and GO and KEGG pathway enrichment analyses are presented as different connections among the nodes. Abbreviation: CI-OPFRs=chlorinated organophosphate flame retardants; CTD=Comparative Toxicogenomics Database; MIEs=molecular initiating events; KEs=key events; GO=gene ontology; AO=adverse outcome; ROS=reactive oxygen species.

OPFRs are linked to multiple systemic toxicities, including those affecting growth and development, motor function, neurology, and particularly reproduction. Empirical evidence supports these findings, such as research demonstrating the ability of TCEP to affect survival, growth, and induce

histological alterations in juvenile fish (5). Additionally, instances of spinal curvature and muscle malformations in zebrafish have been associated with exposure to TDCIPP (6).

Given the importance of reproductive toxicity, a comprehensive framework linking CI-OPFRs with

genes, phenotypes, and AOs was developed. This framework is justified by previous studies demonstrating the endocrine-disrupting and reproductive toxicity potential of Cl-OPFRs. For example, Cl-OPFRs can interfere with the androgen receptor (AR) activity (7), leading to disruptions in hormone-related receptors and affecting genes involved in steroid hormone biosynthesis, ultimately causing adverse reproductive effects (8). These effects include decreased sperm concentrations and motility in males, increased risks of fetal chromosome abnormalities and spontaneous abortion in females post-Cl-OPFR exposure (9–10), with supporting evidence for KEs in this pathway.

Although potential adverse effects have been identified, the study has several limitations. First, this study only focuses on comprehensively analyzing the data of the CTD database by constructing the AOP. Second, the findings are not validated in the biological experiments. However, it is worth noting that this study can enhance our understanding of the relationship between Cl-OPFRs and human reproductive toxicity, and it is advised that large multicenter national cohorts confirm our results.

**Conflicts of interest:** No conflicts of interest.

**Funding:** Supported by the Natural Science Foundation of Jiangsu Province (grant number 22KJA330002), Collaborative Innovation Center for Cancer Personalized Medicine, and the Priority Academic Program Development of Jiangsu Higher Education Institutions in the Field of Public Health and Preventive Medicine.

**doi:** 10.46234/ccdcw2024.105

\* Corresponding authors: Xiaoting Li, [xiaotingli@njmu.edu.cn](mailto:xiaotingli@njmu.edu.cn); Haiyan Chu, [chy\\_grape@njmu.edu.cn](mailto:chy_grape@njmu.edu.cn).

<sup>1</sup> Department of Environmental Genomics, Jiangsu Key Laboratory of Cancer Biomarkers, Prevention and Treatment, Collaborative Innovation Center for Cancer Personalized Medicine, School of Public Health, Nanjing Medical University, Nanjing City, Jiangsu Province, China; <sup>2</sup> Department of Genetic Toxicology, The Key Laboratory of Modern Toxicology of Ministry of Education, Center of Global Health, School of Public Health, Nanjing Medical University, Nanjing

City, Jiangsu Province, China; <sup>3</sup> Department of Nutrition and Food Safety, School of Public Health, Nanjing Medical University, Nanjing City, Jiangsu Province, China.

<sup>&</sup> Joint first authors.

Submitted: January 06, 2024; Accepted: April 15, 2024

## REFERENCES

- Dou MS, Wang LJ. A review on organophosphate esters: physiochemical properties, applications, and toxicities as well as occurrence and human exposure in dust environment. *J Environ Manage* 2023;325:116601. <https://doi.org/10.1016/j.jenvman.2022.116601>.
- Zhu HH, Zhang HL, Lu K, Yang S, Tang XY, Zhou MY, et al. Chlorinated organophosphate flame retardants impair the lung function via the IL-6/JAK/STAT signaling pathway. *Environ Sci Technol* 2022;56(24):17858–69. <https://doi.org/10.1021/acs.est.2c05357>.
- Feng YX, Cui X, Yin J, Shao B. Chlorinated organophosphorus flame retardants-induced mitochondrial abnormalities and the correlation with progesterone production in mLTC-1 cells. *Food Chem Toxicol* 2022;169:113432. <https://doi.org/10.1016/j.fct.2022.113432>.
- Wang XQ, Li F, Teng YF, Ji CL, Wu HF. Potential adverse outcome pathways with hazard identification of organophosphate esters. *Sci Total Environ* 2022;851(Pt 1):158093. <http://dx.doi.org/10.1016/j.scitotenv.2022.158093>.
- Hu FX, Zhao YX, Yuan Y, Yin L, Dong FL, Zhang WN, et al. Effects of environmentally relevant concentrations of tris (2-chloroethyl) phosphate (TCEP) on early life stages of zebrafish (*Danio rerio*). *Environ Toxicol Pharmacol* 2021;83:103600. <https://doi.org/10.1016/j.etap.2021.103600>.
- Rhyu D, Lee H, Tanguay RL, Kim KT. Tris(1,3-dichloro-2-propyl) phosphate (TDCIPP) disrupts zebrafish tail fin development. *Ecotoxicol Environ Saf* 2019;182:109449. <https://doi.org/10.1016/j.ecoenv.2019.109449>.
- Rosenmai AK, Winge SB, Möller M, Lundqvist J, Wedebye EB, Nikolov NG, et al. Organophosphate ester flame retardants have antiandrogenic potential and affect other endocrine related endpoints *in vitro* and *in silico*. *Chemosphere* 2021;263:127703. <https://doi.org/10.1016/j.chemosphere.2020.127703>.
- Kojima H, Takeuchi S, Itoh T, Iida M, Kobayashi S, Yoshida T. In vitro endocrine disruption potential of organophosphate flame retardants via human nuclear receptors. *Toxicology* 2013;314(1):76–83. <https://doi.org/10.1016/j.tox.2013.09.004>.
- Siddique S, Farhat I, Kubwabo C, Chan P, Goodyer CG, Robaire B, et al. Exposure of men living in the greater Montreal area to organophosphate esters: association with hormonal balance and semen quality. *Environ Int* 2022;166:107402. <https://doi.org/10.1016/j.envint.2022.107402>.
- Li YT, Wang X, Zhu QQ, Xu YQ, Fu QG, Wang T, et al. Organophosphate flame retardants in pregnant women: sources, occurrence, and potential risks to pregnancy outcomes. *Environ Sci Technol* 2023;57(18):7109–28. <https://doi.org/10.1021/acs.est.2c06503>.

## SUPPLEMENTARY MATERIAL

SUPPLEMENTARY TABLE S1. The frequency of genes occurring more than one time in each system.

System	Related genes (Counts)
Reproductive system development	<i>IL1B</i> (7), <i>BAX</i> (6), <i>BCL2</i> (5), <i>AR</i> (3), <i>GHSR</i> (3), <i>HMGCR</i> (3), <i>IGF1</i> (3), <i>MTOR</i> (3), <i>NR1H4</i> (3), <i>PCK2</i> (3), <i>PPARA</i> (3), <i>PPARG</i> (3), <i>SREBF1</i> (3), <i>TP53</i> (3), <i>ATF4</i> (2), <i>CASP9</i> (2), <i>CD36</i> (2>), <i>CYP11A1</i> (2), <i>CYP17A1</i> (2), <i>DDIT3</i> (2), <i>ESR1</i> (2), <i>KISS1</i> (2), <i>LHB</i> (2), <i>NR3C1</i> (2), <i>RELA</i> (2), <i>SOD2</i> (2), <i>SREBF2</i> (2)
Growth and development	<i>NR1H4</i> (4), <i>CD36</i> (3), <i>IGF1</i> (3), <i>IL1B</i> (3), <i>MTOR</i> (3), <i>PCK2</i> (3), <i>TP53</i> (3), <i>BAX</i> (2), <i>BECN1</i> (2), <i>CASP9</i> (2), <i>DDIT3</i> (2), <i>GHSR</i> (2), <i>HMGCR</i> (2), <i>PPARA</i> (2), <i>SREBF1</i> (2)
Motor system	<i>PPARA</i> (2), <i>TP53</i> (2)
Urinary system	<i>IGF1</i> (2)
Digestive system	<i>IGF1</i> (2)

SUPPLEMENTARY TABLE S2. Classification of phenotypes.

Classification	Ancestor terms	Phenotypes	Related genes
System	Reproductive system development	Gland development, Mammary gland development, Prostate gland growth, Reproductive structure development, Reproductive system development, Prostate gland development, Genitalia development, Urogenital system development, Developmental maturation, Mammary gland branching involved in pregnancy, Mammary gland duct morphogenesis, Gonad development, Female gonad development	<i>AR/ATF4/BATF3/BAX/BCL2/CASP3/CASP9/CCND1/CYP11A1/CYP17A1/CYP1A1/CYP27A1/CYP3A7/ESR1/FASN/GH1/GHSR/HMGCR/HSP90AB1/IGF1/IL1B/INSR/KISS1/LHB/LHCGR/MTOR/NR1H4/NR3C1/PCK2/PPARA/PPARG/RELA/SGK1/SOD2/SREBF1/SREBF2/TGIF1/TH/TP53/TRIB3</i>
	Sex differentiation	Sex differentiation, Development of primary sexual characteristics, Female sex differentiation, Development of primary female sexual characteristics	<i>ACSL5/ATF4/BAX/BECN1/CASP9/CD36/DIT3/IL1B/LEPR/LPL/NR3C1/PCK2/PPARG/SREBF2/TP53</i>
	Cellular response to hormone stimulus	Cellular response to peptide hormone stimulus, Cellular response to steroid hormone stimulus	<i>ATF4/ATP2A1/BAX/BCL2/BECN1/CASP3/CASP9/CD36/CD68/DDIT3/GHSR/HSPA5/IL1B/RELA/SOD2/TP53/TRIB3</i>
	Hormone secretion	Hormone transport, Hormone secretion, Peptide hormone secretion	<i>ATF4/BAX/BCL2/BECN1/CCND1/CDK1/CYP1A1/HSPA5/IGF1/IL1B/INSR/PPARG/QSTM1/SREBF1/SREBF2/TP53</i>
Cellular	Hormone receptor	Nuclear receptor binding, Nuclearreceptor activity	<i>AR/ATF4/BCL2/BECN1/CASP9/CAT/CD68/CDK1/CDX4/CYP1A1/DDIT3/ESR1/HMGCR/MTOR/NR1H4/NR112/NR3C1/PPARA/RELA/SOD2/SREBF1/TH/TP53</i>
	Regulation of cell cycle	Regulation of mitotic cell cycle, Negative regulation of cell cycle, Mitotic cell cycle phase transition, Negative regulation of the cell cycle process, Regulation of cell cycle phase transition, Regulation of mitotic cell cycle phase transition, Negative regulation of the mitotic cell cycle, Positive regulation of cell cycle, Negative regulation of cell cycle phase transition, Negative regulation of mitotic cell cycle phase transition, Positive regulation of the cell cycle process, G1/S transition of mitotic cell cycle, Cell cycle G1/S phase transition	<i>AR/ATF4/BAX/BCL2/BECN1/CASP3/CASP9/CD36/CDK1/CYP27A1/ESR1/GHSR/HMGCR/HSP90AB1/HSPA5/IGF1/IL1B/INSR/ISG15/LPL/MTOR/NR3C1/PCK2/PPARA/PPARG/SGK1/SOD2/SREBF1/TP53/TRIB3/ULK1</i>
	Epithelial cell proliferation and development	Epithelial cell proliferation, Epithelial cell development, Mammary gland epithelium development, Positive regulation of epithelial cell proliferation involved in prostate gland development, Positive regulation of epithelial cell proliferation	<i>AR/ATF4/BAX/BCL2/CASP3/DDIT3/GAP43/GHSR/HMGCR/HSP90AB1/HSPA5/IL1B/INSR/KISS1/LEPR/MTOR/NR1H4/PCK2/PPARG/SREBF1/TH/TP53</i>
	Cellular response to oxidative stress	Cellular response to oxidative stress, Cellular response to reactive oxygen species, Regulation of cellular response to oxidative stress, Negative regulation of oxidative stress-induced cell death, Cell death in response to oxidative stress, Cellular response to decreased oxygen levels	<i>AR/BCL2/BECN1/CASP9/CCND1/CD36/CDK1/GH1/GHSR/HSD3B1/HSP90AB1/IGF1/IL1B/INSR/MTOR/NR3C1/PCK2/PPARA/PPARG/RELA/SOD2/SREBF1/TH/TP53</i>

Continued

Classification	Ancestor terms	Phenotypes	Related genes
Subcellular	Biological processes of hormones	Steroid metabolic process, Steroid biosynthetic process	<i>AR/ATF4/BAX/BCL2/BECN1/CASP3/CASP9/CAT/CCND1/CD36/CD68/CDK1/CDX4/CYP11A1/CYP17A1/CYP1A1/CYP27A1/CYP3A7/ESR1/GH1/GHSR/HMGCR/HSD3B1/HSP90AB1/HSPA5/IL1B/INSR/ISG15/KISS1/KLK3/LEPR/LHB/LHCGR/LPL/MTOR/NR1H4/NR1I2/NR3C1/PCK2/PPARA/PPARG/RELA/SGK1/SOD2/SQSTM1/SREBF1/SREBF2/TH/TP53/TRIB3/TUBA1B/ULK1</i>
		Hormone metabolic process, Steroid hydroxylase activity, Steroid hormone biosynthetic process, Androgen metabolic process, Steroid binding, Hormone biosynthetic process, C21-steroid hormone metabolic process, Estrogen metabolic process, Steroid delta-isomerase activity, C21-steroid hormone biosynthetic process, Regulation of peptide hormone secretion, Regulation of hormone secretion	
	Response to hormone	Response to peptide hormone, Response to steroid hormone, Response to estradiol, response to corticosteroid	
	Hormone signaling pathway	Hormone-mediated signaling pathway, Steroid hormone-mediated signaling pathway, Intracellular steroid hormone receptor signaling pathway, ER-nucleus signaling pathway	
	Apoptotic signaling pathway	Regulation of apoptotic signaling pathway, Intrinsic apoptotic signaling pathway, Negative regulation of apoptotic signaling pathway, Regulation of intrinsic apoptotic signaling pathway, Intrinsic apoptotic signaling pathway in response to oxidative stress, Intrinsic apoptotic signaling pathway in response to endoplasmic reticulum stress, Positive regulation of intrinsic apoptotic signaling pathway, Extrinsic apoptotic signaling pathway, Regulation of extrinsic apoptotic signaling	
	Cell cycle signaling	Cell cycle checkpoint signaling, Mitotic cell cycle checkpoint signaling	
Oxidative stress and ROS	Response to oxidative stress, Response to reactive oxygen species, Positive regulation of reactive oxygen species metabolic process, Regulation of reactive oxygen species metabolic process, Reactive oxygen species metabolic process, Reactive oxygen species biosynthetic process	<i>CDK1/CYP1A1/CYP3A7/HMGCR/HSP90AB1/IGF1/IL1B/PCK2/SREBF2/TH/AR/ATF4/BAX/BCL2/BECN1/CASP3/CASP9/CCND1/CD36/DDIT3/ESR1/GH1/GHSR/HMGCR/HSP90AB1/HSPA5/IGF1/IL1B/INSR/ISG15/LHB/LHCGR/MTOR/PPARA/PPARG/RELA/SOD2/SQSTM1/SREBF1/TP53/TRIB3/TUBA1B</i>	

Abbreviation: ROS=reactive oxygen species.

SUPPLEMENTARY TABLE S3. Top genes with the most linkages in CI-OPFRs-gene-phenotype-AO framework and the top genes in the AOP-helpFinder text mining results.

CI-OPFRs-gene-phenotype-AO framework, Gene (degree)	AOP-helpFinder, Gene (average score)
<i>IL-1β</i> (10), <i>TP53</i> (10), <i>AR</i> (9), <i>BCL2</i> (9), <i>BAX</i> (9), <i>MTOR</i> (9), <i>IL-1β</i> (-), <i>TP53</i> (-), <i>AR</i> (26.2), <i>BCL2</i> (-), <i>BAX</i> (29.6), <i>MTOR</i> (8.2), <i>GHSR</i> (9), <i>PPARG</i> (9), <i>IGF1</i> (9), <i>CASP9</i> (9), <i>SOD2</i> (9)	<i>GHSR</i> (-), <i>PPARG</i> (4.9), <i>IGF1</i> (31.1), <i>CASP9</i> (-), <i>SOD2</i> (-)

Abbreviation: CI-OPFRs=chlorinated organophosphate flame retardants; AOP=adverse outcome pathway; AO=adverse outcome.

SUPPLEMENTARY TABLE S4. Assessment of the essentiality of KEs.

Events	Evidence	WoE	PMID
<b>MIE</b>			
<i>AR</i>	<i>AR</i> inhibition induced malformation of the male reproductive tract.	High	16417039
	Reduced <i>AR</i> expression caused reproductive disorders in rats.	High	32392119
	pAOP-9: Disrupted <i>AR</i> activity leads to altered follicle growth and impaired fertility.	High	32638039
<i>IGF1</i>	Reduced <i>IGF1</i> expression caused testicular dysplasia.	High	31141788
	Decreased <i>IGF1</i> -induced ovarian developmental toxicity.	High	29370380
<i>BAX</i>	Elevated <i>BAX</i> expression inhibits follicle growth.	High	16081520
	Driving <i>BAX</i> expression caused premature ovarian failure.	High	12488331
	High expression of <i>BAX</i> induced Loss of ovarian follicles.	High	11455387
<i>MTOR</i>	Activation of the <i>MTOR</i> pathway improved ovarian function.	Moderate	35300716
	Inhibition of spermatogenesis by <i>MTOR</i> activation.	Moderate	27296223
	DNA damage in duck testes caused by <i>MTOR</i> activation.	Moderate	36351481
<i>PPARG</i>	Agonistic <i>PPARG</i> -induced ovarian toxicity.	High	19265280
	Upregulation of <i>PPARG</i> had a protective effect on rat testes.	High	34890588
	Testicular injury in male mice disrupted <i>PPARG</i> levels.	Moderate	26219505
<b>KE1</b>			
Biological processes of hormones	C21-steroid hormone metabolism affects organ morphology and the development and function of the reproductive system.	High	23717070
Response to hormone	Transcriptome aberration in mice uterus was associated with steroid hormone response.	High	33971472
Hormone signaling pathway	Disruption of steroid hormone-related signaling pathways induced ovarian toxicity.	High	32610232
	pAOP-4: Disrupted ESR and AHR signaling led to disturbed primordial follicle formation and impaired fertility in females.	High	32638039
	pAOP-5: Disrupted AHR signaling leads to follicle atresia and premature ovarian insufficiency.	High	32638039
<b>KE2</b>			
Cellular response to hormone stimulus	Primary co-cultures of epithelial and stromal cells from human prostate carcinoma can response to hormone.	Moderate	15679620
Hormone secretion	Testosterone secretion induced anovulation and ovarian characteristics of PCOS in WT mice.	High	10.1016/j.coemr.2020.03.001
Hormone receptor	Mechanisms of sex-dependent reproductive toxicity due to estrogen receptor and androgen receptor antagonism.	High	34638023
	AOP-Wiki-19 Androgen receptor antagonism leads to adverse effects in the male fetus.	High	-
	AOP-Wiki-167 Early-life estrogen receptor activity leading to endometrial carcinoma in the mouse.	High	-
<b>KE3</b>			
Reproductive system development	Delayed development and further induction of ovarian reproductive toxicity in <i>Drosophila</i> .	High	37080472
	Zebrafish reproduction is inhibited, with reduced female spawning and slow growth of offspring reflecting reproductive toxicity.	Moderate	34638023
	Reproductive toxicity due to damage to gonadal development.	High	31398636

Abbreviation: AOP=adverse outcome pathway; MIEs=molecular initiating events; KEs=key events.

SUPPLEMENTARY TABLE S5. Assessment of the evidence supporting KERs.

KERs	Evidence	WoE	PMID
MIE to KE1	Disruption of androgen signaling by <i>AR</i> antagonists in utero.	Moderate	20487044
	<i>IGF1</i> perturbation causes abnormal steroid hormone response.	High	33628636
	<i>MTOR</i> disorder causes lower testosterone levels.	High	32026564
	Accumulation of <i>BAX</i> increased the release of testosterone in cultured granulosa cells.	High	31344364
	<i>PPARG</i> was involved in several estrogen metabolism pathways.	Moderate	36932403
KE1 to KE2	The gonadotropin receptor complex promotes testosterone production.	Moderate	1646778
	Blocking the classical testosterone-signaling pathway to exert antagonistic effects on <i>AR</i> receptors.	High	16169144
	Activation of the testosterone-signaling pathway mediated anti-androgenic secretion.	High	30974244
	Promotes the responsiveness of testicular-like organs to hormones and increases sensitivity to reproductive toxicants.	Moderate	36219953
KE2 to KE3	Disrupting steroid hormone-related signaling pathways to block steroid hormone secretion.	High	35990263
	Hormone secretion affects ovarian development.	High	23279460
	Feline gonads exhibit tissue-specific alternative splicing of estrogen receptors.	Moderate	20963760
	Antagonizing androgen receptors or inhibiting steroid hormone synthesis inhibits the normal development of the male reproductive system.	High	23525324
	Affected the development of the reproductive system of ovarian-intact experimental rats by regulating hormones and estrogen receptors.	High	21722617
KE3 to AO	Delayed seasonal gonad development in mature female cod reflecting reproductive toxicity.	High	20487044

Abbreviation: AOP=adverse outcome pathway; MIEs=molecular initiating events; KEs=key events; KERs=KE relationships.

## Vital Surveillances

## Relationships Between Meteorological Factors and Mongolian Gerbils and Its Flea Burdens — Xilingol League, Inner Mongolia Autonomous Region, China, 2012–2021

Ke Li<sup>1</sup>; Zhenxu Wang<sup>1</sup>; Xiaohui Wei<sup>1,2</sup>; Haoqiang Ji<sup>1,3</sup>; Meng Shang<sup>1,3</sup>; Nan Chang<sup>1,2</sup>; Zihao Wang<sup>1,2</sup>; Chenran Guo<sup>1,2</sup>; Lei Xu<sup>4</sup>; Ning Zhao<sup>1</sup>; Qiyong Liu<sup>1,2,3,#</sup>

### ABSTRACT

**Introduction:** Plague is a significant global infectious disease, its spread is linked to host and flea populations. Meteorological conditions can impact flea populations and host densities, hence influencing plague outbreaks. Investigating the connection between meteorological factors, flea populations, and rodent densities in Inner Mongolia's natural plague foci can aid in predicting and managing plague outbreaks.

**Methods:** Monthly data on flea index, rodent density, meteorological factors, and normalized difference vegetation index (NDVI) were collected for the study area. Generalized additive modeling (GAM) was used to analyze the non-linear and lag effects of meteorological factors on flea index and rodent density. Structural equation modeling (SEM) was employed to investigate the relationships among meteorological factors, NDVI, flea index, and rodent density.

**Results:** GAM analysis revealed that temperature, precipitation, relative humidity, and NDVI had significant linear, non-linear, and time-lagged impacts on the density of Mongolian gerbils and the flea index. SEM analysis indicated that meteorological factors could directly influence the density and flea index of Mongolian gerbils, or indirectly impact NDVI, subsequently influencing gerbil density and the flea index.

**Conclusions:** Meteorological factors primarily influence gerbil density and flea index indirectly by affecting NDVI and the relationship between flea index and gerbil density. This study offers additional support for the significance of meteorological factors and NDVI in influencing the vector-rodent system, offering valuable insights for predicting and managing plague outbreaks.

Plague, responsible for millions of deaths globally across three pandemics, is caused by the bacterium *Yersinia pestis* (*Y. pestis*). The Mongolian gerbil (*Meriones unguiculatus*) is the primary host of plague in the natural focus in the Inner Mongolian Plateau, carrying various pathogens, including *Y. pestis*. Recent plague cases in China have been mostly associated with Mongolian gerbils. Rodent and flea populations are crucial in plague outbreaks, and with climate change, vector-borne diseases like plague may have a more significant impact (1). Climate change influences vegetation, human activities, rodent populations, and fleas, affecting plague transmission dynamics. Meteorological factors impact rodent populations, flea numbers, and their growth (2–4). The trophic cascade hypothesis (5) explains the relationship among climate, vegetation, host, vector, and pathogen. Monitoring data from Mongolian gerbils in the Xilingol League, Inner Mongolia Autonomous Region, China were analyzed to study the effects of meteorological factors and vegetation on the vector-rodent system.

### METHODS

The monthly density and body flea index of Mongolian gerbils for this study were extracted from the Plague Control Management Information System of China CDC covering 10 counties in the Xilingol League from 2012 to 2021. Monthly cumulative precipitation, average temperature, and average relative humidity data were sourced from the China Meteorological Service Center (<https://data.cma.cn/>). The normalized difference vegetation index (NDVI) was used to evaluate vegetation conditions, offering insights into food availability and survival conditions for Mongolian gerbils. Monthly NDVI data were obtained from the Moderate Resolution Imaging

Spectroradiometer (MODIS) dataset, available via EarthData (<https://search.earthdata.nasa.gov/search>). All data were analyzed monthly. To account for the delayed impact of meteorological factors on Mongolian gerbils and their fleas, a lag of 0–2 months was applied to the meteorological data and NDVI in this study.

Generalized additive modeling (GAM) and structural equation modeling (SEM) were utilized to assess the impact of meteorological factors on the density and body flea index of Mongolian gerbils. In SEM, theoretical assumptions guided the exploration of direct and indirect causal relationships between variables. Initially, GAM was employed to develop two models incorporating Mongolian gerbil density and body flea index as response variables, alongside meteorological data lagged from 0–2 months and NDVI as explanatory variables. Model selection criteria prioritized maximizing Deviance explained and minimizing generalized cross-validation (GCV), favoring models with a lower GCV and a higher Deviance explained. Subsequently, SEM was employed, focusing on path analysis due to the absence of latent variables in the study. Monthly models were created using climate, rodent, flea, and NDVI data. Thirty-six time-lagged SEM combinations were evaluated to assess the delayed effects of meteorological factors and NDVI on rodent density and flea parasitism. The analysis was conducted using the “mgcv” package in R (version 4.2.2, R Core Team, Vienna, Austria) for GAM, and with AMOS (version 28.0, IBM Corporation, Armonk, NY, USA) for SEM.

## RESULTS

The table presented the densities, flea index, meteorological factors, and NDVI of Mongolian gerbils in the Xilingol League from 2012 to 2021. Over this period, 23,396 Mongolian gerbils were captured, resulting in 17,809 fleas, of which 6,521 were found on rodents, indicating a flea rate of 27.87% and a flea index of 0.76. The research revealed a negative linear correlation between gerbil density and the flea index. Moreover, meteorological factors and NDVI demonstrated significant effects on the gerbil density/flea index relationship, showing non-linear patterns and lag effects. The impact of meteorological factors on this relationship was influenced by NDVI and the reciprocal flea index/gerbil density.

The GAM analysis using rodent density as the response variable showed a negative linear relationship with the flea index ( $F=5.155$ ,  $P<0.05$ ; Figure 1A).

Rodent densities exhibited a cyclic pattern with peaks in 2014 and 2019 ( $F=5.391$ ,  $P<0.001$ ; Figure 1B). Additionally, a negative linear correlation was observed between rodent density and NDVI, possibly due to Mongolian gerbils' preference for desert grasslands with sparse vegetation ( $F=9.378$ ,  $P<0.01$ ; Figure 1C). Furthermore, rodent densities were positively correlated with temperature with a 2-month lag ( $F=5.143$ ,  $P<0.05$ ; Figure 1D), with precipitation in a linear fashion ( $F=4.895$ ,  $P<0.05$ ; Figure 1E), and with relative humidity in a nonlinear manner ( $F=3.222$ ,  $P<0.05$ ; Figure 1F). The GAM analysis using the flea index as the response variable revealed a negative linear correlation between body flea index in Mongolian gerbils and rodent density ( $F=5.759$ ,  $P<0.05$ ; Figure 2A) and NDVI ( $F=13.342$ ,  $P<0.001$ ; Figure 2C). The flea index decreased over time ( $F=7.145$ ,  $P<0.001$ ; Figure 2B) and was positively correlated with average temperature with a one-month lag ( $F=8.357$ ,  $P<0.01$ ; Figure 2D). Moreover, a nonlinear correlation was observed between the flea index and precipitation ( $F=2.864$ ,  $P<0.05$ ; Figure 2E) and average relative humidity with a one-month lag ( $F=3.773$ ,  $P<0.01$ ; Figure 2F).

The influence of meteorological factors on gerbil density occurs primarily through two indirect pathways (Figure 3A): meteorological factors (positive) → vegetation (negative) → rodent, and meteorological factors (positive) → vegetation (negative) → flea (negative) → rodent. These indirect pathways are well-supported by numerous models, whereas the direct pathway from meteorological factors to rodent density, meteorological factors → rodents, is less supported. This indicates that meteorological factors impact rodent density predominantly via NDVI and the flea index. Furthermore, in the SEM (Figure 3B) with the flea index as the final variable, the most supported model was meteorological factors (positive) → vegetation (negative) → flea, indicating that the influence of meteorological factors on the flea index is primarily mediated by NDVI.

## CONCLUSIONS

GAM and SEM were employed to examine the intricate relationships between biotic and abiotic factors in natural plague foci. A decade of surveillance data from 10 counties in the Xilingol League was utilized for the analysis. The findings highlight the influence of meteorological conditions on gerbil density and flea index, mediated by NDVI and the

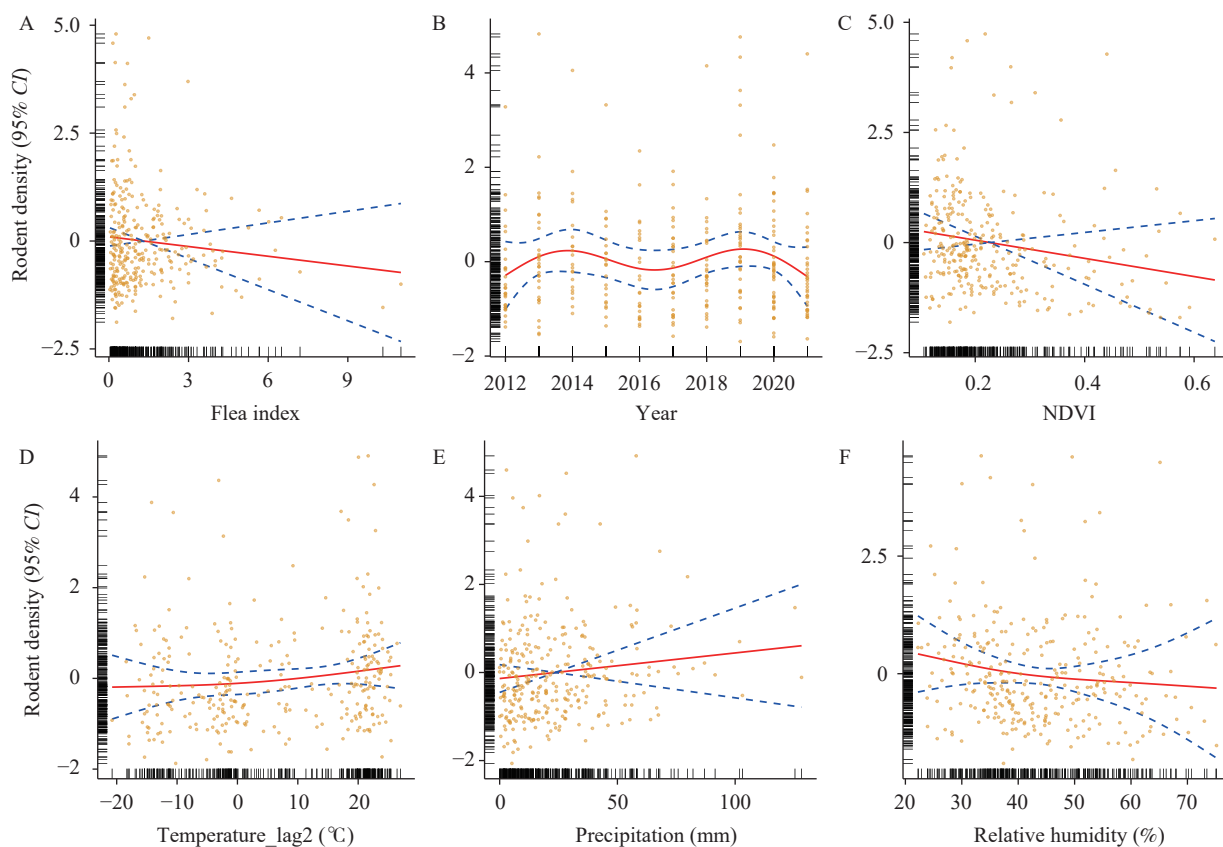


FIGURE 1. Analysis of factors influencing the density of Mongolian gerbils in Xilingol League from 2012 to 2021 using generalized additive modeling. (A) The correlation between flea index and rodent density; (B) The association between time trend (year) and rodent density; (C) The link between NDVI and rodent density; (D) The connection between monthly average temperature with a 2-month lag and rodent density; (E) The correlation between monthly cumulative precipitation and rodent density; (F) The relationship between monthly average relative humidity and rodent density. Abbreviation: NDVI=normalized difference vegetation index; CI=confidence interval.

reciprocal impact of flea index on gerbil density.

A negative correlation was observed between gerbil density and their body flea index, aligning with similar patterns found in Utah prairie dogs (6). The higher flea infestation likely impacted the survival and reproduction of gerbils by affecting immunity, behavior, and reproduction, ultimately contributing to decreased gerbil populations. Research on North American red squirrels revealed that flea-infected females gave birth to offspring with lower body weight and survival rates (7), while studies on voles demonstrated that flea-infected voles had notably reduced average lifespans (8). Furthermore, as fleas serve as vectors for various pathogens, elevated flea indices facilitate pathogen transmission among gerbils, consequently lowering gerbil densities.

Temperature was found to have a positive correlation with gerbil density and flea index, aligning with a previous study on *Rattus norvegicus* in Ningbo (2). Temperature affects gerbil density through factors

like metabolism, reproduction, activity, and food availability. Low temperatures can hinder oocyte development in female gerbils and lead to testicular atrophy in males, reducing sperm production and hindering gerbil reproduction. Flea larvae and pupae are sensitive to temperature, as higher temperatures can speed up their development and shorten the reproductive cycle, ultimately increasing flea populations (9). Consequently, warmer temperatures contribute to higher flea parasitism rates in gerbils due to increased flea numbers.

The study found a positive relationship between precipitation, gerbil density, and the flea index. Research in Hebei Province indicated a direct link between flea prevalence and precipitation (3). However, studies in Inner Mongolia demonstrated a curvilinear association among gerbil density, flea index, and precipitation (4). The increased precipitation and relative humidity likely created ideal conditions for flea survival and reproduction in gerbil burrows (6).

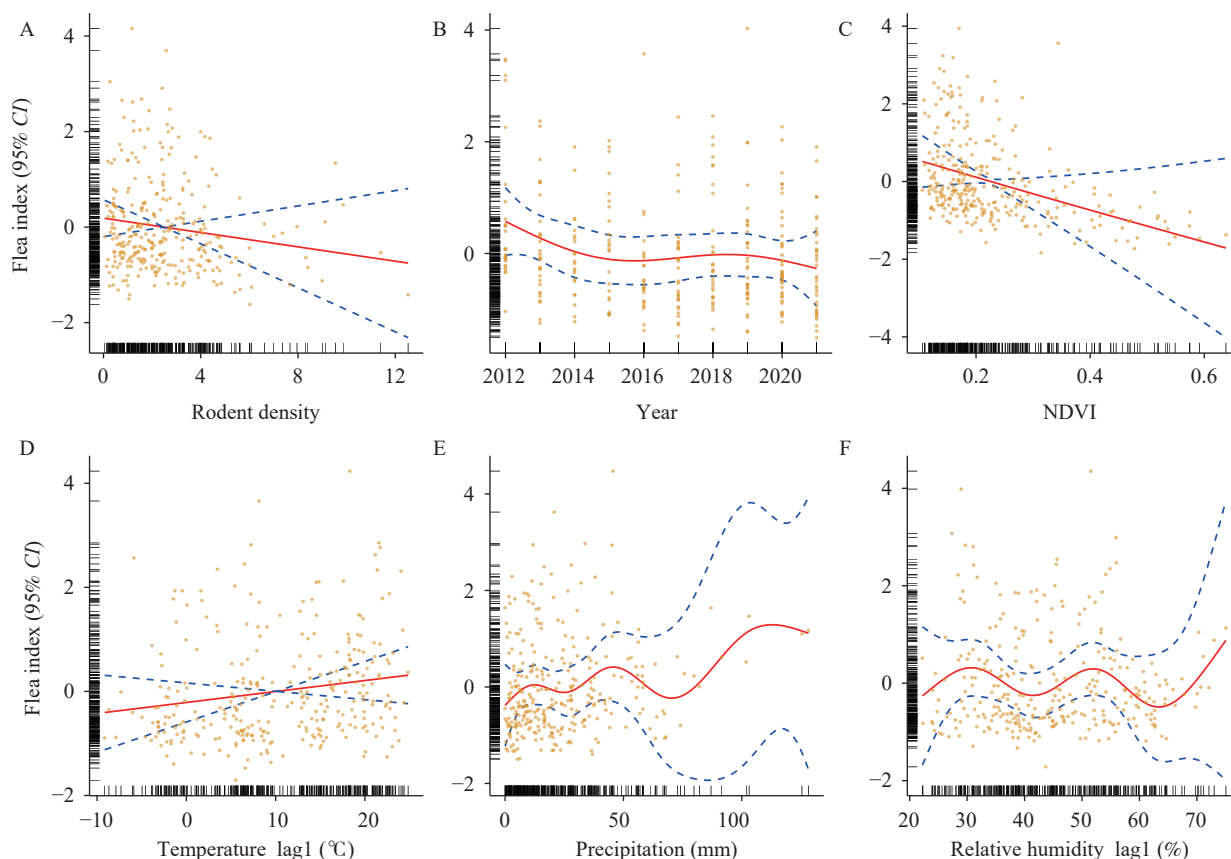


FIGURE 2. Analysis of factors influencing the flea index of Mongolian gerbils in Xilingol League from 2012 to 2021 using generalized additive modeling. (A) The correlation between rodent density and the flea index; (B) The association between flea time trend (year) and the flea index; (C) The link between flea NDVI and the flea index; (D) The connection between monthly average temperature with a 1-month lag and the flea index; (E) The correlation between monthly cumulative precipitation and the flea index; (F) The relationship between monthly average relative humidity with a 1-month lag and the flea index.

Abbreviation: NDVI=normalized difference vegetation index; CI=confidence interval.

Adequate precipitation boosts vegetation growth, providing more food for gerbils. Relative humidity displayed a non-linear negative correlation with gerbil density and an erratic upward trend with the flea index, possibly due to the arid environment of desert grasslands preferred by gerbils. Conversely, relative humidity can impact flea reproduction and abundance by influencing the female ratio, developmental rate, and life cycle of the fleas (10–11).

A multitude of studies have established a significant link between the NDVI and the distribution, abundance, and density of small mammal populations (12–13). Contrary to the trophic cascade hypothesis, our research in the Xilingol League has shown that as temperature, precipitation, and relative humidity increase, NDVI values rise, but the density of Mongolian gerbil populations and the flea index decrease, a finding that echoes those of Xu et al. (14). This inverse trend may be due to gerbils' preference for

desert grassland ecosystems, where the NDVI reflects vegetation cover rather than the actual availability of food resources. Moreover, host habitat significantly shapes the composition and prevalence of fleas; variations in vegetation density and structure can alter flea populations and their movements. Furthermore, the diversity of flea parasites found on rodent hosts changes with the ecological terrain (15). Within our study, a negative correlation was observed between the gerbil flea index and NDVI, suggesting that less dense vegetation may be more conducive to host survival, and thus, the relationship between the flea index and NDVI correlates inversely with host distribution patterns.

This study is subject to some limitations. First, the lack of continuous data on Mongolian gerbil densities and flea index may have impacted the accuracy of model predictions. Second, the analysis focused solely on the ecological aspects of the vector-rodent system,

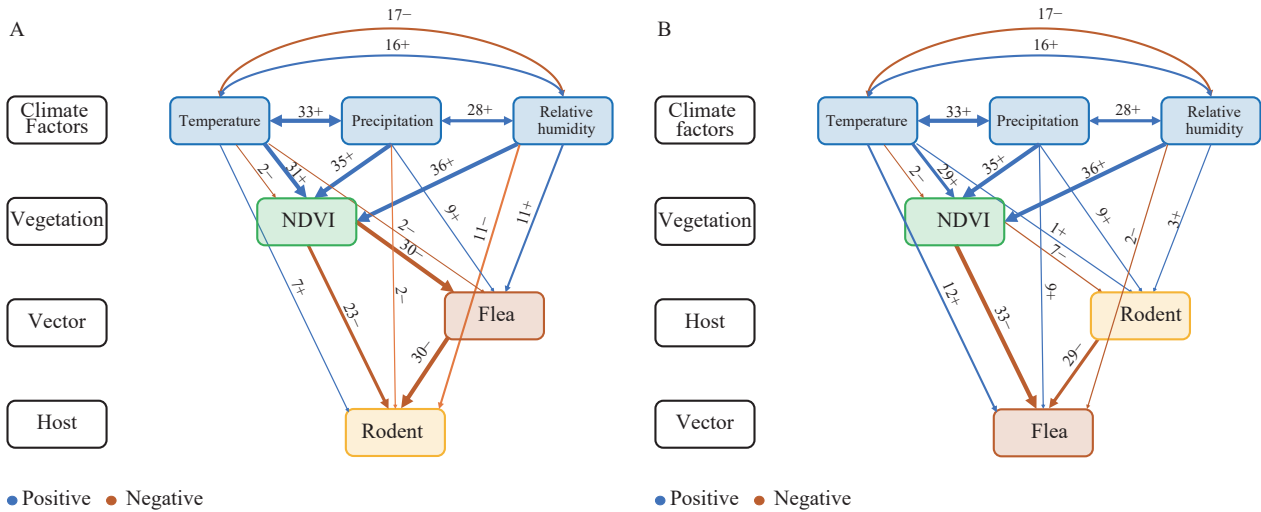


FIGURE 3. The results of SEM for meteorological factors and vegetation on the vector-rodent system in Xilingol League, 2012–2021. (A) SEM with Mongolian gerbils' density as the final variable; (B) SEM with Mongolian gerbils' flea index as the final variable.

Note: Thirty-six monthly model combinations were developed by considering time-lagged relationships between the current month and the two preceding months. The width and quantity of lines in the diagram reflect the statistical significance ( $P < 0.05$ ) and level of support for each pathway. Positive correlations are indicated by blue lines marked with a “+,” while negative correlations are represented by orange lines marked with a “-”. The arrows show the direction of influence within the model.

Abbreviation: SEM=structural equation modeling; NDVI=normalized difference vegetation index.

TABLE 1. Monthly summary statistics for Mongolian gerbil density, flea index, and meteorological factors in Xilingol League, 2012–2021.

Variable	Mean	Standard deviation	Minimum	P25	P50	P75	Maximum
Rodent density (gerbils/hectare)	2.49	1.98	0.05	1.05	2.08	3.33	12.53
Flea index	1.31	1.50	0.04	0.33	0.77	1.79	11.00
Monthly average temperature (°C)	11.77	6.15	-8.01	6.78	12.97	15.81	22.81
Average temperature with 1-month lag (°C)	10.12	8.50	-9.15	3.73	9.42	17.98	24.85
Average temperature with 2-month lag (°C)	6.16	14.01	-20.76	-4.58	5.43	20.93	27.00
Monthly cumulative precipitation (mm)	23.62	21.69	0.00	7.50	16.90	33.80	128.20
Cumulative precipitation with 1-month lag (mm)	23.64	26.32	0.00	4.60	14.20	35.30	168.60
Cumulative precipitation with 2-month lag (mm)	26.22	37.38	0.00	2.60	9.20	40.30	271.20
Monthly average relative humidity (%)	43.37	11.49	22.23	34.97	41.42	51.60	75.17
Monthly average relative humidity with 1-month lag (%)	44.68	11.86	22.23	35.63	43.50	53.77	75.05
Monthly average relative humidity with 2-month lag (%)	49.95	11.75	22.30	41.05	51.58	58.55	75.52
NDVI	0.23	0.11	0.11	0.16	0.19	0.26	0.64
NDVI with 1-month lag	0.23	0.13	0.10	0.15	0.18	0.26	0.66
NDVI with 2-month lag	0.21	0.14	-0.01	0.13	0.16	0.25	0.63

Abbreviation: NDVI=normalized difference vegetation index.

without consideration of pathogens or plague cases. Consequently, drawing direct conclusions about pathogen transmission dynamics or mechanisms of plague outbreaks is not feasible.

In conclusion, meteorological factors influence gerbil density and flea index indirectly through their

impact on NDVI and the interaction between fleas and gerbils. This suggests a complex mediating mechanism in the ecosystem, indicating the regulatory roles of NDVI and flea-gerbil interactions. Favorable temperature and precipitation conditions enhance Mongolian gerbil survival, leading to local rodent

infestations and increasing the risk of plague outbreaks. Human activities like overgrazing contribute to grassland desertification, creating suitable habitats for Mongolian gerbils and further elevating the plague risk. Regular monitoring of meteorological conditions (temperature, humidity, precipitation) and NDVI is crucial to comprehend gerbil ecological dynamics and flea vectors. Local CDC departments should intensify rodent surveillance and control during warm temperatures, increased precipitation, and low NDVI. Implementing grazing reduction measures and grassland restoration can reduce gerbil plague risk. Developing predictive systems for gerbils and plague outbreaks should integrate ecological, meteorological, and human activity factors for effective management. Such a holistic approach can safeguard human and ecosystem health.

**Conflicts of interest:** No conflicts of interest.

**Funding:** Supported by the Key Program of National Natural Science Foundation of China (grant number 32090023).

**doi:** 10.46234/ccdcw2024.107

# Corresponding author: Qiyong Liu, liuqiyong@icdc.cn.

<sup>1</sup> National Key Laboratory of Intelligent Tracking and Forecasting for Infectious Diseases, National Institute for Communicable Disease Control and Prevention, Chinese Center for Disease Control and Prevention, Beijing, China; <sup>2</sup> School of Public Health, Nanjing Medical University, Nanjing City, Jiangsu Province, China; <sup>3</sup> Cheeloo College of Medicine, Shandong University, School of Public Health, Jinan City, Shandong Province, China; <sup>4</sup> Vanke School of Public Health, Tsinghua University, Beijing, China.

Submitted: January 08, 2024; Accepted: March 11, 2024

## REFERENCES

- Liu QY. The impacts of climate change on vector-borne diseases. *Chin J Hyg Insect Equip* 2013;19:7,12. (In Chinese). [https://kns.cnki.net/kcms2/article/abstract?v=2dRWw02s3kwz3a0B1a2\\_5cdtoMXjXY8GDe99lLtE19nzfScOkcp1EwmSr-k6Rpl6v\\_liw00wWcBQp6MX9K-yCFRTQEmYq1kRiYqeqAVU:Unv0SaRefKNdebMG SqWiOSp9jcrDdp8gog=&uniplatform=NZKPT&language=CHS](https://kns.cnki.net/kcms2/article/abstract?v=2dRWw02s3kwz3a0B1a2_5cdtoMXjXY8GDe99lLtE19nzfScOkcp1EwmSr-k6Rpl6v_liw00wWcBQp6MX9K-yCFRTQEmYq1kRiYqeqAVU:Unv0SaRefKNdebMG SqWiOSp9jcrDdp8gog=&uniplatform=NZKPT&language=CHS)
- Wang JN, Lao JH, Hou J, Guo S, Wu YY, Ma X, et al. Effect of meteorological factors on rodent density. *China Prev Med J* 2018;30(9):870 – 3,878. <https://doi.org/10.19485/j.cnki.issn2096-5087.2018.09.002>.
- Niu YF, Liu HZ, Zhang YH, Kang DM, Liu G, Wang HF, et al. An analysis of the relationship between rodent fleas and meteorological factors in *Meriones unguiculatus* plague foci in Hebei province, China. *Chin J Vector Biol Control* 2021;32(1):41-4. <http://dx.doi.org/10.11853/j.issn.1003.8280.2021.01.008>. (In Chinese).
- Xu L, Li GC, Si XY, Fang XY, Liu QY. Nonlinear effects of climate driven plague in *Meriones unguiculatus* natural foci in Inner Mongolia. *Chin J Vector Biol Control* 2016;27(4):321 – 5. <https://doi.org/10.11853/j.issn.1003.8280.2016.04.002>.
- Parmenter RR, Yadav EP, Parmenter CA, Ettestad P, Gage KL. Incidence of plague associated with increased winter-spring precipitation in New Mexico. *Am J Trop Med Hyg* 1999;61(5):814 – 21. <https://doi.org/10.4269/ajtmh.1999.61.814>.
- Eads DA, Abbott RC, Biggins DE, Rocke TE. Flea parasitism and host survival in a plague-relevant system: theoretical and conservation implications. *J Wildl Dis* 2020;56(2):378. <https://doi.org/10.7589/2019-08-2019>.
- Patterson JEH, Neuhaus P, Kutz SJ, Ruckstuhl KE. Parasite removal improves reproductive success of female North American red squirrels (*Tamiasciurus hudsonicus*). *PLoS One* 2013;8(2):e55779. <https://doi.org/10.1371/journal.pone.0055779>.
- Devevey G, Christe P. Flea infestation reduces the life span of the common vole. *Parasitology* 2009;136(11):1351 – 5. <https://doi.org/10.1017/S0031182009990746>.
- Iurgenson IA, Makesimov VN. Effect of air temperature and relative humidity on the preimaginal development of *Ctenophthalmus teres* fleas (Siphonaptera). *Parazitologija* 1981;15(1):38-46. <https://pubmed.ncbi.nlm.nih.gov/7465246/>. (In Russian).
- Kreppel KS, Telfer S, Rajerison M, Morse A, Baylis M. Effect of temperature and relative humidity on the development times and survival of *Synopsyllus fonquerniei* and *Xenopsylla cheopis*, the flea vectors of plague in Madagascar. *Parasit Vectors* 2016;9:82. <https://doi.org/10.1186/s13071-016-1366-z>.
- Krasnov BR, Khokhlova IS, Fielden LJ, Burdelova NV. Effect of air temperature and humidity on the survival of pre-imaginal stages of two flea species (Siphonaptera: Pulicidae). *J Med Entomol* 2001;38(5):629 – 37. <https://doi.org/10.1603/0022-2585-38.5.629>.
- Ramírez-Bautista A, Williams JN. The importance of productivity and seasonality for structuring small rodent diversity across a tropical elevation gradient. *Oecologia* 2019;190(2):275 – 86. <https://doi.org/10.1007/s00442-018-4287-z>.
- Xiao H, Liu HN, Gao LD, Huang CR, Li Z, Lin XL, et al. Investigating the effects of food available and climatic variables on the animal host density of hemorrhagic fever with renal syndrome in Changsha, China. *PLoS One* 2013;8(4):e61536. <http://dx.doi.org/10.1371/journal.pone.0061536>.
- Xu L, Schmid BV, Liu J, Si XY, Stenseth NC, Zhang ZB. The trophic responses of two different rodent-vector-plague systems to climate change. *Proc Biol Sci* 2015;282(1800):20141846. <http://dx.doi.org/10.1098/rspb.2014.1846>.
- Yang K, Zhang JP, Wu ML, Bai X. Effects of habitat on flea community and life history. *Chin J Vector Biol Control* 2011;22(1):86-8. <http://www.bmsw.net.cn/CN/Y2011/V22/I1/86>. (In Chinese).

## SUPPLEMENTARY MATERIAL

SUPPLEMENTARY TABLE S1. Model selection process for analyzing factors affecting Mongolian gerbils density using generalized additive modeling.

Model	Model type	Formula	Significant factors	R-sq.(adj)	Deviance explained (%)	GCV
1	Year	$Y_{i,t}=f_1(\text{year}_{i,t})+\alpha_{i,t}$	year	0.0899	11.90	1.2908
2	Flea	$Y_{i,t}=f_1(\text{flea}_{i,t})+\alpha_{i,t}$	NAN	0.0024	1.06	1.3985
3		$Y_{i,t}=f_1(\text{NDVI}_{i,t})+\alpha_{i,t}$	NDVI	0.0340	4.45	1.3462
3.lag1	NDVI	$Y_{i,t}=f_1(\text{NDVI}_{i,t-1})+\alpha_{i,t}$	NAN	0.0088	1.47	1.3883
3.lag2		$Y_{i,t}=f_1(\text{NDVI}_{i,t-2})+\alpha_{i,t}$	NAN	0.0050	1.40	1.3986
4		$Y_{i,t}=f_1(\text{Tmp}_{i,t})+\alpha_{i,t}$	NAN	0.0037	1.10	1.4013
4.lag1	Tmp	$Y_{i,t}=f_1(\text{Tmp}_{i,t-1})+\alpha_{i,t}$	NAN	0.0342	6.56	1.3729
4.lag2		$Y_{i,t}=f_1(\text{Tmp}_{i,t-2})+\alpha_{i,t}$	NAN	-0.0034	0.00	1.4089
5		$Y_{i,t}=f_1(\text{Pre}_{i,t})+\alpha_{i,t}$	NAN	0.0007	0.46	1.4025
5.lag1	Pre	$Y_{i,t}=f_1(\text{Pre}_{i,t-1})+\alpha_{i,t}$	NAN	0.0055	1.01	1.3946
5.lag2		$Y_{i,t}=f_1(\text{Pre}_{i,t-2})+\alpha_{i,t}$	NAN	0.0009	0.54	1.4014
6		$Y_{i,t}=f_1(\text{Rhu}_{i,t})+\alpha_{i,t}$	Rhu	0.0346	5.38	1.3596
6.lag1	Rhu	$Y_{i,t}=f_1(\text{Rhu}_{i,t-1})+\alpha_{i,t}$	Rhu	0.0329	4.10	1.3512
6.lag2		$Y_{i,t}=f_1(\text{Rhu}_{i,t-2})+\alpha_{i,t}$	NAN	0.0176	3.38	1.3881
7		$Y_{i,t}=f_1(\text{flea}_{i,t})+f_2(\text{Tmp}_{i,t})+\alpha_{i,t}$	NAN	0.0060	2.03	1.4010
7.lag1	Flea+Tmp	$Y_{i,t}=f_1(\text{flea}_{i,t-1})+f_2(\text{Tmp}_{i,t-1})+\alpha_{i,t}$	NAN	0.0375	7.28	1.3730
7.lag2		$Y_{i,t}=f_1(\text{flea}_{i,t-2})+f_2(\text{Tmp}_{i,t-2})+\alpha_{i,t}$	NAN	-0.0014	0.91	1.4090
8		$Y_{i,t}=f_1(\text{flea}_{i,t})+f_2(\text{Pre}_{i,t})+\alpha_{i,t}$	NAN	0.0023	1.26	1.4028
8.lag1	Flea+Pre	$Y_{i,t}=f_1(\text{flea}_{i,t-1})+f_2(\text{Pre}_{i,t-1})+\alpha_{i,t}$	NAN	0.0092	2.03	1.3916
8.lag2		$Y_{i,t}=f_1(\text{flea}_{i,t-2})+f_2(\text{Pre}_{i,t-2})+\alpha_{i,t}$	NAN	0.0036	1.43	1.4001
9		$Y_{i,t}=f_1(\text{flea}_{i,t})+f_2(\text{Rhu}_{i,t})+\alpha_{i,t}$	Rhu	0.0472	7.00	1.3486
9.lag1	Flea+Rhu	$Y_{i,t}=f_1(\text{flea}_{i,t-1})+f_2(\text{Rhu}_{i,t-1})+\alpha_{i,t}$	Rhu	0.0435	5.60	1.3399
9.lag2		$Y_{i,t}=f_1(\text{flea}_{i,t-2})+f_2(\text{Rhu}_{i,t-2})+\alpha_{i,t}$	NAN	0.0216	4.33	1.3844
10		$Y_{i,t}=f_1(\text{flea}_{i,t})+f_2(\text{Tmp}_{i,t})+f_3(\text{year}_{i,t})+\alpha_{i,t}$	Year	0.0938	13.20	1.2977
10.lag1	Flea+Tmp+ year	$Y_{i,t}=f_1(\text{flea}_{i,t-1})+f_2(\text{Tmp}_{i,t-1})+f_3(\text{year}_{i,t})+\alpha_{i,t}$	Year	0.1010	15.50	1.2968
10.lag2		$Y_{i,t}=f_1(\text{flea}_{i,t-2})+f_2(\text{Tmp}_{i,t-2})+f_3(\text{year}_{i,t})+\alpha_{i,t}$	Year	0.0863	12.20	1.3031
11		$Y_{i,t}=f_1(\text{flea}_{i,t})+f_2(\text{Pre}_{i,t})+f_3(\text{year}_{i,t})+\alpha_{i,t}$	Year	0.0874	12.00	1.3008
11.lag1	Flea+Pre+ year	$Y_{i,t}=f_1(\text{flea}_{i,t-1})+f_2(\text{Pre}_{i,t-1})+f_3(\text{year}_{i,t})+\alpha_{i,t}$	Year	0.0882	12.30	1.3004
11.lag2		$Y_{i,t}=f_1(\text{flea}_{i,t-2})+f_2(\text{Pre}_{i,t-2})+f_3(\text{year}_{i,t})+\alpha_{i,t}$	Year	0.3230	40.70	1.0058
12		$Y_{i,t}=f_1(\text{flea}_{i,t})+f_2(\text{Rhu}_{i,t})+f_3(\text{year}_{i,t})+\alpha_{i,t}$	Rhu, year	0.1260	17.90	1.2667
12.lag1	Flea+Rhu+ year	$Y_{i,t}=f_1(\text{flea}_{i,t-1})+f_2(\text{Rhu}_{i,t-1})+f_3(\text{year}_{i,t})+\alpha_{i,t}$	Rhu, year	0.1180	15.00	1.2559
12.lag2		$Y_{i,t}=f_1(\text{flea}_{i,t-2})+f_2(\text{Rhu}_{i,t-2})+f_3(\text{year}_{i,t})+\alpha_{i,t}$	Year	0.0891	12.50	1.2960
13		$Y_{i,t}=f_1(\text{flea}_{i,t})+f_2(\text{NDVI}_{i,t})+f_3(\text{year}_{i,t})+\alpha_{i,t}$	NDVI, year	0.1200	15.70	1.2486
13.lag1	Flea+NDVI+ year	$Y_{i,t}=f_1(\text{flea}_{i,t-1})+f_2(\text{NDVI}_{i,t-1})+f_3(\text{year}_{i,t})+\alpha_{i,t}$	NDVI, year	0.1310	18.10	1.2708
13.lag2		$Y_{i,t}=f_1(\text{flea}_{i,t-2})+f_2(\text{NDVI}_{i,t-2})+f_3(\text{year}_{i,t})+\alpha_{i,t}$	year	0.0897	12.40	1.2996
14	Flea+Tmp+Pre+ Rhu+NDVI+year	$Y_{i,t}=f_1(\text{flea}_{i,t})+f_2(\text{year}_{i,t})+f_3(\text{Tmp}_{i,t-2})+f_4(\text{Pre}_{i,t})+f_5(\text{Rhu}_{i,t})+f_6(\text{NDVI}_{i,t})+\alpha_{i,t}$	Flea, year, Tmp, Rhu, pre, NDVI	0.1350	18.80	1.2216

Note: Models were selected using the coefficient of determination (R-sq.) and GCV. Models with larger R-sq. and lower GCV values had higher out-of-sample predictive power. Therefore, Model 14 is the final model with the highest R-sq. value and the lowest GCV value.

Abbreviation: GCV=Generalized cross-validation.

SUPPLEMENTARY TABLE S2. Results of generalized additive modeling to analyze factors affecting Mongolian gerbils density.

<b>Factors</b>	<b>edf</b>	<b>F</b>	<b>P value</b>
s(flea)	1	5.155	0.0239*
s(year)	3.922	5.391	0.0003***
s(NDVI)	1	9.378	0.0024**
s(pre)	1	4.895	0.0277*
s(RHU_Avg)	1.839	3.222	0.0461*
s(TEM_Avg_2)	1.561	5.143	0.0173*

\*  $P < 0.05$ .\*\*  $P < 0.01$ .\*\*\*  $P < 0.001$ .

SUPPLEMENTARY TABLE S3. Model selection process for analyzing factors affecting Mongolian gerbils flea index using generalized additive modeling.

Model	Model type	Formula	Significant factors	R-sq.(adj)	Deviance explained (%)	GCV
1	Year	$Y_{i,t}=f_1(\text{year}_{i,t})+\alpha_{i,t}$	Year	0.0507	7.00	1.2118
2	Rodent	$Y_{i,t}=f_1(\text{rodent}_{i,t})+\alpha_{i,t}$	NAN	0.0117	3.26	1.2607
3		$Y_{i,t}=f_1(\text{NDVI}_{i,t})+\alpha_{i,t}$	NDVI	0.0425	6.81	1.1967
3.lag1	NDVI	$Y_{i,t}=f_1(\text{NDVI}_{i,t-1})+\alpha_{i,t}$	NDVI	0.0412	8.32	1.208
3.lag2		$Y_{i,t}=f_1(\text{NDVI}_{i,t-2})+\alpha_{i,t}$	NDVI	0.0438	9.51	1.2064
4		$Y_{i,t}=f_1(\text{Tmp}_{i,t})+\alpha_{i,t}$	NAN	0.00328	0.95	1.2719
4.lag1	Tmp	$Y_{i,t}=f_1(\text{Tmp}_{i,t-1})+\alpha_{i,t}$	NAN	-0.00334	0.00	1.2841
4.lag2		$Y_{i,t}=f_1(\text{Tmp}_{i,t-2})+\alpha_{i,t}$	NAN	0.0013	0.64	1.276
5		$Y_{i,t}=f_1(\text{Pre}_{i,t})+\alpha_{i,t}$	NAN	0.00545	3.21	1.2791
5.lag1	Pre	$Y_{i,t}=f_1(\text{Pre}_{i,t-1})+\alpha_{i,t}$	Pre	0.0147	2.78	1.2485
5.lag2		$Y_{i,t}=f_1(\text{Pre}_{i,t-2})+\alpha_{i,t}$	NAN	0.00608	1.49	1.265
6		$Y_{i,t}=f_1(\text{Rhu}_{i,t})+\alpha_{i,t}$	Rhu	0.0392	7.25	1.2244
6.lag1	Rhu	$Y_{i,t}=f_1(\text{Rhu}_{i,t-1})+\alpha_{i,t}$	Rhu	0.084	13.60	1.153
6.lag2		$Y_{i,t}=f_1(\text{Rhu}_{i,t-2})+\alpha_{i,t}$	Rhu	0.0105	1.86	1.2603
7		$Y_{i,t}=f_1(\text{rodent}_{i,t})+f_2(\text{Tmp}_{i,t})+\alpha_{i,t}$	NAN	0.0195	5.68	1.2547
7.lag1	Rodent+Tmp	$Y_{i,t}=f_1(\text{rodent}_{i,t-1})+f_2(\text{Tmp}_{i,t-1})+\alpha_{i,t}$	NAN	0.00825	3.28	1.2691
7.lag2		$Y_{i,t}=f_1(\text{rodent}_{i,t-2})+f_2(\text{Tmp}_{i,t-2})+\alpha_{i,t}$	NAN	0.013	4.08	1.2592
8		$Y_{i,t}=f_1(\text{rodent}_{i,t})+f_2(\text{Pre}_{i,t})+\alpha_{i,t}$	NAN	0.0165	6.07	1.2656
8.lag1	Rodent+Pre	$Y_{i,t}=f_1(\text{rodent}_{i,t-1})+f_2(\text{Pre}_{i,t-1})+\alpha_{i,t}$	Pre	0.0277	7.93	1.2495
8.lag2		$Y_{i,t}=f_1(\text{rodent}_{i,t-2})+f_2(\text{Pre}_{i,t-2})+\alpha_{i,t}$	NAN	0.0208	5.18	1.2461
9		$Y_{i,t}=f_1(\text{rodent}_{i,t})+f_2(\text{Rhu}_{i,t})+\alpha_{i,t}$	Rhu	0.0595	11.50	1.1972
9.lag1	Rodent+Rhu	$Y_{i,t}=f_1(\text{rodent}_{i,t-1})+f_2(\text{Rhu}_{i,t-1})+\alpha_{i,t}$	Rodent, Rhu	0.122	19.30	1.1133
9.lag2		$Y_{i,t}=f_1(\text{rodent}_{i,t-2})+f_2(\text{Rhu}_{i,t-2})+\alpha_{i,t}$	Rhu	0.0251	5.03	1.2462
10		$Y_{i,t}=f_1(\text{rodent}_{i,t})+f_2(\text{Tmp}_{i,t})+f_3(\text{year}_{i,t})+\alpha_{i,t}$	Year	0.0731	13.40	1.1877
10.lag1	Rodent+Tmp+year	$Y_{i,t}=f_1(\text{rodent}_{i,t-1})+f_2(\text{Tmp}_{i,t-1})+f_3(\text{year}_{i,t})+\alpha_{i,t}$	Year	0.0594	10.70	1.2065
10.lag2		$Y_{i,t}=f_1(\text{rodent}_{i,t-2})+f_2(\text{Tmp}_{i,t-2})+f_3(\text{year}_{i,t})+\alpha_{i,t}$	Year	0.0818	15.20	1.1888
11		$Y_{i,t}=f_1(\text{rodent}_{i,t})+f_2(\text{Pre}_{i,t})+f_3(\text{year}_{i,t})+\alpha_{i,t}$	Year	0.0971	15.60	1.1923
11.lag1	Rodent+Pre+year	$Y_{i,t}=f_1(\text{rodent}_{i,t-1})+f_2(\text{Pre}_{i,t-1})+f_3(\text{year}_{i,t})+\alpha_{i,t}$	Pre, year	0.084	13.60	1.1706
11.lag2		$Y_{i,t}=f_1(\text{rodent}_{i,t-2})+f_2(\text{Pre}_{i,t-2})+f_3(\text{year}_{i,t})+\alpha_{i,t}$	Pre, year	0.0726	12.40	1.1824
12		$Y_{i,t}=f_1(\text{rodent}_{i,t})+f_2(\text{Rhu}_{i,t})+f_3(\text{year}_{i,t})+\alpha_{i,t}$	Rhu, year	0.111	17.60	1.1542
12.lag1	Rodent+Rhu+year	$Y_{i,t}=f_1(\text{rodent}_{i,t-1})+f_2(\text{Rhu}_{i,t-1})+f_3(\text{year}_{i,t})+\alpha_{i,t}$	Rodent, Rhu, year	0.202	27.20	1.0458
12.lag2		$Y_{i,t}=f_1(\text{rodent}_{i,t-2})+f_2(\text{Rhu}_{i,t-2})+f_3(\text{year}_{i,t})+\alpha_{i,t}$	Rhu, year	0.0828	14.80	1.1692
13		$Y_{i,t}=f_1(\text{rodent}_{i,t})+f_2(\text{NDVI}_{i,t})+f_3(\text{year}_{i,t})+\alpha_{i,t}$	NDVI, year	0.112	17.00	1.1213
13.lag1	Rodent+NDVI+year	$Y_{i,t}=f_1(\text{rodent}_{i,t-1})+f_2(\text{NDVI}_{i,t-1})+f_3(\text{year}_{i,t})+\alpha_{i,t}$	NDVI, year	0.111	18.70	1.1267
13.lag2		$Y_{i,t}=f_1(\text{rodent}_{i,t-2})+f_2(\text{NDVI}_{i,t-2})+f_3(\text{year}_{i,t})+\alpha_{i,t}$	NDVI, year	0.114	19.60	1.1327
14	Rodent+Tmp+Pre+Rhu+NDVI+year	$Y_{i,t}=f_1(\text{rodent}_{i,t})+f_2(\text{year}_{i,t})+f_3(\text{Tmp}_{i,t-1})+f_3(\text{Pre}_{i,t})+f_3(\text{Rhu}_{i,t-1})+f_4(\text{NDVI}_{i,t})+\alpha_{i,t}$	Rodent, year, Tmp, Pre, Rhu, NDVI	0.23	29.00	1.014

Note: Models were selected using the coefficient of determination (R-sq.) and GCV. Models with larger R-sq. and lower GCV values had higher out-of-sample predictive power. Therefore, Model 14 is the final model with the highest R-sq. value and the lowest GCV value.

Abbreviation: GCV=Generalized cross-validation; NDVI= normalized difference vegetation index.

SUPPLEMENTARY TABLE S4. Results of generalized additive modeling to analyze factors affecting Mongolian gerbils flea index.

Factors	edf	F	P value
s(rodent,bs='cr')	1	5.759	0.0171*
s(year,bs='cr')	3.055	7.145	0.0000487***
s(NDVI,bs='cr')	1.061	13.342	0.0002***
s(pre,bs='cr')	5.659	2.864	0.0096*
s(RHU_Avg_1,bs='cr')	4.892	3.773	0.0036**
s(TEM_Avg_1,bs='cr')	1	8.357	0.0041**

\*  $P < 0.05$ .\*\*  $P < 0.01$ .\*\*\*  $P < 0.001$ .

SUPPLEMENTARY TABLE S5. SEM with Mongolian gerbils' density as the final variable. Red means statistically significant, black means not statistically significant, 0 current month, 1 previous month, 2 previous 2 months.

Time lag of RHU_Avg		Time lag of TEM_Avg		Time lag of NDVI		Time lag of flea		Time lag of rodent		Time lag of flea		Time lag of rodent		Time lag of flea		Time lag of rodent		Time lag of flea		Time lag of rodent		
pre	pre	pre	pre	pre	pre	pre	pre	pre	pre	pre	pre	pre	pre	pre	pre	pre	pre	pre	pre	pre	pre	
0	0	0	0	0	0	0	0	0	0	0	0	0	0	0	0	0	0	0	0	0	0	0
0	1	0	0	0	0	0	0	0	0	0	0	0	0	0	0	0	0	0	0	0	0	0
0	1	1	0	0	0	0	0	0	0	0	0	0	0	0	0	0	0	0	0	0	0	0
0	1	2	0	0	0	0	0	0	0	0	0	0	0	0	0	0	0	0	0	0	0	0
0	2	0	0	0	0	0	0	0	0	0	0	0	0	0	0	0	0	0	0	0	0	0
0	2	1	0	0	0	0	0	0	0	0	0	0	0	0	0	0	0	0	0	0	0	0
0	2	2	0	0	0	0	0	0	0	0	0	0	0	0	0	0	0	0	0	0	0	0
0	0	1	0	0	0	0	0	0	0	0	0	0	0	0	0	0	0	0	0	0	0	0
0	0	2	0	0	0	0	0	0	0	0	0	0	0	0	0	0	0	0	0	0	0	0
1	0	0	0	0	0	0	0	0	0	0	0	0	0	0	0	0	0	0	0	0	0	0
1	1	0	0	0	0	0	0	0	0	0	0	0	0	0	0	0	0	0	0	0	0	0
1	1	1	1	1	1	1	1	1	1	1	1	1	1	1	1	1	1	1	1	1	1	1
1	1	2	0	0	0	0	0	0	0	0	0	0	0	0	0	0	0	0	0	0	0	0
1	2	0	0	0	0	0	0	0	0	0	0	0	0	0	0	0	0	0	0	0	0	0
1	2	2	1	1	1	1	1	1	1	1	1	1	1	1	1	1	1	1	1	1	1	1
1	0	1	0	0	0	0	0	0	0	0	0	0	0	0	0	0	0	0	0	0	0	0
1	2	1	0	0	0	0	0	0	0	0	0	0	0	0	0	0	0	0	0	0	0	0
1	2	1	1	1	1	1	1	1	1	1	1	1	1	1	1	1	1	1	1	1	1	1
1	0	2	0	0	0	0	0	0	0	0	0	0	0	0	0	0	0	0	0	0	0	0
2	0	0	0	0	0	0	0	0	0	0	0	0	0	0	0	0	0	0	0	0	0	0
2	1	0	0	0	0	0	0	0	0	0	0	0	0	0	0	0	0	0	0	0	0	0
2	1	1	0	0	0	0	0	0	0	0	0	0	0	0	0	0	0	0	0	0	0	0
2	1	2	0	0	0	0	0	0	0	0	0	0	0	0	0	0	0	0	0	0	0	0
2	1	2	1	1	1	1	1	1	1	1	1	1	1	1	1	1	1	1	1	1	1	1



Continued

Time lag of RHU_Avg		Time lag of TEM_Avg		Time lag of NDVI		Time lag of RHU_Avg		Time lag of TEM_Avg		Time lag of NDVI		Time lag of RHU_Avg		Time lag of TEM_Avg		Time lag of NDVI		
pre	pre	pre	pre	pre	pre	pre	pre	pre	pre	pre	pre	pre	pre	pre	pre	pre	pre	
RHU_Avg	TEM_Avg	RHU_Avg	TEM_Avg	RHU_Avg	TEM_Avg	RHU_Avg	TEM_Avg	RHU_Avg	TEM_Avg	RHU_Avg	TEM_Avg	RHU_Avg	TEM_Avg	RHU_Avg	TEM_Avg	RHU_Avg	TEM_Avg	
NDVI	NDVI	NDVI	NDVI	NDVI	NDVI	NDVI	NDVI	NDVI	NDVI	NDVI	NDVI	NDVI	NDVI	NDVI	NDVI	NDVI	NDVI	
1	0	1	0	0.290	0.520	0.294	-0.125	-0.230	-0.100	0.163	0.034	0.124	-0.056	-0.251	-0.120	0.642	-0.181	0.217
1	2	1	0	0.430	0.360	0.043	-0.182	-0.154	0.096	0.072	0.050	0.046	-0.147	-0.192	-0.132	0.642	0.399	0.623
1	2	1	1	0.228	0.473	0.273	0	-0.220	0.088	-0.006	0.001	0.076	-0.143	-0.148	-0.115	0.642	0.399	0.623
1	0	2	0	0.291	0.554	0.370	-0.122	-0.180	-0.054	0.107	0.106	0.142	-0.067	-0.289	-0.125	0.571	-0.181	-0.024
2	0	0	0	0.513	0.479	0.279	-0.196	-0.064	-0.064	0.072	0.166	0.142	0.069	-0.386	-0.120	-0.089	-0.470	0.408
2	1	0	0	0.441	0.453	0.428	-0.28	0.017	0.102	0.059	0.186	0.140	0.051	-0.427	-0.134	-0.089	-0.260	0.428
2	1	1	0	0.477	0.334	0.292	-0.253	0	0.094	0.024	-0.063	0.169	0.002	-0.273	-0.127	0.093	-0.470	0.217
2	1	1	1	0.391	0.494	0.431	-0.065	-0.053	0.048	-0.071	-0.081	0.210	0.053	-0.283	-0.102	0.093	-0.470	0.217
2	1	2	0	0.199	0.353	0.480	-0.249	-0.023	0.073	0.049	-0.018	0.155	0.008	-0.301	-0.127	0.374	-0.260	0.558
2	1	2	1	0.377	0.390	0.434	-0.126	-0.062	0.009	0.048	0.055	0.165	0.042	-0.352	-0.101	0.374	-0.260	0.558
2	2	0	0	0.521	0.396	0.364	-0.284	0.007	0.106	0.075	0.195	0.046	0.005	-0.369	-0.130	-0.089	-0.129	0.271
2	2	1	0	0.587	0.264	0.123	-0.236	-0.017	0.093	0.014	-0.007	0.028	-0.058	-0.221	-0.121	0.093	-0.129	0.623
2	2	1	1	0.410	0.432	0.405	-0.101	-0.035	0.105	-0.084	-0.048	0.085	-0.024	-0.211	-0.102	0.093	-0.129	0.623
2	2	2	0	0.369	0.197	0.250	-0.238	-0.032	0.076	0.040	0.088	-0.025	-0.092	-0.245	-0.122	0.374	-0.129	0.625
2	2	2	1	0.396	0.321	0.398	-0.159	-0.028	0.079	0.015	0.113	0.028	-0.046	-0.287	-0.101	0.374	-0.129	0.625
2	2	2	2	0.307	0.249	0.520	0.039	-0.089	-0.004	-0.060	0.062	0.019	-0.087	-0.202	-0.083	0.374	-0.129	0.625
2	0	1	0	0.580	0.402	0.326	-0.198	-0.068	-0.050	0.061	0.019	0.170	0.040	-0.299	-0.114	0.093	-0.470	0.217
2	0	2	0	0.489	0.319	0.425	-0.203	-0.091	-0.044	0.087	0.090	0.178	0.023	-0.338	-0.118	0.374	-0.470	-0.024

## Methods and Applications

## Establishment and Application of a Radiation Dose Rate Model for Nuclear Medicine Examinees

Yuehua Hu<sup>1,✉</sup>; Xinyu He<sup>2,✉</sup>; Wenjia Zhao<sup>1</sup>; Lixin Ding<sup>3</sup>; Meiyong You<sup>1</sup>; Zihan Li<sup>1</sup>; Xinyu Liu<sup>1</sup>; Miaomiao Wang<sup>1</sup>; Siyi Chen<sup>4</sup>; Ziwei Lu<sup>5</sup>; Lei Qu<sup>6</sup>; Kuke Ding<sup>7</sup>; Li Zhang<sup>7,#</sup>; Qiuxian Fu<sup>8,#</sup>

### ABSTRACT

**Introduction:** Traditional methods for determining radiation dose in nuclear medicine include the Monte Carlo method, the discrete ordinate method, and the point kernel integration method. This study presents a new mathematical model for predicting the radiation dose rate in the vicinity of nuclear medicine patients.

**Methods:** A new algorithm was created by combining the physical model of “cylinder superposition” of the human body with integral analysis to assess the radiation dose rate in the vicinity of nuclear medicine patients.

**Results:** The model accurately predicted radiation dose rates within distances of 0.1–3.0 m, with a deviation of less than 11% compared to observed rates. The model demonstrated greater accuracy at shorter distances from the radiation source, with a deviation of only 1.55% from observed values at 0.1 m.

**Discussion:** The model proposed in this study effectively represents the spatial and temporal distribution of the radiation field around nuclear medicine patients and demonstrates good agreement with actual measurements. This model has the potential to serve as a radiation dose rate alert system in hospital environments.

During positron emission tomography/computed tomography (PET/CT) testing, it is crucial to administer radioactive isotopes. The  $\gamma$  radiation from these isotopes poses risks to nearby individuals, including medical staff, patients' families, and other nuclear medicine patients. Therefore, assessing the dose rate is essential for ensuring the safety of these individuals in close proximity.

Various methods are employed to calculate dose rates in radiation scenarios, including the Monte Carlo

method, the discrete ordinate method, and the point kernel integration method. Each method has its strengths and limitations. The Monte Carlo method uses probability and statistics but can be computationally slow and occasionally unsolvable (1). The discrete ordinate method offers fast calculations but struggles with complexity in large systems. The point kernel integration method uses a uniform grid for radiation sources but lacks real-time capabilities (2–4). To address these limitations, the “cylinder integration” method was developed to create a spatial-temporal model for radiation dose rates around nuclear medicine patients (5), offering a simplified and innovative approach to calculations.

### METHODS

Upon injection, <sup>18</sup>F-FDG rapidly dispersed throughout the body, achieving nearly complete distribution across organs within about 30 seconds (6). Gray-scale physical models were generated for each organ, correlating with their respective gray-scale values (Figure 1). Post-injection, gray-scale imaging was calibrated at three time points: 350–360 seconds (A1), 1,770–1,800 seconds (B1), and 3,480–3,600 seconds (C1), with radionuclide activity represented in charts A2, B2, and C2. For example, the radioactivity levels in different body regions at time points B2 and C2 can be illustrated by assigning values  $a_1$  to the head,  $a_2$  to the trunk,  $a_3$  to the heart,  $a_4$  to the bladder, and  $a_5$  to the legs. Detailed methodology for determining these values is provided in Supplementary Materials (available at <https://weekly.chinacdc.cn/>).

The methodology for calculating the radiation dose rate around organs that are symmetric along a common axis in the body is provided in the Supplementary Materials. To assess the radiation dose distribution from organs such as the heart, tumor, and legs, which are not aligned with the Z-axis of the cylinder, a translation technique was utilized to align them with

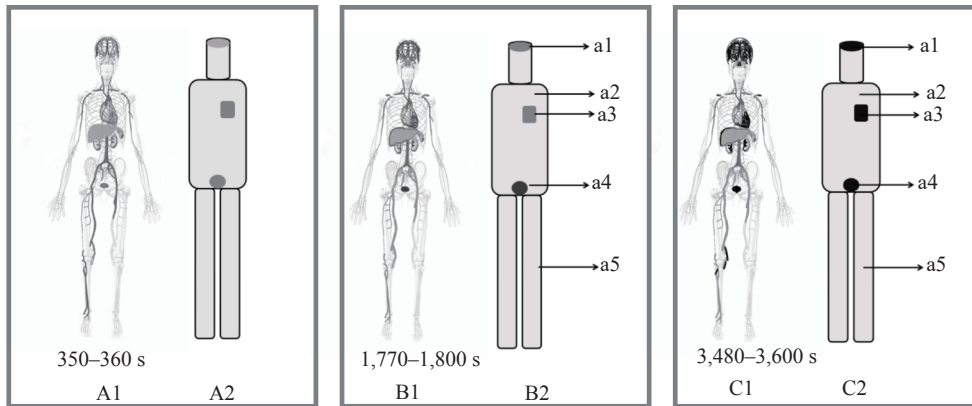


FIGURE 1. Schematic diagram of the grayscale values and corresponding specific activity of PET/CT or PET images. (A1) Gamma-ray imaging of the human body 350 to 360 seconds after radiopharmaceuticals are injected into the patient; (A2) Grayscale image of its corresponding organ; (B1) Gamma-ray imaging of the human body between 1,770 and 1,800 seconds after radiopharmaceutical injection into the patient; (B2) Grayscale image of its corresponding organ; (C1) Gamma-ray imaging of the human body 3,480 to 3,600 seconds after the injection of radiopharma into the patient; (C2) Grayscale image of its corresponding organ.

Abbreviation: PET/CT=positron emission tomography/computed tomography.

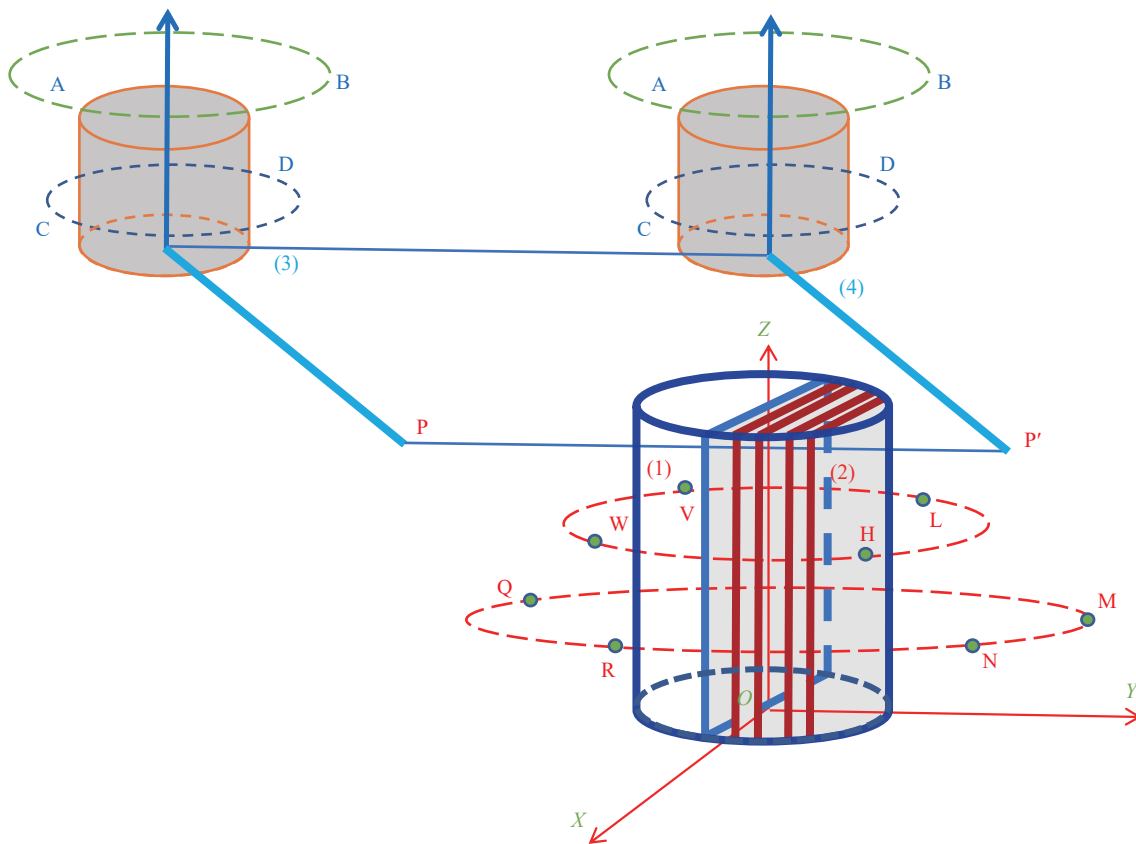


FIGURE 2. Schematic diagram illustrating the calculation of radiation dose rates around organs with non-axisymmetric axes. Note: In the same way that P is translated to P', (3) is translated to (4), coaxial with (1) and (2) below. The four points W, V, H and L mean that the four points are coaxial and on the same plane at the same height, so the radiation dose rate is the same; The four points, N, M, Q, R, are coaxial and on the same plane at the same height, so the radiation dose rate is the same.

the Z-axis using the equation  $OP=O' P'$  (Figure 2). This method ensured that the radiation dose rates at

points P and P' were equal. Additional information on the derivation process is available in the

## Supplementary Materials.

The method used for calculation assumes a uniform distribution of radioactive activity in the body, which may not always hold true. To improve accuracy, we introduced a “radiation dose rate correction factor” ( $\omega$ ) by comparing measured radiation dose rates near the body.  $\omega$  was determined as the average of theoretical and observed dose rates at different distances. Despite metabolic differences in radioactive pharmaceuticals, the corrected relative error remained below 11%, indicating the general applicability of the correction factor  $\omega$ .

The patient was injected with 127.4 MBq of  $^{18}\text{F}$ -FDG imaging agent through the median elbow vein at a hospital. The imaging agent, supplied by Beijing Atomic High Tech Co., Ltd., had a radiochemical purity of over 95%. Portable model 6,150 by Automes from Germany  $\gamma$  Peripheral dose equivalent rate instrument was used to measure the dose equivalent rate of radiation. Measurements were taken while the patient stood with hands naturally hanging down, the detector placed at the center of the patient’s chest facing forward. Measurements began 99 minutes post-injection, with distances ranging from 0.1 m to 3.0 m from the patient’s body surface. Each measurement, lasting 30 seconds, was repeated three times, recorded after stabilization, and averaged after background dose subtraction.

## RESULTS

The method used to calculate the spatiotemporal

distribution of radiation dose around a single cylindrical model can be found in the Supplementary Materials. Different body parts such as the head, trunk, legs, heart, bladder, and tumor were represented by cylinders in the mathematical model to estimate the radiation dose rate. The spatiotemporal radiation dose distribution around an individual was determined using the superposition method of coaxial and non-coaxial cylinder values.

To account for variations in height, weight, stance, and timing of radiopharmaceutical administration among subjects, standardization within a consistent coordinate system was essential, achieved through our computational model. The model’s unique aspect is the use of position translation to achieve a uniform spatiotemporal distribution of radiation dose rates. We harmonized horizontal discrepancies by aligning the subjects’ positions using horizontal translation (Figure 3). For individuals with different leg lengths, vertical height translation aligned their origin within the coordinate system, enabling precise dose rate comparisons. Additionally, we synchronized temporal variations in radiopharmaceutical administration by adjusting the starting times in the temporal parameter  $t$ , ensuring consistent dose rate calculation regardless of injection schedule differences.

Using the “cylinder” model and its associated algorithm, we estimated the radiation dose rate for the subject. We then compared this estimate to the actual measured data, allowing us to ascertain the deviation and calculate the mean discrepancy, denoted as  $\omega$ . Table 1 presents the relative differences between the

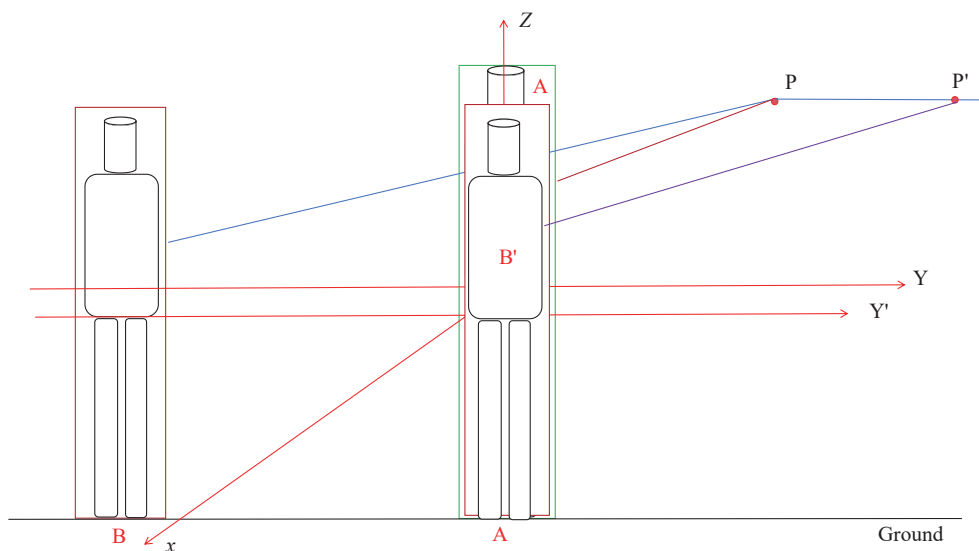


FIGURE 3. The standing positions of subjects A and B within the same space.

TABLE 1. Comparison of calculated and measured radiation dose rates.

Distance between the point and the body surface (m)	Theoretical rate ( $\mu\text{Gy}\cdot\text{h}^{-1}$ )	Measured rate ( $\mu\text{Gy}\cdot\text{h}^{-1}$ )	Difference ( $\mu\text{Gy}\cdot\text{h}^{-1}$ )	$\omega$ ( $\mu\text{Gy}\cdot\text{h}^{-1}$ )	Uncorrected relative error (%)	Corrected relative error (%)
0.1	242.48	238.78	3.70		1.55	1.81
0.5	44.56	41.02	3.54		8.63	10.16
1.0	14.50	16.65	-2.15	0.626	-12.91	-9.15
2.0	4.14	5.33	-1.19		-22.33	-10.58
3.0	1.92	2.69	-0.77		-28.62	-5.35

theoretical and measured dose rates. After applying the model's corrections for distances spanning from 0.1 to 3.0 meters, we found that the estimated dose rates consistently correlated with the measured values, exhibiting variances of less than 11%.

## DISCUSSION

Using a sophisticated human body model based on cylindrical elements, we have developed an integral solution that evolves from “point” to “line” and then to “surface” infinitesimals, allowing us to accurately compute the spatiotemporal distribution of radiation dose rates in the vicinity of nuclear medicine patients. The strength of this algorithm is rooted in its sound scientific principles and meticulous mathematical framework. Importantly, the model moves beyond the overly simplistic “point” or “line” representations of the human body and incorporates a more complex, layered cylindrical approach. This enhancement significantly improves the fidelity of simulations across various clinical situations, whether assessing radiation dose distribution around a single patient or multiple patients located on the same plane following radiopharmaceutical administration. The flexibility of the algorithm confirms its wide-ranging clinical utility. Through comparative calculations and validations, we have demonstrated that the estimated radiation dose rates at distances ranging from 0.1 to 3.0 meters are consistent with actual measurements. While some deviations exceeded 5 percent, they remained below the acceptable dose variation threshold of 15 percent, affirming the algorithm's suitability for clinical use. These results validate that the integration of a comprehensive computational strategy with a cylindrical superposition model of the human body considerably improves the accuracy of predicted dose rate distributions, thereby more closely reflecting the real radiation exposure levels around patients.

This study is subject to some limitations. First, the necessity of computational software development is crucial to expedite the application process due to the

complex calculations involved. Second, there is a discrepancy of 10.58% between measured and calculated values, attributed to the human body being simplified as a “cylinder”. To reduce this error, measurements should be taken with a human body model utilizing “cylinder superposition”. Third, it is essential to increase the radiation dose rate measurements around more participants to obtain an accurate correction factor for the radiation dose rate ( $\omega$ ).

**Conflicts of interest:** No conflicts of interest.

**Acknowledgements:** Shixi Zheng, Shuyuan Liu, Ziwei Lu, and Lei Qu for their contributions in preparing the figures.

**Funding:** Supported by the National Natural Science Foundation of China (grant nos. 31770907, 31640022 and 31170806), and the Beijing Natural Science Foundation (grant no. 7172146).

doi: 10.46234/ccdcw2024.108

# Corresponding authors: Li Zhang, Zhangli@chinacdc.cn; Qiuxian Fu, fuqiuxian51@163.com.

<sup>1</sup> Office of Epidemiology, Chinese Center for Disease Control and Prevention, Beijing, China; <sup>2</sup> Department of Oncology, Central Hospital Affiliated to Shandong First Medical University, Jinan City, Shandong Province, China; <sup>3</sup> National Institute for Radiological Protection, Chinese Center for Disease Control and Prevention, Beijing, China; <sup>4</sup> National Center for Chronic and Noncommunicable Disease Control and Prevention, Chinese Center for Disease Control and Prevention, Beijing, China; <sup>5</sup> Laboratory Animal Center, Chinese Center for Disease Control and Prevention, Beijing, China; <sup>6</sup> National Institute of Parasitic Diseases, Chinese Center for Disease Control and Prevention, Shanghai, China; <sup>7</sup> Office of Public Health Management, Chinese Center for Disease Control and Prevention, Beijing, China; <sup>8</sup> Hainan Medical University, Haikou City, Hainan Province, China.  
<sup>&</sup> Joint first authors.

Submitted: January 05, 2024; Accepted: March 05, 2024

## REFERENCES

- Huang Y, Liu HK. Development and application of graphics processor units-based Monte Carlo simulation in radiation dose calculation. *Chin J Med Phys* 2017;34(10):973 - 4. <https://doi.org/10.3969/j.issn.1005-202X.2017.10.001>. (In Chinese).
- Ohga Y, Fukuda M, Shibata K, Kawakami T, Matsuzaki T. A system for the calculation and visualisation of radiation field for maintenance support in nuclear power plants. *Radiat Prot Dosimetry* 2005;116(1-4 Pt

- 2):592 – 6. <http://dx.doi.org/10.1093/rpd/nci014>.
3. Subbaiah KV, Sarangapani R. GUI2QAD-3D: a graphical interface program for QAD-CGPIC program. *Ann Nuclear Energy* 2006;33(1):22 – 9. <https://doi.org/10.1016/j.anucene.2005.07.009>.
4. Ingersoll DT. User's manual for PUTZ: a point-kernel photon shielding code. Oak Ridge National Lab. 1986. [https://inis.iaea.org/search/search.aspx?orig\\_q=RN%3A18001366](https://inis.iaea.org/search/search.aspx?orig_q=RN%3A18001366). [2023-12-19].
5. China State Bureau of Technical Supervision. GB/T 10000-1988 Human dimensions of Chinese adults. Beijing: Standards Press of China, 1988. <https://openstd.samr.gov.cn/bzgk/gb/newGbInfo?hcno=A78583489235BF9BF9EE253E74DC76B9>. (In Chinese).
6. Tan H, Qi C, Cao YY, Cai DJ, Mao WJ, Yu HJ, et al. Ultralow-dose [<sup>18</sup>F]FDG PET/CT imaging: demonstration of feasibility in dynamic and static images. *Eur Radiol* 2023;33(7):5017 – 27. <https://doi.org/10.1007/s00330-023-09389-3>.

## SUPPLEMENTARY MATERIAL

### The Establishment of Physical Model in A “Cylinder Superposition”

According to the physical model known as “cylinder superposition,” the following relationships are established.

$$(\pi R_1^2 h_1 + \pi R_2^2 h_2 + 2\pi R_3^2 h_3) \rho = Mg \quad (1)$$

$$h_1 + h_2 + h_3 = H \quad (2)$$

$$\rho = \frac{Mg}{V} \quad (3)$$

### The Mathematical Model Corresponding to the Gray Value of Image and the Specific Activity of the Corresponding Part

Assuming the patient’s weight is represented by  $Mg$  (kg), height by  $H$  (m), actual body volume by  $V$  ( $m^3$ ) obtained through full water immersion, head height by  $h_1$  (m), torso height by  $h_2$  (m), leg height by  $h_3$  (m), head radius by  $R_1$  (m), torso radius by  $R_2$  (m), leg radius by  $R_3$  (m), and average human body density by  $\rho$  ( $kg/m^3$ ).

It is essential to understand the relationship between the gray scale values of images and the activity of radionuclides at their respective sites. To establish this, two time points post-radiopharmaceutical injection, denoted as  $t_1$  and  $t_2$ , were designated. PET-CT or PET images from these time intervals (1,770–1,800 seconds, 3,480–3,600 seconds) were chosen to represent each period (Figure 1). Assuming the patient does not void urine during the scanning, the following two equations can be deduced:

$$D_0 e^{-\lambda_1 t_1} = \pi k R_1^2 h_1 a_{1t_1} + \pi k R_2^2 h_2 a_{2t_1} + \pi k R_4^2 h_4 (a_{3t_1} - a_{2t_1}) + \pi k R_5^2 h_5 (a_{4t_1} - a_{2t_1}) + 2\pi k R_3^2 h_3 a_{5t_1} \quad (4)$$

$$D_0 e^{-\lambda_1 t_2} = \pi k R_1^2 h_1 a_{1t_2} + \pi k R_2^2 h_2 a_{2t_2} + \pi k R_4^2 h_4 (a_{3t_2} - a_{2t_2}) + \pi k R_5^2 h_5 (a_{4t_2} - a_{2t_2}) + 2\pi k R_3^2 h_3 a_{5t_2} \quad (5)$$

In the equations:

$D_0$  represents the initial activity value of  $^{18}F$ -FDG injected into the body.

$k$  is the scale factor between the radionuclide activity value and the gray-scale value of the image;

$\lambda_1$  represents the radioactive decay rate of  $^{18}F$ -FDG, while  $\lambda_2$  indicates the variation coefficient of metabolism in a specific organ, excluding the bladder.

$h_4$  represents the height of the “cylinder” corresponding to the heart;  $h_5$  represents the height of the “cylinder” corresponding to the bladder;

$R_4$  represents the radius of the heart “cylinder” and  $R_5$  represents the radius of the bladder “cylinder”;

$a_{1t_1}, a_{2t_1}, a_{3t_1}, a_{4t_1}, a_{5t_1}$  are the radionuclide activity values in the head, trunk, heart, bladder, and legs, measured at 1,770–1,800 seconds post-injection of the radiopharmaceutical;

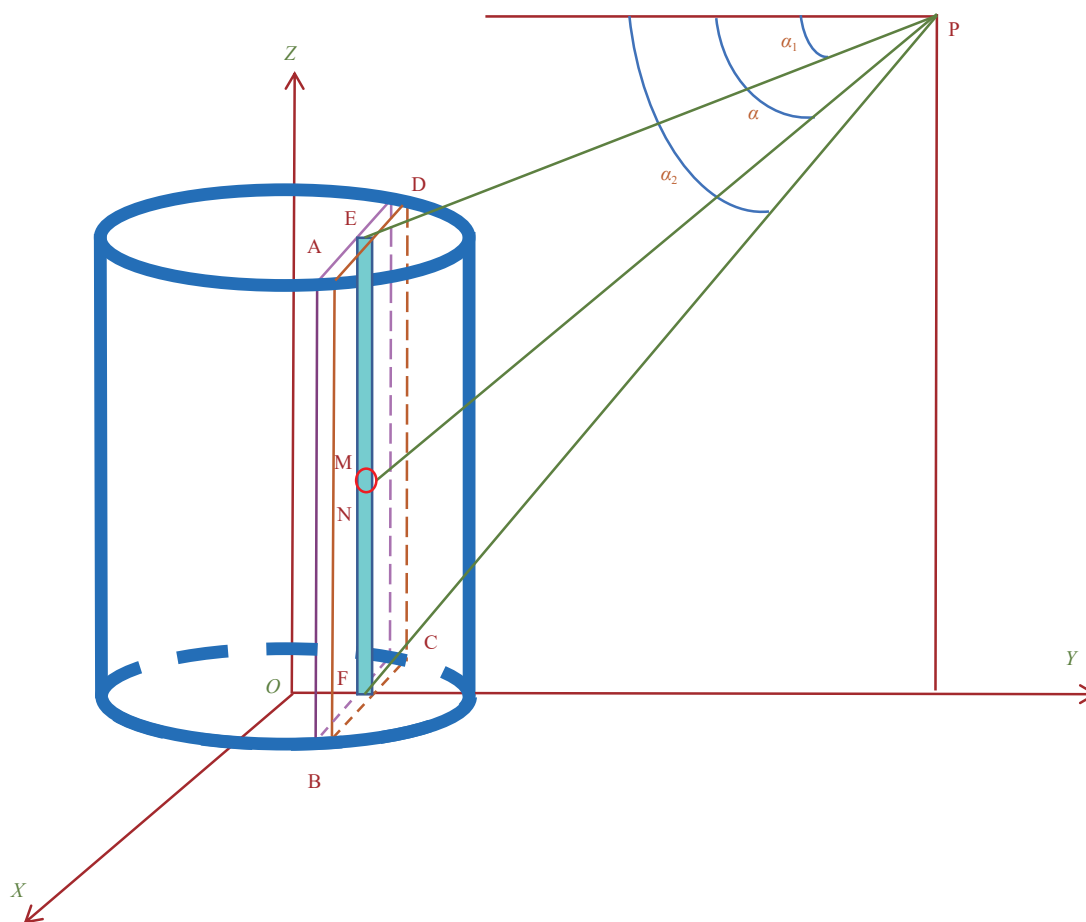
$a_{1t_2}, a_{2t_2}, a_{3t_2}, a_{4t_2}, a_{5t_2}$  are the radionuclide activity values in the head, trunk, heart, bladder, and legs, measured at 3,480–3,600 seconds post-injection of the radiopharmaceutical.

### The Calculation of the Spatial and Temporal Distribution of Radiation Dose Rates Around a Single “Cylinder Model”

It is essential to apply the integral method to calculate the infinitesimal solutions of points, lines, and surfaces of cylinders.

(i) Integral solutions for making the point infinitesimal: The research focuses on determining radiation dose distributions for cylindrical structures using the integration of infinitesimal points, lines, and surfaces within a human body model. This involves employing the concept of “cylinder superposition” to calculate radiation dose rates from point sources at varying distances, such as the “infinitesimal” MN on a linear radioactive source within the EF line segment (Figure 1).

According to the isotropic point source  $\gamma$  dose rate formula  $\left(X_0 = \frac{Q\Gamma}{R_{sp}^2}\right)(I)$ , for a specific monoenergetic gamma



SUPPLEMENTARY FIGURE S1. An “infinitesimal” MN on a “line source” EF.

ray emitted from a particular radioisotope, the  $\Gamma$ -constant used is the differential  $\Gamma$ -constant, represented as  $\Gamma_i$ . The total  $\Gamma$ -constant for the radioisotope, referred to as the  $\Gamma$ -constant, is the cumulative sum of  $\Gamma_i$ , which can be determined as follows:

$$\Gamma = 1.54 \times 10^5 \sum_{i=1}^m E_i n_i R_i \quad (6)$$

(ii) Integral solutions for making the line infinitesimal: By utilizing the spatial and temporal distribution solution of the radiation dose rate  $M_{head}$  surrounding a head cylinder model, we consider the distance between EF and PH as  $h_F$  (i.e., the length of FH) (Supplementary Figure S2).

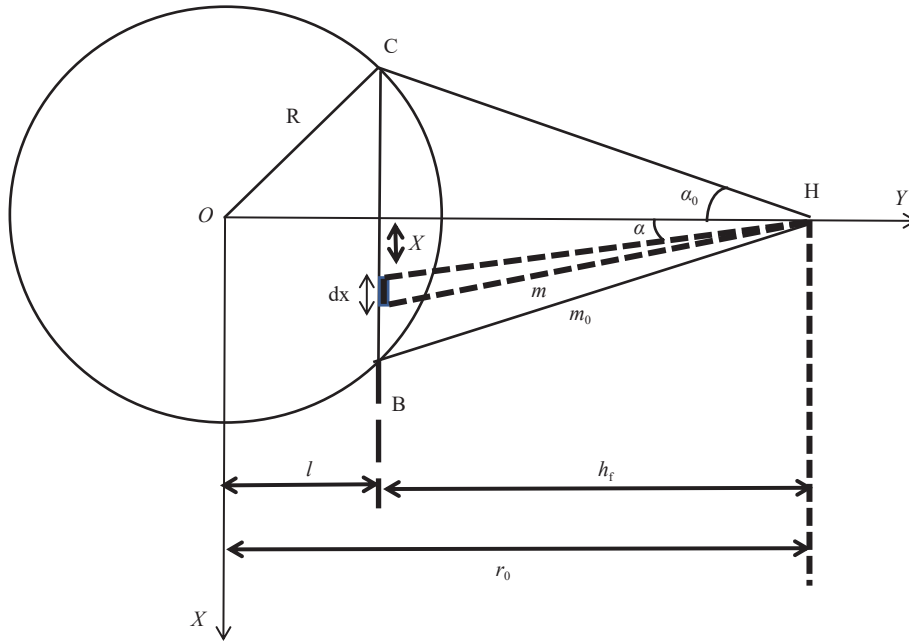
The angle between EF and PF is denoted as  $\theta_1$ , the angle between the extension of FE and PE is denoted as  $\theta_2$ , and the angle between FN and NP is denoted as  $\theta$ . The main integral equation is:

The height of  $\bar{EF}$  is assumed to be  $h$ ,

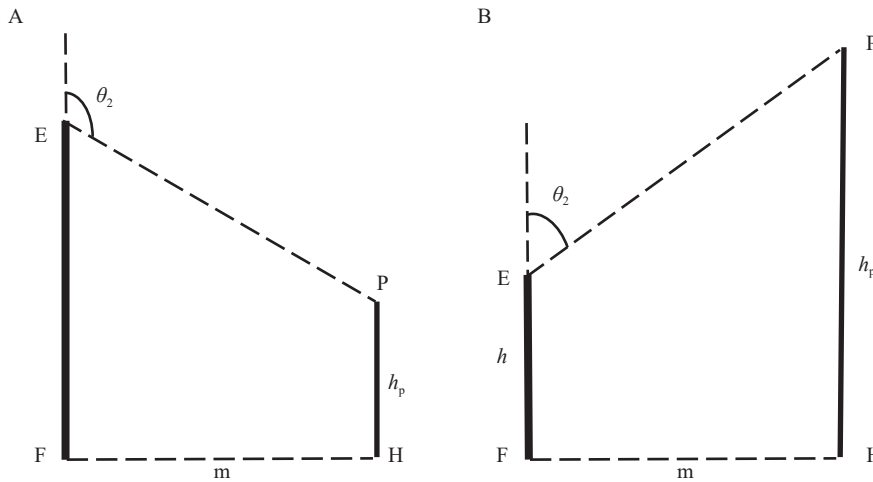
$$dM_{head} = \frac{A_{head} \Gamma_{\delta}}{r^2} dz \quad (7)$$

$$\begin{aligned} \dot{M}_{head} &= \int \frac{A_{head} \Gamma_{\delta}}{r^2} dz \\ &= \int \frac{D_0 e^{-\lambda t} a_{1t_1} \Gamma_{\delta}}{r^2} e^{-\lambda t} dz \\ &= \int \frac{D_0 e^{-\lambda t} a_{1t_1} \Gamma_{\delta}}{\left(\frac{h_F}{\sin \theta}\right)^2} e^{-\lambda t} d\left(-\frac{h_F}{\tan \theta}\right) \\ &= \frac{D_0 a_{1t_1} \Gamma_{\delta} e^{-\lambda t}}{h_F} (\theta_2 - \theta_1) \end{aligned} \quad (8)$$





SUPPLEMENTARY FIGURE S3. Bottom view of the head cylinder model.



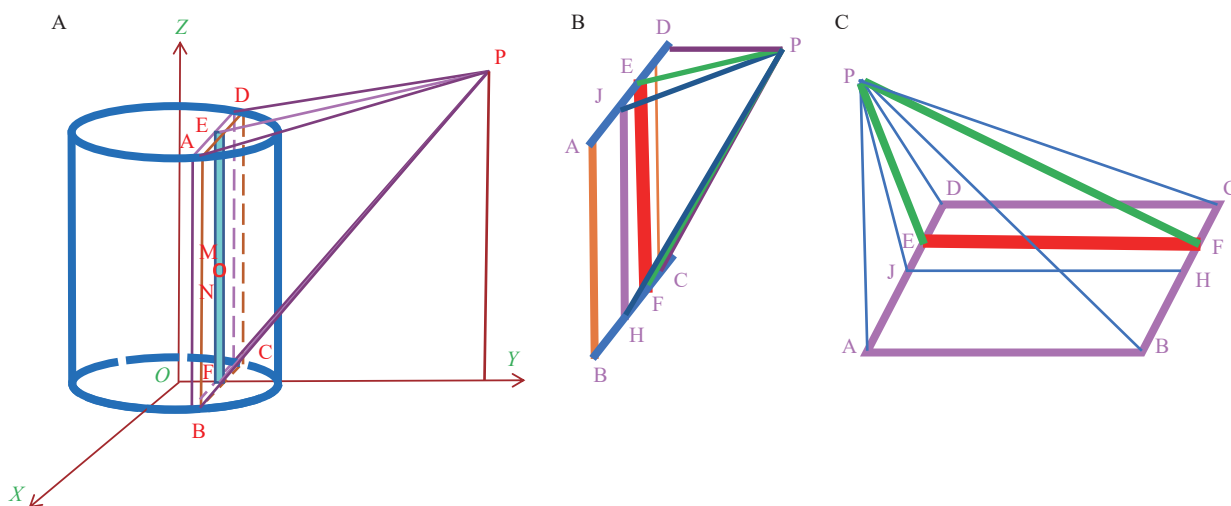
SUPPLEMENTARY FIGURE S4. (A). The relative positions of line segment EF and point P ( $h_p > h$ ). (B) The relative positions of line segment EF and point P ( $h_p < h$ ).

$$\begin{aligned}
 S_{(l)} &= 2 \int_0^{\sqrt{R^2 - l^2}} \frac{D_0 a_{1t} \Gamma_{\delta} e^{-\lambda t}}{h_F} (\theta_2 - \theta_1) dx \\
 &= 2 \int_0^{\sqrt{R^2 - l^2}} \frac{D_0 a_{1t} \Gamma_{\delta} e^{-\lambda t}}{h_F} \left( \arctan \left( \frac{\sqrt{(r_0 - l)^2 + x^2}}{h_p - h} \right) \right. \\
 &\quad \left. - \arctan \left( \frac{\sqrt{(r_0 - l)^2 + x^2}}{h_p} \right) \right) dx
 \end{aligned} \tag{13}$$

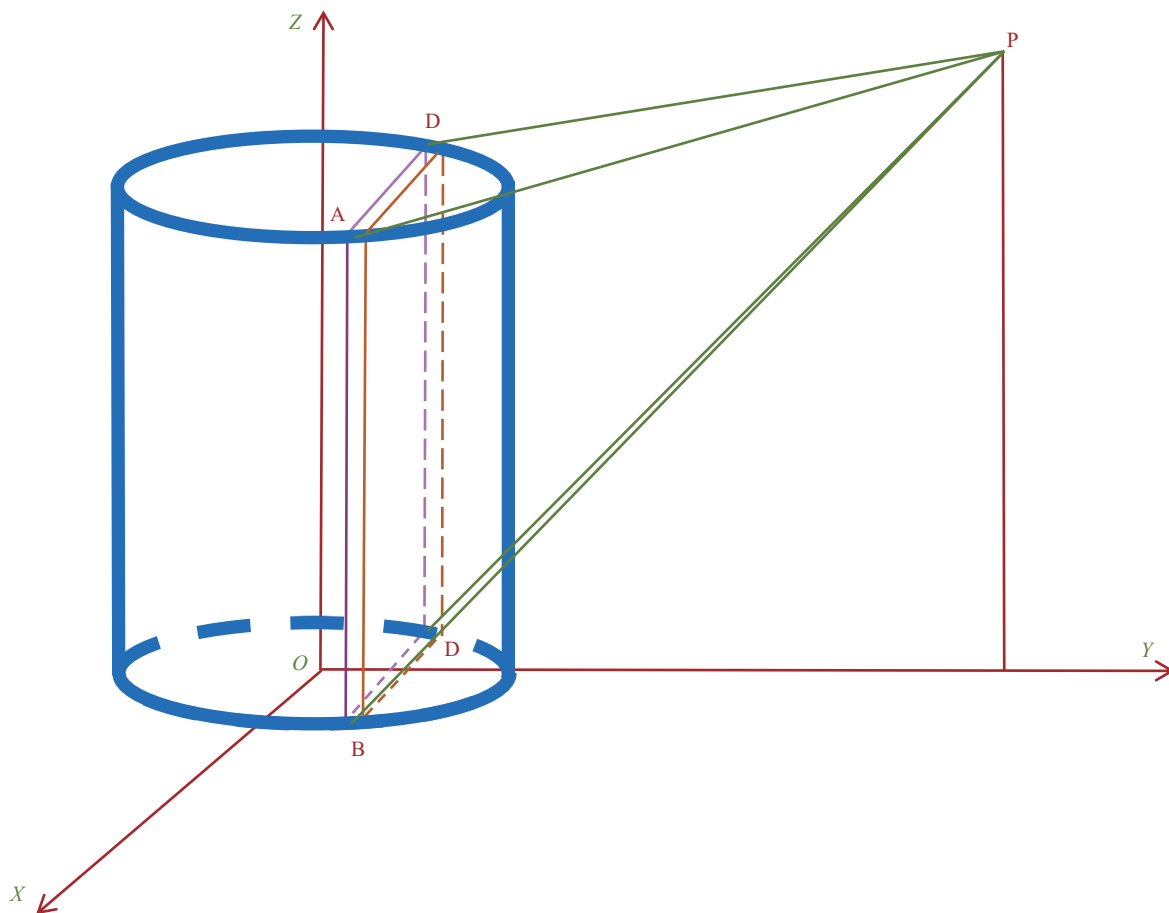
The volume integral was conducted for the infinitesimal surface ABCD using the surface integral mentioned previously (Supplementary Figure S6).

If the head cylinder model is used as an example, the head volume integral is calculated.

The volume integral of the right half cylinder is calculated as:

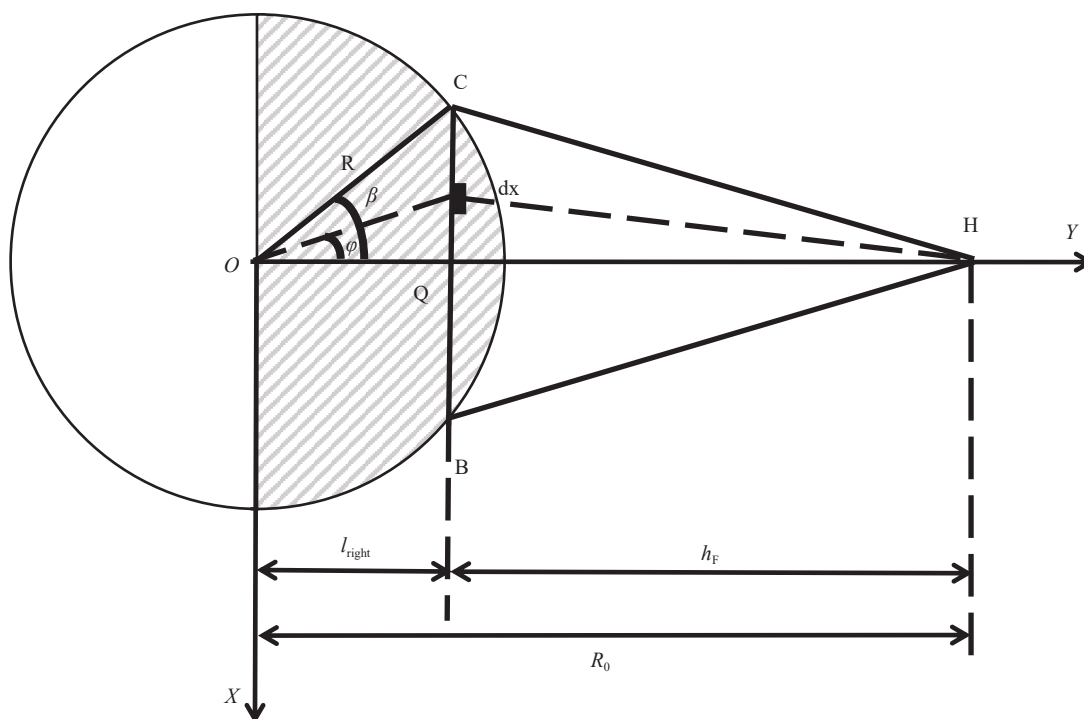


SUPPLEMENTARY FIGURE S5. A surface integral of ABCD (with the line segment EF as infinitesimal). Note: “A” represents the line infinitesimal diagram, “B” indicates the position of point P relative to the surface ABCD, and “C” illustrates the rotation diagram for “B”.



SUPPLEMENTARY FIGURE S6. Volume integral of cylinders with a thin surface ABCD as “infinitesimal”.

The line between point D and the center point O forms an angle  $\phi$  with the y-axis and  $\angle COQ=\beta$  (Supplementary Figure S7).  
 Because  $x > 0$  and  $y > 0$ ,



SUPPLEMENTARY FIGURE S7. Bottom view of the right half cylinder model.

$$S_{(\Delta)right} = \int_0^{\beta} \frac{D_0 a_{1t} \Gamma_{\delta} e^{-\lambda t}}{h_F} \left( \arctan \left( \frac{\sqrt{(r_0 - R \cos \beta)^2 + (R \cos \beta \tan \phi)^2}}{h_p - h} \right) - \arctan \left( \frac{\sqrt{(r_0 - R \cos \beta)^2 + (R \cos \beta \tan \phi)^2}}{h_p} \right) \right) \frac{R \cos \beta}{\cos^2 \phi} d\phi \quad (14)$$

The radiation dose rate to point P from the right half of the cylinder in the region where  $y > 0$  is represented by the variable  $G_{right}$ :

$$G_{right} = 2 \int_0^{\frac{\pi}{2}} S_{(\Delta)right} R \cos \beta d\beta \quad (15)$$

The volume integral of the left half cylinder was calculated as shown in Supplementary Figure S8.

When  $x > 0$ ,  $y < 0$ ,

$$\begin{aligned} S_{(\Delta)left} &= \int_{\beta}^{\pi} \frac{D_0 a_{1t} \Gamma_{\delta} e^{-\lambda t}}{h_F} \left( \arctan \left( \frac{\sqrt{(r_0 + l_{left})^2 + x^2}}{h_p - h} \right) - \arctan \left( \frac{\sqrt{(r_0 + l_{left})^2 + x^2}}{h_p} \right) \right) \frac{R \cos \beta}{\cos^2 \phi} d\phi \\ &= \int_{\beta}^{\pi} \frac{D_0 a_{1t} \Gamma_{\delta} e^{-\lambda t}}{h_F} \left( \arctan \left( \frac{\sqrt{(r_0 - R \cos \beta)^2 + (R \cos \beta \tan \phi)^2}}{h_p - h} \right) - \arctan \left( \frac{\sqrt{(r_0 - R \cos \beta)^2 + (R \cos \beta \tan \phi)^2}}{h_p} \right) \right) \frac{R \cos \beta}{\cos^2 \phi} d\phi \end{aligned} \quad (16)$$

The volume integral of the left half cylinder is:

$$V_{left} = 2 \int_{\frac{\pi}{2}}^{\pi} S_{(\Delta)left} R \cos \beta d\beta \quad (17)$$



## Outbreak Reports

## First Case Report of Cystic Echinococcosis Caused by G7 Genotype *Echinococcus intermedius* Confirmed by Genetic Sequencing — Southern China, December 2023

De Wu<sup>1#</sup>; Jiayi Zhang<sup>1</sup>; Jieling Wang<sup>1</sup>; Yangyang Zhao<sup>2</sup>; Lei Wang<sup>1</sup>; Qiang Mao<sup>1</sup>; Haisen Lin<sup>3</sup>; Gang Yao<sup>2</sup>; Guanting Zhang<sup>1</sup>; Xu Wang<sup>4</sup>; Chuizhao Xue<sup>4</sup>; Ying Wang<sup>4</sup>; Jingdiao Chen<sup>1</sup>

### Summary

#### What is already known about this topic?

Echinococcosis exhibits a global distribution. In China, the primary endemic area is the northwest region. In December 2023, we documented a case of echinococcosis in an individual lacking any travel or residential history in endemic regions.

#### What is added by this report?

This is the first laboratory-confirmed case of hepatic echinococcosis reported in Guangdong Province, associated with the G7 genotype of *Echinococcus granulosus* (*E. granulosus*). The most probable mode of transmission is a local infection resulting from *E. granulosus* introduced from endemic regions.

#### What are the implications for public health practice?

As the circulation of agricultural products increases, it is essential to enhance the quarantine and management of livestock from epidemic areas to prevent and control the spread of echinococcosis to non-epidemic regions.

Echinococcosis, a zoonotic disease resulting from infection by *Echinococcus* larvae, has been a persistent health threat. This disease transmits to humans through the ingestion of parasitic eggs. By 2022, China reported echinococcosis in nine epidemic regions encompassing 290,926 villages across 370 affected counties (including cities, districts, and banners). A total of 26,773 cases were recorded, predominantly in the provincial-level administrative divisions (PLADs) of Sichuan, Qinghai, and Xizang (1). Advances in molecular technology have facilitated the differentiation of *Echinococcus* species into several genotypes, specifically G1–G10 and the so-called lion genotype. With the exception of the G2 and G9 genotypes, all others have been verified (2). Currently, the predominant genotype in China is G1, complemented by minor occurrences of G3 and G6

genotypes (3–6). The G7 genotype, however, has been infrequently reported (7).

In December 2023, a case of hepatic cystic echinococcosis was reported in Zhuhai City, Guangdong Province. To confirm the diagnosis and trace the source of infection, we conducted epidemiological investigations, case searches, polymerase chain reaction (PCR) testing, genotyping, and examination of tapeworm eggs in canine feces. Findings revealed that the individual had no travel or residency history in areas known for such infections. Genotyping identified the *Echinococcus granulosus* as belonging to the G7 genotype, a genotype seldom observed in China (7). Preventive measures recommended include health education in the affected area, banning unauthorized livestock slaughtering, stricter quarantine and management of imported livestock, and enhanced monitoring and pathogen testing of cases.

## INVESTIGATION AND RESULTS

A 27-year-old male presented at Zhuhai People's Hospital on November 26, 2023, with black stool. The following day, he underwent hemostatic endoscopic surgery for a duodenal ulcer. Before discharge, the patient noted a lump in his upper left abdomen but exhibited no clinical symptoms and requested further evaluation. A computer tomography (CT) scan of the upper abdomen performed on November 30 revealed a space-occupying lesion in the left lobe of the liver. He was readmitted on December 11, and a laparoscopic resection of the mass was successfully performed on December 14, completely removing the mass without any complications.

Since 2016, the individual primarily lived in Nanxiong City, Zhuhai City, and Guangzhou City in Guangdong Province, as well as Wuhan City in Hubei Province, with the longest duration spent in Nanxiong

City. Throughout this time, he made short visits to Henan and Jiangsu provinces. He asserted that he neither traveled to nor resided in areas known for epidemics, nor did he purchase leather or frozen meat products from such regions online. Although he is fond of cats and dogs, he has not kept them at home. While residing in Wuhan and Zhuhai, he frequently encountered stray cats and occasionally stray dogs. In his native Nanxiong, where most villagers own dogs, he had more frequent interactions with dogs. However, his family is not involved in livestock slaughter or the fur processing industry.

To better elucidate the potential infection origins, we investigated livestock sources and slaughtering practices in Nanxiong City. In Nanxiong, pork is the predominant meat consumed, and pigs must be slaughtered at officially designated sites. Given the prohibition on swine imports from other PLADs into Guangdong, all pigs in Nanxiong are sourced locally. Unlike pigs, cattle in Nanxiong are not predominantly from large-scale farms but are rather raised by individual farmers. Annually, over 2,000 cattle — including water buffalo, yellow cattle, and Simmental cattle — are processed in local slaughterhouses. These cattle are sourced primarily from PLADs outside Guangdong, with Liaoning, Xinjiang, and Inner Mongolia being major suppliers. In contrast, local sheep consumption is minimal, with most sheep sourced from Xinfeng County, Jiangxi Province.

According to the Diagnostic Criteria for Echinococcosis (WS 257-2006), we conducted a case search via the China Information System for Disease Control and Prevention (CISDCP). Since the first reported case of imported *E. granulosus* in 2006, a total of 149 echinococcosis cases have been recorded through December 2023. These include 28 confirmed, 4 clinically diagnosed, and 117 suspected cases. Notably, none of these cases were confirmed through nucleic acid diagnosis or molecular typing. Additionally, 53 canine fecal samples collected from Zhuhai and Nanxiong were examined for *Echinococcus* eggs using an automatic fecal analysis system; no eggs were detected in these samples.

The initial medical evaluations play a critical role in the diagnostic process for this case. Routine blood tests showed a monocyte count of  $0.61 \times 10^9/L$ , marginally above the normal range of  $0.1 \times 10^9 - 0.6 \times 10^9/L$ , with all other parameters falling within normal limits. CT imaging of the upper abdomen revealed a normal liver morphology, but identified a circular, mixed-density nodular shadow near the capsule in the left inner lobe,

measuring approximately 23 mm in diameter. This lesion displayed multiple internal calcifications, particularly around its clearly defined edges (Figure 1A). Histopathological examination confirmed the presence of a grayish-yellow tumor with a dark red, oval contour measuring 2.8 cm  $\times$  tumor was encapsulated, with most of the capsule remaining intact (Figure 1B).

To confirm the diagnosis, pathological tissue samples were collected from which nucleic acids were extracted. The *cox1* and *nad1* genes were amplified to produce PCR fragments of 874 bp and 529 bp, respectively. These products were then sequenced, yielding effective DNA sequences of 791 bp and 479 bp. BLAST sequence alignment showed that these sequences exhibited 100% nucleotide homology with *Echinococcus granulosus sensu lato* genotype G7 isolate 92 mitochondrion (MH301020.1) and *Echinococcus candidasis* mitochondrial NADH1 gene strain G7 (AJ237975.1). Both sequences were deposited in GenBank under the accession numbers PP158976.1 and PP187231.1.

To determine the genotype of the *Echinococcus granulosus* strain identified in this study (2023-ZH-EG-1), we compared the *cox1* and *nad1* gene sequences with 28 corresponding sequences from GenBank. We employed these sequences to construct phylogenetic trees as displayed in Figure 2. These sequences encompassed a range of genotypes within the *Echinococcus* genus, specifically G1, G3–G8, G10, and the Lion strain. Analysis of the phylogenetic trees revealed that the gene sequences of *E. granulosus* from our study clustered with the reference G7 genotype initially, and subsequently formed a broader cluster with the G6 genotype. This clustering pattern

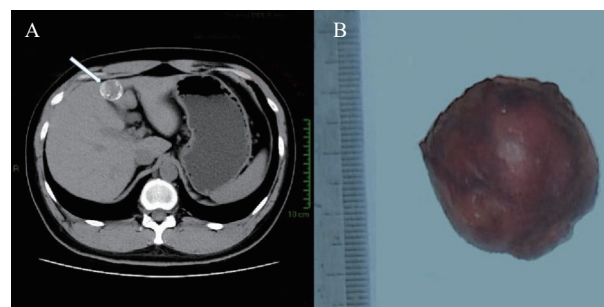


FIGURE 1. Abdominal CT and Cysts of Cystic Echinococcus Case in Zhuhai City, Guangdong Province, 2023. (A) A circular image (arrows) in the left inner lobe of the liver, displaying a diameter of approximately 23 mm; (B) the complete cysts that were surgically removed. Abbreviation: CT=computer tomography.

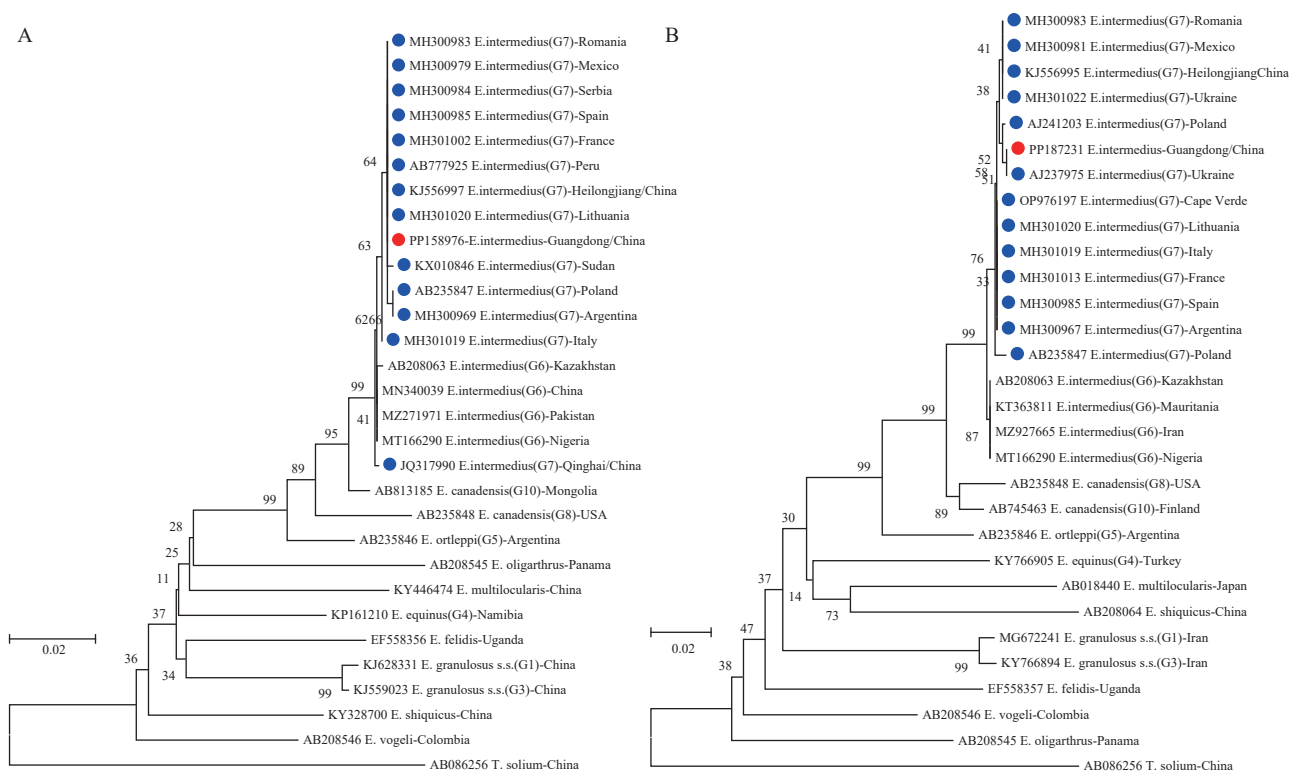


FIGURE 2. The phylogenetic trees were constructed using the Neighbor-Joining method based on mtDNA genes (A) *cox1* and (B) *nad1*.

Notes: The red dots represent the sequences from this study, while the blue dots depict the G7 representative sequences.

distinctly separates it from other genotypes. Based on these observations, we concluded that the *E. granulosus* strain in this study belongs to the G7 genotype.

## PUBLIC HEALTH RESPONSE

It is necessary to promote the prevention knowledge of echinococcosis among residents in the area where the case occurred. Echinococcosis monitoring should be carried out in medical institutions in Shaoguan City, and local government departments should further strengthen animal slaughter management and animal disease quarantine.

## DISCUSSION

This study presents the first reported instance of hepatic echinococcosis in an individual with no travel or residency history in an endemic area. Additionally, this is the first laboratory-confirmed case of its genotype in Guangdong. Consequently, it is critical to determine the time and location of infection, identify the source, and, most importantly, understand the transmission pattern.

Following infection, individuals typically remain asymptomatic for extended periods, attributable to the slow growth of cysts, particularly in the liver where growth rates vary from 1 mm to 5 mm in diameter annually (8). The cyst examined in this instance measured approximately 25 mm and exhibited signs of partial calcification, suggesting that the infection may have occurred between 2 to 3 years ago, or possibly earlier. Epidemiological investigations revealed that during this period, the patient resided primarily in Wuhan, Zhuhai, and Nanxiong cities. The likelihood of encountering the infection source in Wuhan and Zhuhai was notably low. Dogs are recognized as a critical reservoir host for echinococcosis, and in Nanxiong, the patient had increased contact with dogs, thus raising the probability of infection. Consequently, it appears more plausible that the infection was contracted in Nanxiong.

Livestock serve as significant intermediate hosts for *Echinococcus granulosus*. Recent surveys indicate that while the infection rate of *Echinococcus* in livestock within endemic regions of China has considerably declined, sheep and cattle remain the predominant intermediate hosts. For genotype G7, domestic pigs are the most common intermediate hosts (9), though

instances in goats and wildlife have also been reported (3). In Nanxiong, a substantial number of cattle and a smaller number of sheep are annually imported from endemic areas. This movement of livestock poses a risk of introducing pathogens into Guangdong, potentially leading to localized transmission cycles.

*Echinococcus* species have a global distribution, found in Asia, Europe, North America, Oceania, and some African countries. The primary endemic areas in Northwest China include Xinjiang, Xizang, Qinghai, Gansu, Ningxia, Sichuan, and Inner Mongolia PLADs (4). Currently, of the 9 recognized genotypes of *Echinococcus* effective in human infection, genotypes G1, G6, and G7 are predominant, comprising 88.4%, 7.34%, and 3.7% of human infections respectively (5). Although the G7 genotype is less commonly observed in humans and animals globally compared to G1, in certain countries like Poland and Austria, it accounts for 100% (30/30) and 92.0% (23/25) of human hydatid cyst cases, respectively (6). Hence, the pathogenicity of *E. granulosus* genotypes appears to be influenced by geographic factors. The G7 genotype, also known as the “pig strain”, primarily uses pigs as its intermediate hosts, though cattle, goats, sheep, and wild bears can also fulfill this role (6). The broad distribution of the G7 genotype indicates its adaptability and suggests the potential establishment of a cycle involving this genotype in Guangdong.

In 2011, Jin et al. identified the G7 genotype of *Echinococcus intermedium* in goats from Qinghai Province. By 2014, Zhang et al. detected this genotype in four out of ten human liver cysts in Heilongjiang Province, marking the first documented instance of human infection with the G7 genotype of *Echinococcus granulosus* in China (6). The current study reveals that cases of echinococcosis of unknown origin in Zhuhai City, Guangdong Province, are attributable to the G7 genotype of *E. granulosus*. This represents the first report of such infections in Guangdong Province, and the third instance in China. Similar to isolated cases, such as the G7 genotype in Heilongjiang Province (6) and the G5 genotype in Guangxi and Guizhou PLADs (10), the recent case also emerged in a region not typically endemic for echinococcosis. These findings emphasize the urgent need for enhanced echinococcosis prevention and control measures in regions not traditionally affected by the disease, particularly through stringent quarantine and management of potential intermediate hosts such as pigs, cattle, and sheep.

Based on the findings, we propose two potential

transmission patterns for echinococcosis in Guangdong. The first is an input pattern, wherein pathogens are introduced into the area through the importation of livestock. Dogs contract the infection by consuming the organs of these infected animals, subsequently transmitting the disease to humans through contact. The second pattern is local, characterized by a consistent, albeit low-level, cycle of echinococcosis among local fauna, with infrequent human transmission. It is imperative to enhance quarantine measures to fully elucidate these transmission dynamics.

**Conflicts of interest:** No conflicts of interest.

**Acknowledgements:** The physicians at Zhuhai First People’s Hospital for their assistance with medical examinations and for providing CT images.

**Funding:** Supported by the Key Laboratory of Emergency Detection Technology for Emerging Infectious Diseases in Guangdong Province, approval number 2023B112010010 (2023).

doi: 10.46234/ccdcw2024.109

# Corresponding author: De Wu, wude68@tom.com.

<sup>1</sup> Parasitic Disease Prevention and Control Institute, Guangdong Center for Disease Control and Prevention, Guangzhou City, Guangdong Province, China; <sup>2</sup> Epidemic Prevention and Control Institute, Zhuhai Center for Disease Control and Prevention, Zhuhai City, Guangdong Province, China; <sup>3</sup> Department of Prevention & Healthcare, Zhuhai First People's Hospital, Zhuhai City, Guangdong Province, China; <sup>4</sup> National Institute of Parasitic Diseases, Chinese Center for Disease Control and Prevention (Chinese Center for Tropical Diseases Research), Shanghai, China.

Submitted: March 07, 2024; Accepted: May 11, 2024

## REFERENCES

- Kui Y, Xue CZ, Wang X, Liu BX, Wang Y, Wang LY, et al. Progress of echinococcosis control in China, 2022. *Chin J Parasitol Parasit Dis* 2024;42(1):8 - 16. <https://doi.org/10.12140/j.issn.1000-7423.2024.01.002>.
- D'Alessandro A, Rausch RL. New aspects of neotropical polycystic (*Echinococcus vogeli*) and unicystic (*Echinococcus oligarthrus*) echinococcosis. *Clin Microbiol Rev* 2008;21(2):380 - 401. <https://doi.org/10.1128/CMR.00050-07>.
- Fadakar B, Tabatabaei N, Borji H, Naghibi A. Genotyping of *Echinococcus granulosus* from goats and sheep indicating G7 genotype in goats in the Northeast of Iran. *Vet Parasitol* 2015;214(1-2):204 - 7. <https://doi.org/10.1016/j.vetpar.2015.09.029>.
- Deng XY, Kui Y, Guan YY, Wu WP. Research progress in terminal host infection of *Echinococcus aureus*. *J Pathog Biol* 2023;18(8):978 - 82. <https://doi.org/10.13350/j.cjpb.230822>.
- Sun H, Li L, Yan HB, Li XR, Fu BQ, Jia WZ. Research progress on molecular markers and epidemiology of *Echinococcus ortleppi*. *Chin J Parasitol Parasit Dis* 2023;41(2):213 - 8. <https://doi.org/10.12140/j.issn.1000-7423.2023.02.014>.
- Zhang TM, Yang D, Zeng ZL, Zhao W, Liu AQ, Piao D, et al. Genetic characterization of human-derived hydatid cysts of *Echinococcus granulosus* Sensu Lato in Heilongjiang Province and the first report of

- G7 genotype of *E. canadensis* in humans in China. PLoS One 2014;9(10):e109059. <https://doi.org/10.1371/journal.pone.0109059>.
7. Ohiolai JA, Xia CY, Li L, Liu JZ, Tang WQ, Wu YT, et al. Genetic variation of *Echinococcus* spp. in yaks and sheep in the Tibet Autonomous Region of China based on mitochondrial DNA. Parasit Vectors 2019;12(1):608. <https://doi.org/10.1186/s13071-019-3857-1>.
  8. Nunnari G, Pinzone MR, Gruttadauria S, Celesia BM, Madeddu G, Malaguarnera G, et al. Hepatic echinococcosis: clinical and therapeutic aspects. World J Gastroenterol 2012;18(13):1448 – 58. <https://doi.org/10.3748/wjg.v18.i13.1448>.
  9. Cardona GA, Carmena D. A review of the global prevalence, molecular epidemiology and economics of cystic echinococcosis in production animals. Vet Parasitol 2013;192(1-3):10 – 32. <https://doi.org/10.1016/j.vetpar.2012.09.027>.
  10. Wang X, Zhu AY, Cai HY, Liu BX, Xie G, Jiang R, et al. The pathology, phylogeny, and epidemiology of *Echinococcus ortleppi* (G5 genotype): a new case report of echinococcosis in China. Infect Dis Poverty 2021;10(1):130. <https://doi.org/10.1186/S40249-021-00907-3>.

## Youth Editorial Board

**Director** Lei Zhou

**Vice Directors** Jue Liu    Tiantian Li    Tianmu Chen

### Members of Youth Editorial Board

Jingwen Ai	Li Bai	Yuhai Bi	Yunlong Cao
Gong Cheng	Liangliang Cui	Meng Gao	Jie Gong
Yuehua Hu	Jia Huang	Xiang Huo	Xiaolin Jiang
Yu Ju	Min Kang	Huihui Kong	Lingcai Kong
Shengjie Lai	Fangfang Li	Jingxin Li	Huigang Liang
Di Liu	Jun Liu	Li Liu	Yang Liu
Chao Ma	Yang Pan	Zhixing Peng	Menbao Qian
Tian Qin	Shuhui Song	Kun Su	Song Tang
Bin Wang	Jingyuan Wang	Linghang Wang	Qihui Wang
Xiaoli Wang	Xin Wang	Feixue Wei	Yongyue Wei
Zhiqiang Wu	Meng Xiao	Tian Xiao	Wuxiang Xie
Lei Xu	Lin Yang	Canqing Yu	Lin Zeng
Yi Zhang	Yang Zhao	Hong Zhou	

Indexed by Science Citation Index Expanded (SCIE), Social Sciences Citation Index (SSCI), PubMed Central (PMC), Scopus, Chinese Scientific and Technical Papers and Citations, and Chinese Science Citation Database (CSCD)

**Copyright © 2024 by Chinese Center for Disease Control and Prevention**

All Rights Reserved. No part of the publication may be reproduced, stored in a retrieval system, or transmitted in any form or by any means, electronic, mechanical, photocopying, recording, or otherwise without the prior permission of *CCDC Weekly*. Authors are required to grant *CCDC Weekly* an exclusive license to publish.

All material in *CCDC Weekly Series* is in the public domain and may be used and reprinted without permission; citation to source, however, is appreciated.

References to non-China-CDC sites on the Internet are provided as a service to *CCDC Weekly* readers and do not constitute or imply endorsement of these organizations or their programs by China CDC or National Health Commission of the People's Republic of China. China CDC is not responsible for the content of non-China-CDC sites.

The inauguration of *China CDC Weekly* is in part supported by Project for Enhancing International Impact of China STM Journals Category D (PIIJ2-D-04-(2018)) of China Association for Science and Technology (CAST).



*Vol. 6 No. 23 Jun. 7, 2024*

---

**Responsible Authority**

National Disease Control and Prevention Administration

**Sponsor**

Chinese Center for Disease Control and Prevention

**Editing and Publishing**

China CDC Weekly Editorial Office

No.155 Changbai Road, Changping District, Beijing, China

Tel: 86-10-63150501, 63150701

Email: [weekly@chinacdc.cn](mailto:weekly@chinacdc.cn)

**CSSN**

ISSN 2096-7071

CN 10-1629/R1